Quantitative Monitoring of Tissue Fractionation by Cavitation-Based High-Intensity Focused Ultrasound

Minho Song

A dissertation

submitted in partial fulfillment of the

requirements for the degree of

Doctor of Philosophy

University of Washington

2024

Reading Committee:

Tatiana Khokhlova, Chair

Michael Bailey

Peter Dahl

Program Authorized to Offer Degree:

Mechanical Engineering

University of Washington

Abstract

Quantitative Monitoring of Tissue Fractionation by Cavitation-based High-Intensity Focused Ultrasound

Minho Song

Chair of the Supervisory Committee:
Tatiana Khokhlova
Division of Gastroenterology, UW Medicine

High-intensity focused ultrasound (HIFU) can non-invasively induce cavitation within tissue, resulting in mechanical tissue damage that ranges from mild disruption with petechial hemorrhage to complete liquefaction at a subcellular scale. This capability positions HIFU as an increasingly promising and valuable tool in various clinical applications, such as enhancing drug delivery through increased tissue permeability, modulating the tumor microenvironment, and ablating tumors. In this dissertation, the quantitative monitoring of residual cavitation bubbles was investigated based on ultrasound Doppler technique. The research focuses on two main HIFU regimes that induce mechanical tissue fractionation: less destructive pulsed HIFU (pHIFU) and boiling histotripsy (BH), each with distinct mechanism of inducing cavitation and varying level of

subsequent tissue damage. Doppler-based quantitative metrics for each regime were developed and correlated with tissue damage or liquefaction levels evaluated through histological image analysis. Particularly, a new Doppler technique based on dynamic mode decomposition (DMD) for rapidly dissolving cavitation bubbles following the HIFU pulse was introduced, with demonstrations *in silico* and *ex vivo,* where DMD showed superior performance compared to widely used techniques (Chapter 2). This DMD-based Doppler technique was then applied to surgically exposed *in vivo* tissues, showing a strong correlation between DMD-derived bubble dissolution rate and tissue damage level (Chapter 3). Doppler measurements were also conducted to capture the swiftly moving residual bubbles following BH pulses in *ex vivo* experiments, displaying gradually increasing and saturating in observed maximum velocity as treatment progressed (Chapter 4). Similar measurements, conducted on *in vivo* abdominal tissue in pigs, confirmed a strong correlation between maximum velocity and level of tissue liquefactions (Chapter 5).

TABLE OF CONTENTS

LIST OF FIGURES

LIST OF TABLES

ACKNOWLEDGEMENTS

Standing at the very final stage of my five-year Ph.D. studies, I am filled with ambivalent emotions. I am excited to successfully complete this long-lasting project and embark on the next chapter of my life. At the same time, I feel a sense of nostalgia for the bittersweet journey that has brought me here. I believe the sadness comes from leaving behind the incredible people I met and worked with, whose sincere support I deeply appreciate.

First and foremost, I would like to express my sincere gratitude to my advisor, Prof. Tatiana Khokhlova. Her patient guidance, support, encouragement, and mentorships have significantly influenced my development from an amateur student to an independent researcher. It has been the best opportunity to work with her and learn closely during my studies.

I would also like to thank the other members of my supervisory committee, Drs. Mike Bailey, Mike Averkiou, and Peter Dahl, for their valuable comments, feedback, and suggestions for my research. My gratitude extends to Drs. Oleg Sapozhnikov, Vera Khokhlova, and Adam Maxwell for their insights and constructive discussions. Furthermore, special thanks to Drs. Yak-Nam Wang, Gilles Thomas, Katie Ponomarchuk, and Randy Williams for their help and suggestions in many experiments.

Additionally, I want to thank all of the incredible people in the Center for Industrial and Medical Ultrasound (CIMU), especially my fellow Ph.D. students, Yash and Pratik, who created many great memories, including our weekly acoustic studies, journal clubs, and outings.

Last but not least, I am deeply thankful to my wife, Jinny, for the unconditional support, trust, and love. Without her support, I could never have successfully completed this journey.

DEDICATION

To my adorable daughters, Sua and Leah,

who have taught me the meaning of true love.

Chapter 1.
INTRODUCTION

1.1 MOTIVATION

This dissertation explores quantitative monitoring of residual cavitation bubbles within the targeted tissue region induced by the high-intensity focused ultrasound (HIFU) pulses, using the ultrasound Doppler imaging modality. The research primarily investigates two distinct phenomena: rapidly dissolving cavitation bubbles induced by less destructive pulsed HIFU (pHIFU) and swiftly moving cavitation bubbles induced by boiling histotripsy (BH). Both pHIFU and BH use a series of HIFU pulses, but there are notable differences between these two HIFU regimes. pHIFU generally induces a sparse distribution of cavitation activity, causing mild tissue disruption and hemorrhage, whereas BH specifically induces local boiling and the formation of a vapor cavity within tissue. This promotes atomization and complete liquefaction of tissues through the use of higher amplitude and longer pulses compared to those used in pHIFU.

The motivation for this research originates from the need for real-time quantitative metrics that accurately represent the level of tissue damage or liquefaction during the cavitation-based HIFU treatments. These metrics can be used to determine the specific endpoint of the treatment, ensuring that the tissue reaches the desired state and thereby improving the efficiency of the treatment. Several critical aspects influence the development of these metrics. First, the metrics should be universally applicable, independent of any specific hardware system. This leads to the fact that the metrics represent physical quantities, whose units are derived from basic mechanical units such as length, mass, and time. Another aspect is that the metrics must be calculable within

an allowable computation time for the real-time implementation. For the target HIFU regimes–pHIFU and BH–a computation time of below 1 second is considered feasible. Finally, the metrics should be tested in *in vivo* setting, with a focus on correlating them with the status of the tissue being treated. Together, this research investigates the development of effective and reliable metrics for monitoring and controlling cavitation-based HIFU treatment, specifically within the pHIFU and BH regimes.

1.2 BACKGROUND

1.2.1 *High-Intensity Focused Ultrasound (HIFU)*

High-intensity focused ultrasound (HIFU) is an advanced biomedical technique that utilizes sound waves to precisely treat abnormal tissue without invasive interventions. Originating from the innovations of the Fry brothers, who first developed a pioneering device for concentrating high-ultrasound energy into targeted areas to destroy localized regions associated with neurological disorders[1], [2], HIFU has evolved considerably. Today, the capability of HIFU have become significantly diverse across both clinical and research settings, including hyperthermia treatment, breaking down kidney stone, immunotherapy, modulating tumor microenvironment, and ablating cancer cells [2], [3], [4].

HIFU is typically realized with a concave transducer that has a spherically curved surface. This design allows the low amplitude sound waves generated from transducer's surface to propagate through the medium (*e.g.* water, tissue), and converge at the localized area. This results in constructive interference of the sound waves, yielding a high-intensity region at the focal point (Figure 1.1). In the general HIFU regime, the operational frequency typically ranges from 0.5 to 3 MHz, depending on the specific needs for each treatment such as the focal amplitude, size, and penetration depth inside the tissue. The acoustic intensities at the focus range from 100 to 10,000

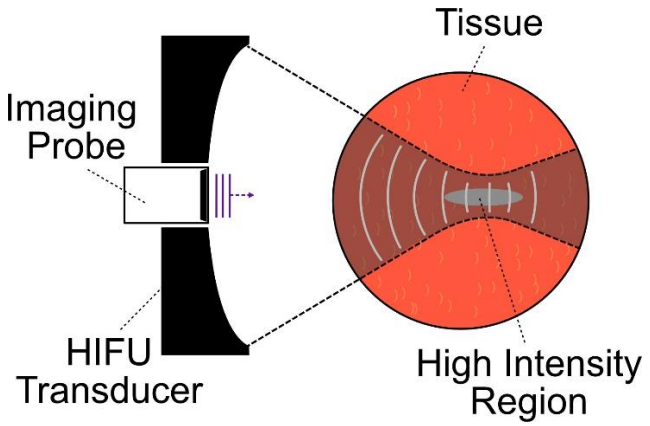

Figure 1.1. Schematic of a high-intensity focused ultrasound (HIFU) transducer and an ultrasound imaging probe for treatment monitoring.

W/cm^2, and the focal size is 1-3 mm in lateral diameter (*i.e.* width) and 5-10 mm in axial length (*i.e.* depth).

When delivering HIFU waves to the biological tissue, two distinct bioeffects can be induced: thermal and mechanical effects. The thermal effect is a result of the absorption of HIFU energy at focus, leading to conversion into heat and temperature rise. This localized heating can be used for thermotherapy applications while controlling mild temperature rise. With excessive heating, this can cause coagulative necrosis and cauterization, effectively ablating anomalous tissue or burning blood vessels [2], [5], [6], [7]. On the other hand, mechanical bioeffects involve acoustic cavitation and acoustic radiation force (ARF), becoming the key mechanisms underlying recent ultrasound therapy advancements. Figure 1.2 categorizes the recently advanced focused ultrasound techniques that use mechanical bioeffects with respect to the associated focal peak negative pressure levels. In low-intensity focused ultrasound regime where the peak negative pressure level below 1 MPa is used, the focused ultrasound can be utilized within delicate tissue like brain for modulating neural activities or blood brain barrier opening. The pressure below 5 MPa can be used for drug delivery enhancement with an administration of microbubbles, a synthetic micron size bubbles generally used for the ultrasound contrast agent. The peak negative pressure level above 5 MPa is

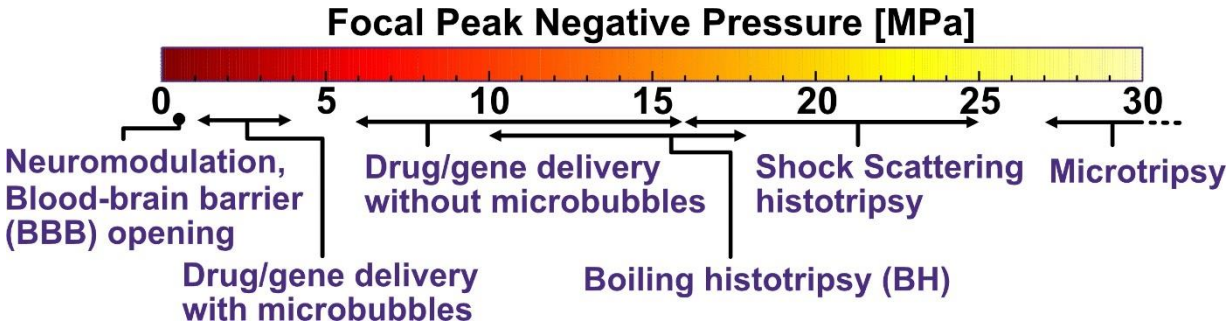

Figure 1.2. Focused ultrasound therapy techniques that facilitate mechanical bioeffects with associated focal peak negative pressure levels. Note that pHIFU regimes generally includes the applications where the focal peak negative pressure level above 5 MPa

typically categorized as HIFU regime, used for the various applications including the drug delivery enhancement without the needs for microbubbles, tumor microenvironment modulation, and mechanical tissue ablation, termed as histotripsy.

1.2.2 *Pulsed HIFU-induced Cavitation*

Acoustic cavitation is the formation of gas and/or vapor-filled bubbles ranging from micron to millimeter sizes within tissue, which interact with the acoustic fields, yielding mechanical effects on surrounding tissue. Each period of acoustic wave exerts compressional and rarefactional pressure, resulting in the contraction and expansion of cavitation nuclei sufficiently pre-existing in the surrounding tissue. These interactions are inherently an asymmetric process, commonly known as rectified diffusion. This means that cavitation nuclei take longer time to expand than to compress, causing the growth in size and stability for cavitation [8].

Pulsed HIFU (pHIFU), characterized by a series of short HIFU pulses (1 μs to 1 ms) with a low pulse repetition frequency (PRF) of 1 to 1 kHz and low duty cycle (<5%), is capable of inducing the sparse distribution of acoustic cavitation within tissue. This type of cavitation is also known as *de novo* cavitation, which means that the cavitation is generated directly by HIFU pulses without the need for microbubble administration. The interaction between pHIFU and cavitation

in tissue allows the cavitation to undergo radical changes in size, applying the high stress and strain onto surrounding tissue. In addition to stable oscillation of cavitation, this interaction can promote cavitation collapse (*i.e.* inertial cavitation), resulting in destructive effects in tissue, which can range from minor disruptions with petechial hemorrhage to full mechanical ablation into subcellular debris or liquefaction of the targeted tissue area. To ensure clarity and differentiate from histotripsy–a specialized form of pHIFU that employs specific mechanisms described in a subsequent section to achieve subcellular ablation or tissue liquefaction–the term "pHIFU" will hereinafter refer to all less destructive methods that do not attain the pulse intensity and mechanisms characteristic of histotripsy. pHIFU has been investigated in tumor permeabilization to enhance passive diffusion of systemically administered drugs [9], [10], [11], and inducing changes in tumor and benign tissue microenvironment [12], [13], [14], [15].

1.2.3 *Boiling Histotripsy*

Histotripsy is a mechanical tissue ablation technique that minimizes thermal damage. Unlike the thermal ablation technique where not only abnormal tissue but the nearby normal tissue may be thermally damaged due to heat diffusion, histotripsy generates clear boundaries between liquefaction and intact tissue area. Histotripsy is further categorized into cavitation histotripsy (CH) and boiling histotripsy (BH), depending on the specific pulsing parameters and the tissue liquefaction mechanism.

CH utilizes the cavitation cloud–a dense collection of cavitation spanning axially around 4 – 6 mm and laterally 1 – 2 mm [16]–within the tissue induced by 0.25 – 5 MHz microsecond-length ($< 80\ \mu s$) pulses at PRF of 5 – 1,000 Hz with high peak negative pressure level ($\sim$30 MPa) at focus [17]. The tissue fractionation mechanism of CH mirrors the process of fatigue failure in material science. During CH treatment, the cavitation cloud exerts cyclic stress onto surrounding tissues

through repeated expansion and collapse with each period of CH pulse, leading to the disruptions and fractionation of the tissue [18]. CH can be further divided into two techniques based on the generation of the cavitation cloud: shock-scattering histotripsy [16], and intrinsic threshold histotripsy (*i.e.* microtripsy) [19].

Boiling histotripsy uses millisecond-length HIFU pulses, ranging from 1 to 10 ms with peak negative pressures ranging between 9 and 19 MPa, at relatively low PRF of 1-10 Hz. A crucial aspect of BH involves the formation of shock fronts exceeding 40 MPa, driven by the nonlinearity of the tissue and the propagation of high-amplitude BH pulses. This swiftly raises tissue temperatures to boiling levels, forming millimeter-sized vapor cavities. The efficiency of this heating process is proportional to the cube of the shock amplitude [20], [21]. Once the vapor cavities are formed, the subsequent interactions between these cavities and shock fronts lead to the tissue fractionation mechanisms such as atomization, microfountain [22], [23], and the formation of cavitation cloud proximal to the vapor cavity [24], [25]. The process results in tissue liquefaction with subcellular debris. BH has been explored in various applications, ranging from tumor ablation in organs such as the liver [26], [27], [28], kidney [26], and prostate [29], [30], [31], [32], to the treatment of large hematomas [33], abscesses [34], [35], and enhancing anti-tumor immune responses in clinical and pre-clinical settings [30], [36], [37].

1.2.4 *Cavitation Monitoring Methods*

Real-time cavitation monitoring is an essential part of the cavitation-based HIFU therapy. Given that cavitation or residual bubbles act as high-contrast scatterers for ultrasound waves, ultrasound imaging-based monitoring methods are primarily employed. The methods are realized by an ultrasound imaging probe that is mounted coaxially with the HIFU transducer, as shown in

Figure 1.1. This type of imaging probe typically consists of 64 – 128 elements arranged linearly within 2 – 5 cm width.

1.2.4.1 B-mode

B-mode ultrasound (*i.e.* brightness mode) is the most widely used ultrasound imaging method. It is based on a pulse-echo scheme where multiple focused imaging pulses (*i.e.* ray-lines) are transmitted, and the signals backscattered from tissue are received and processed into a 2-dimensional map that displays the signal intensity backscattered from each location in tissue. The signal intensity is represented by the brightness of the image, hence the term "brightness mode" or B-mode.

B-mode is often considered as the first option for cavitation imaging due to its effectiveness in capturing the phenomenon [6]. This is attributed to the significant impedance difference at the air-tissue interface of cavitation bubbles, which cause the strong backscattering of imaging pulses. In both pHIFU and BH regimes, B-mode imaging is typically synchronized to capture between HIFU pulses [12], [26]. This allows for the detection of residual bubbles that are generated during the HIFU pulses and persist for durations ranging from a few hundred microseconds to several seconds. While B-mode is effective for targeting HIFU pulses, its application in evaluating tissue damage/liquefaction levels is limited due to the lack of corresponding quantitative metrics. Moreover, the tissue itself can produce clutter scattering, which is often considered noise in terms of cavitation monitoring.

1.2.4.2 Passive Methods

Passive cavitation detection (PCD) is another commonly used method for monitoring cavitation, passively recording–or "listening to"–the acoustic emissions produced by cavitation activity during the HIFU pulse. PCD is recognized for its sensitivity and cost-effectiveness as a

real-time cavitation monitoring tool [38]. Furthermore, analyzing the spectrum of PCD signals allows for the differentiation between stable and inertial cavitation activity. Stable cavitation is characterized by the frequency of the HIFU and its harmonics, whereas inertial cavitation is identified by a broadband signal resulting from the shock wave emissions during bubble collapse [20], [39].

In general, a single element flat or focused transducer is used for acquiring PCD signal. This setup can lead to difficulties in specifically identifying the spatial distribution of cavitation. To address this limitation, passive acoustic mapping (PAM) or passive cavitation imaging (PCI) method has been explored by using multielement array transducer and receive beamforming technique [40], [41], [42], [43]. However, these passive mapping techniques also have limited axial resolution, which becomes even more problematic when the imaging probe has a small aperture relative to the depth of the region of interest (ROI). This is indeed the case with the setup used in this study.

1.2.4.3 Ultrasound Doppler

Ultrasound Doppler was originally developed to measure blood flow speed and is the second most common tool in diagnostic ultrasound, following B-mode. As the name suggests, this technique leverages Doppler phenomena, which is the frequency shift observed when a sound source or receiver is in motion. The early ultrasound Doppler tool was a spectral Doppler echocardiography using either continues or pulsed wave Doppler, which displays the spectrum of the received signal to measure the blood speed at the specific location [44]. Doppler technique now provides a two dimensional Doppler velocity map (*i.e.* color Doppler) with allowable computation time based on the autocorrelation suggested by Kasai [45].

Doppler ultrasound can also be effective for monitoring cavitation [46], [47]. Similar to B-mode, a Doppler ensemble is acquired between HIFU pulses to detect residual cavitation bubbles that persist after the termination of HIUF pulse. This bubble-induced Doppler method has been found to be more sensitive for detecting bubbles compared to B-mode, because the rapid dissolution of bubbles is interpreted as motion by the Doppler algorithm [46].

1.3 Organization of the Dissertation

This dissertation consists of six chapters, including introduction and conclusion. Four main chapters (Chapter 2 through 5) are formatted as independent articles, each of which has its own introduction, methods, results, and conclusion sections. This is meant to be a useful resource and reference, allowing each chapter to be understood on its own without the necessity of reading the entire dissertation.

In this first chapter, the motivation and several foundational backgrounds are presented, including basic concepts of HIFU, HIFU induced cavitation, and current monitoring methods for cavitation. In Chapter 2, a novel Doppler technique that uses dynamic mode decomposition (DMD) is introduced, which enables both imaging and extracting temporal characteristics of fast-dissolving cavitation bubbles induced by moderate pulsed HIFU regime. The performance of the proposed technique was evaluated through pHIFU exposures *in silico* and *ex vivo*. In Chapter 3, the DMD-based Doppler was applied in *in vivo* pig's tissues, and the corresponding metrics were correlated with the tissue damage levels assessed by the histological images. Chapter 4 focuses on measuring BH-induced translational velocities of swiftly moving residual bubbles within the liquefied tissue volume using color Doppler. Several metrics are proposed to track the progression of tissue liquefaction, depending on the size of the treated volume. Chapter 5 details Doppler measurement of BH-induced bubbles conducted in *in vivo* pig's tissues. Doppler metrics were

correlated with the tissue liquefaction level assessed by the histological images. Finally, Chapter 6 summarizes and concludes my doctoral research, offering suggestions for future research.

Chapter 2.
DYNAMIC MODE DECOMPOSITION FOR TRANSIENT CAVITATION BUBBLE IMAGING IN PULSED HIFU THERAPY[1]

2.1 INTRODUCTION

Pulsed high-intensity focused ultrasound (pHIFU) is a therapeutic ultrasound approach in which sparse *de novo* inertial cavitation is induced in tissue without the introduction of exogenous contrast agents, (e.g. microbubbles), resulting in mild mechanical disruption of the targeted tissue. pHIFU uses short (1-100 ms) pulses delivered at low duty cycle (<5%) and relatively low frequency (around 1 MHz) to avoid thermal effects and promote cavitation [9], [10], [12], [13], [14], [15], [48], [49]. This regime was explored in conjunction with several clinical applications, including tumor permeabilization to enhance passive diffusion of systemically administered drugs [9], [10], [11], and inducing changes in tumor and benign tissue microenvironment [12], [13], [14], [15].

The pHIFU treatments are commonly performed under real-time ultrasound (US) imaging guidance; conventional B-mode imaging with a probe integrated coaxially into the HIFU transducer is typically used for treatment planning and targeting. However, B-mode US has low sensitivity for detection of cavitation activity during treatment because of the transient nature of the bubbles and their rapid dissolution after HIFU pulse [48], [50]. Furthermore, even in cases

[1] *© 2024 IEEE. Reprinted, with permission, from Minho Song et al. "Dynamic Mode Decomposition for Transient Cavitation Bubbles Imaging in Pulsed High Intensity Focused Ultrasound Therapy", IEEE Transactions on. Ultrasonics, Ferroelectrics, and Frequency Control, Vol. 71, No.5 (2024).*

where cavitation can be discerned in B-mode images as a hyperechoic region, this method does not provide a quantitative metric of cavitation or the resulting tissue disruption.

Conversely, passive methods, including passive cavitation detection (PCD) and passive acoustic mapping (PAM), quantify broadband acoustic emissions resulting from cavitation collapses (i.e. inertial cavitation) during HIFU pulses [43], [48]. These passive methods provide a sensitive quantitative metric of cavitation activity, but not of the resulting tissue damage, and the spatial information on cavitation occurrence is limited (e.g. axial resolution in PAM).

Bubble Doppler imaging is another active ultrasound method that was found to be more sensitive than B-mode and provide better spatial resolution than PAM in mapping bubbles induced by pHIFU [46], [51], [52], [53]. In Bubble Doppler each HIFU pulse is immediately followed by an ensemble of planewave Doppler pulses. Those pulses encounter a distribution of residual cavitation bubbles that are rapidly (i.e. within milliseconds or the duration of the ensemble) changing due to dissolution. Doppler processing algorithm interprets those changes as motion, and thus the distribution of bubbles is displayed as an area of high Doppler power. The velocity associated with this area of high Doppler power is typically randomly fluctuating around zero, as the bubbles are not actually moving, only changing in size [46]. This creates a problem with selection of the wall filter used in conventional Doppler signal processing to remove clutter from stationary of slowly moving tissue: signal from nearly stationary yet temporally transient cavitation bubbles may be inadvertently filtered out. Furthermore, although Doppler power was found to correlate with PCD-derived broadband emissions, it does not provide any quantitative information on the cavitation bubble parameters, such as size or dissolution time, that could be linked to the level of tissue disruption.

One well-established wall filter is the infinite impulse response (IIR) high pass filter, which eliminates low frequency components from signals in the Doppler ensemble domain (i.e. slow time). This filter is effective when tissue motion is considerably slower than the motions of interest (e.g. blood flows speed vs surrounding tissue motion), and when prior knowledge about the appropriate cut-off frequency is available. However, the design of high pass filter and the cut-off frequency selection can be challenging in pHIFU-induced transient bubbles imaging due to the limited temporal sampling points during the bubbles' lifespan [52]. Moreover, the quality of IIR filter can be degraded by transient clutter signal from HIFU reverberation.

Another commonly used wall filter in blood flow imaging, also proposed for cavitation imaging[52], [53], is singular value decomposition (SVD) filter [54]. The SVD filter decomposes a matrix of beamformed images, where each column is reshaped from an image corresponding to a Doppler ensemble pulse, into spatiotemporally coherent patterns (i.e. modes). These modes are orthogonal to one another and characterized by singular values that indicate the dominance of each mode. Filtering is achieved by reconstructing the image using a selective set of modes corresponding only to the tissues and motion of interest. The primary assumption underlying SVD filtering is that the amplitude of the clutter signal from background tissue consistently exceeds that from scatterers of interest, therefore, the modes corresponding to several largest singular values are removed. However, the amplitude of the backscattered signals from de novo cavitation bubbles can be comparable or even larger than those from tissue, making a priori mode selection challenging. Furthermore, because the residual bubbles typically dissolve within a few milliseconds after the HIFU pulse [46], a limited number of Doppler ensemble pulses can be acquired to capture the bubbles, resulting in degradation of the quality of SVD filter.

We propose the use of dynamic mode decomposition (DMD) as a technique to address the limitations of Bubble Doppler signal processing discussed above, namely – improve the reliability and sensitivity of detecting and mapping the cavitation bubbles and providing quantitative information on their parameters. DMD is a data-driven technique to analyze the dynamics of complex phenomena [55]. This technique originated in fluid dynamics to understand the coherent structures and patterns of high dimensional complex fluid flows [56], [57], but it then extended to various other fields including robotics control [58], imaging processing [59], neuroscience [60], plasma physics [61], and finance [62].

DMD decomposes time-series data into a reduced-order set of spatiotemporal modes, each of which consists of spatially coherent patterns and has the same behavior in time. While both SVD and DMD extract spatiotemporal information from the time-series snapshots, significant distinctions exist between the two. The spatial modes of SVD are not affected by the temporal order or arrangement of the input snapshots. In essence, SVD treats the input data more like a collection of images, focusing on its intrinsic structure and relationships between the individual images, rather than the temporal order in which the input data was collected. In contrast, DMD considers and captures both the intrinsic structure of the snapshots and their physically meaningful time behavior. Here, the DMD modes were assumed to represent quasi-harmonic motion with exponential growth or decay in amplitude. This is the most basic DMD implementation, but it matches the temporal behavior of Doppler signals backscattered from dissolving bubbles [46].

In this chapter, the feasibility of applying DMD processing for mapping the pHIFU-induced transient bubbles and identifying their temporal behavior was investigated. First, the performance of DMD was tested and compared to SVD and IIR high pass filtering in a numerically simulated image series that combined four different spatial patterns with varying time behaviors.

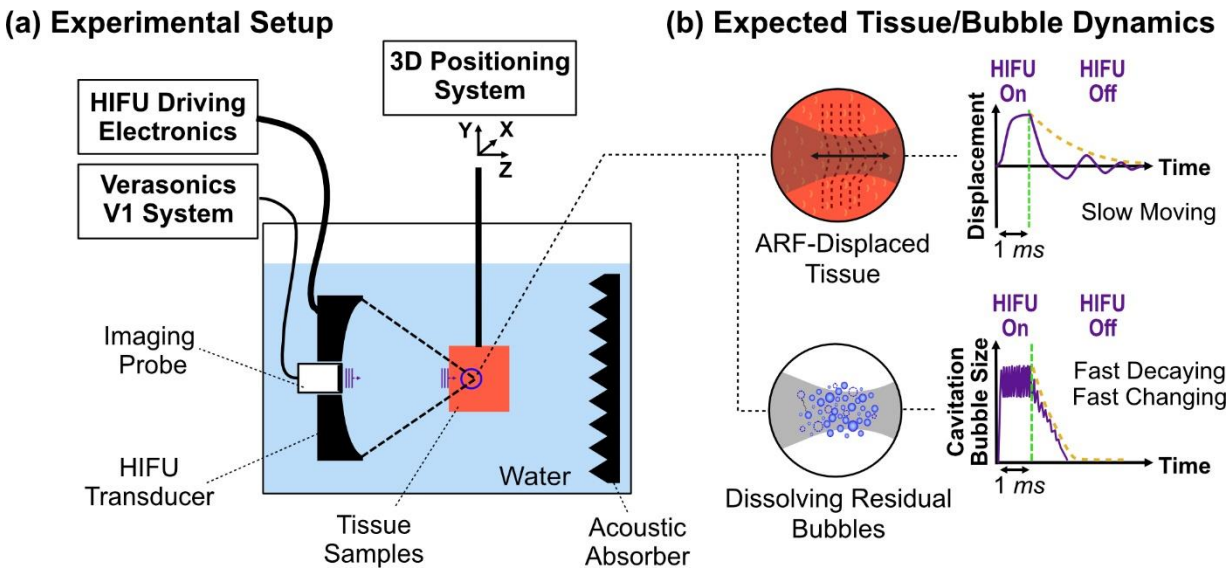

Figure 2.1. Schematic of (a) the experimental setup for pHIFU exposure in ex vivo bovine tongue tissue, (b) expected tissue and bubble dynamics. The elastic rebound motion of tissue displaced by acoustic radiation force was expected to be relatively slow with very gradual decay, whereas the distribution of residual cavitation bubbles of varying sizes was expected to rapidly change and dissolve.

Subsequently, DMD processing was applied to the planewave Doppler datasets acquired from pHIFU treatment of *ex vivo* tissue.

2.2 METHODS

2.2.1 *Experimental Arrangement and pHIFU Exposure Parameters*

Figure 2.1(a) shows the general schematic of the experimental setup that was used in the pHIFU exposures of *ex vivo* bovine tongue tissue. A 1.5 MHz HIFU transducer (8 cm aperture size, 6 cm focal distance and a 2 cm circular central opening) was controlled by high power driving electronics—a custom built 12-channel class D amplifier system [63], [64]. A 64-element ATL P7-4 ultrasound imaging probe was mounted at the center opening of the HIFU transducer and connected to Verasonics V1 system to acquire the planewave Doppler imaging data. The transducer assembly was mounted in a tank filled with degassed, deionized water. The *ex vivo*

tissue sample was placed in front of the transducer in a holder attached to a 3D positioning system (Velmex Inc., Bloomfield, NY, USA), such that the HIFU focus was at a depth of 1 cm. The pHIFU pulsing protocol was the same as that previously used by our group for cavitation-based permeabilization of tissue [9], [46], [64]: pulse duration 1 ms, pulse repetition frequency (PRF) 1 Hz. During each HIFU pulse, the US imaging probe was operated in passive mode at a sampling rate of 20 MHz, to record broadband emissions from cavitation bubbles. The radio frequency (RF) signals were then bandpass and comb-filtered to remove backscattered HIFU harmonics and summed across the 64 channels with beamforming delays corresponding to the location of HIFU focus. The binary indicator of cavitation occurrence was obtained from the resulting PCD signal, and it was used to confirm the cavitation activity of the acquired dataset.

Each HIFU pulse was immediately followed by a 5 MHz planewave Doppler ensemble consisting of 14 pulses at PRF of 3 kHz. Two different HIFU output levels were selected to achieve *in situ* focal pressure levels above and below the cavitation threshold. The *in situ* peak positive and negative pressures were calculated using hydrophone measurements in water reported previously [64] and a derating procedure for nonlinear waveforms [65] using attenuation coefficient of 0.044 Np/cm [66] with 1 cm depth in tissue, and were 20.9 / -9.4 MPa, and 72.3 / -12.7 MPa, respectively. A pHIFU exposure was delivered to 4 different focus locations per output level for a total of 8 focus locations. The exposures consisted of 30 (for non-cavitation cases) or 60 (for cavitation cases) HIFU pulses. The results were similar across treatment locations for each output level.

The bovine tongue tissue sample was obtained from a local abattoir and kept on ice until use within 48 hours. The choice of the bovine tongue was based on its anatomical structure, characterized by the interweaving of muscle bundles with fatty tissue, which presented a good cavitation probability [48]. The tissues were trimmed, cut fibrous surface, degassed in saline for 1

hour in a desiccant chamber, and embedded in low melting point agarose gel (UltraPure Agarose; Invitrogen) to facilitate its placement in the holder.

2.2.2 *Dynamic Mode Decomposition*

2.2.2.1 Underlying Assumptions

The target of DMD processing was to capture changes in the planewave Doppler imaging pulses backscattered from the HIFU focal area immediately after each HIFU pulse. The changes were expected to result from two phenomena: rapid dissolution of the cavitation bubbles of varying size and at varying rate, and slow elastic tissue rebound motion induced by acoustic radiation force (ARF) associated with the HIFU pulse, as shown in Figure 2.1(b). We hypothesized that the captured changes in reconstructed images over slow time can be represented by a low-dimensional set of patterns, with each of these patterns associated with specific factors (e.g. cavitation or tissue motion) contributing to the observed changes. Additionally, linear approximation of the system dynamics was used as the simplest case, described by coupled linear differential equations:

$$\frac{d}{dt}\boldsymbol{X} = \boldsymbol{M}\boldsymbol{X}, \tag{2.1}$$

where $\boldsymbol{X}$ is a matrix of backscattered pulses that reflects the dynamics of tissue and bubbles, and $\boldsymbol{M}$ is a linear operator that reveals the dynamics of matrix $\boldsymbol{X}$. The linear approximation was expected to be adequate due to the limited number of temporal acquisition points (i.e. the number of pulses in the Doppler ensemble) within the bubbles' lifespan.

2.2.2.2 DMD Processing

Although DMD has been a prominent research field in recent years with many variations and advanced techniques developed, in this work we used the most basic implementation—exact DMD—suggested by Tu et al [67]. The data for pre-processing of DMD was constructed similarly

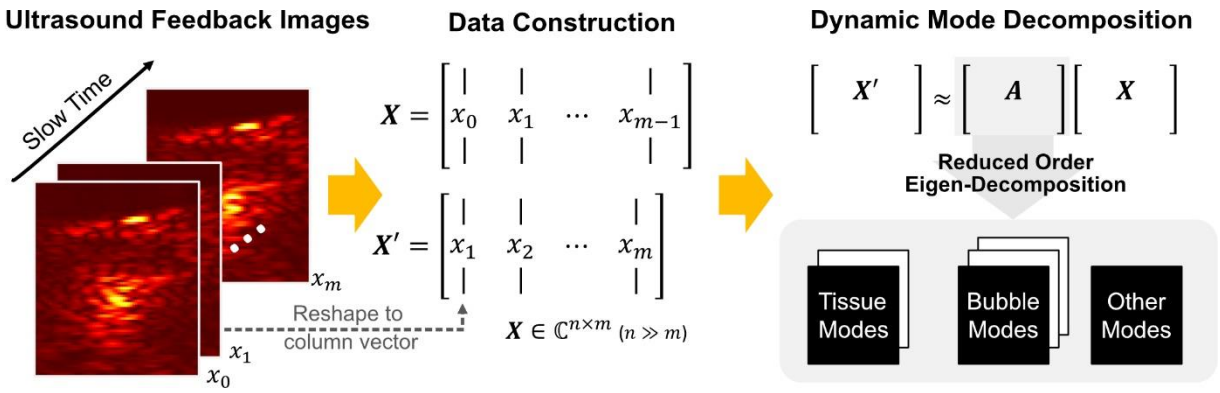

Figure 2.2. Schematic of the DMD processing. The scan-converted I/Q data were reshaped and stacked to form $\boldsymbol{X}$ and $\boldsymbol{X'}$ matrices with one time-step shift relative to each other. The DMD provides reduced ordered eigenvalues and DMD modes of $\boldsymbol{A}$ matrix which is the best-fitted operator satisfying $\boldsymbol{X'} \cong \boldsymbol{AX}$. These modes can be physically interpretable as motion and/or changes in tissue or bubbles.

to the general matrix formulation of SVD clutter filtering used in conventional Doppler imaging [54]. The input data were m+1 2D scan-converted in-phase and quadrature (I/Q) components acquired by Verasonics in slow time (labeled as $x_0, x_1, \cdots, x_m$), where m+1 is the number of pulses in Doppler ensemble. The total number of pixels in a single image (x_i, i =0, 1, ⋯, m) was n with grid size corresponding to the one wavelength of Doppler ensemble pulse (~0.3 mm).

As illustrated in Fig. 2.2, each 2D I/Q dataset was reshaped into a column vector by attaching one column under the other in left-to-right order, and stacked into $\boldsymbol{X}$ and $\boldsymbol{X'}$ matrices each having m columns and one time step shifted from one another (i.e. $\boldsymbol{X}$ contains x_0 to x_{m-1} and $\boldsymbol{X'}$ contains x_1 to x_m). Then, the discrete time version of Eq. (2.1) could be written as

$$\boldsymbol{X'} = \boldsymbol{AX}, \tag{2.2}$$

where $\boldsymbol{A} = exp(\boldsymbol{M}\Delta t)$ and Δt is time step in slow time. Notably, the number of rows (n) of the matrices $\boldsymbol{X}$ and $\boldsymbol{X'}$, corresponding to the total number of pixels in a planewave Doppler image, was on the order of 10^3 in this study. It is usually much larger than the number of columns (m), which was on the order of 10.

In (2.2), the matrix $\boldsymbol{A}$ fully describes the temporal evolution of the image dataset $\boldsymbol{X}$. However, the direct calculation of $\boldsymbol{A}$, as defined by

$$\boldsymbol{A} = \underset{\boldsymbol{A}}{\operatorname{argmin}} \|\boldsymbol{X}' - \boldsymbol{A}\boldsymbol{X}\|_F = \boldsymbol{X}'\boldsymbol{X}^{\dagger}, \tag{2.3}$$

involves a computationally demanding process given that the dimensions of matrix $\boldsymbol{A}$ are $n \times n$. In Eq. (2.3), $\underset{\boldsymbol{A}}{\operatorname{argmin}}$ denotes the process of determining the matrix $\boldsymbol{A}$ at which the argument attains its minimum, $\|\cdot\|_F$ is the Frobenius norm, and † indicates the pseudo-inverse. Instead of this direct computation, the exact DMD provides a reduced order set of exact eigenvalues and eigenvectors of matrix $\boldsymbol{A}$. Specifically, a rank-r approximation of eigen-decomposition of $\boldsymbol{A}$ can be expressed as

$$\boldsymbol{A} \cong \boldsymbol{\Phi}\boldsymbol{\Lambda}\boldsymbol{\Phi}^{-1}, \tag{2.4}$$

where $\boldsymbol{\Phi}$ is an $n \times r$ matrix, its r columns of length n are eigenvectors of $\boldsymbol{A}$, $\boldsymbol{\Lambda}$ is an $r \times r$ diagonal matrix in which each diagonal element is an eigenvalue of $\boldsymbol{A}$, and the superscript -1 denotes the inverse of the given matrix. The objective of DMD is to derive matrices $\boldsymbol{\Phi}$ and $\boldsymbol{\Lambda}$. A comprehensive outline of the corresponding procedure is detailed in reference [67]; below is a brief summary:

a) Compute the SVD of the reconstructed dataset $\boldsymbol{X}$.

$$\boldsymbol{X} = \boldsymbol{U}\boldsymbol{\Sigma}\boldsymbol{V}^{*}, \tag{2.5}$$

where the columns of $\boldsymbol{U}$ and $\boldsymbol{V}$ are right and left singular vectors with orthogonality that represent spatial modes and temporal coefficients, respectively, $\boldsymbol{\Sigma}$ is a diagonal matrix that has at most m non-zero singular values, and the superscript asterisk denotes the complex conjugate transpose.

b) Truncate the SVD matrices to rank-r by selecting the first r singular values in a descending order and corresponding columns of $\boldsymbol{U}$ and $\boldsymbol{V}$. ($r \leq m$). Similar to SVD, the determination of the best-optimized rank r is a crucial step in DMD. For example, if the rank is too low, there is a risk of intertwining tissue and bubble modes, and if it is too high, meaningless clutter modes could complicate the interpretation of the modes and identifying modes associated with bubbles. In this study, r was determined when the summation of first r singular values exceeded 97% of that of all singular values ($\sum_{k=1}^{r} \sigma_k > 0.97 \cdot \sum_{k=1}^{m} \sigma_k$, where σ_k is a k[th] singular value or diagonal term of matrix $\boldsymbol{\Sigma}$).

$$\boldsymbol{X} \cong \boldsymbol{U}_r \boldsymbol{\Sigma}_r \boldsymbol{V}_r^*, \tag{2.6}$$

Where the subscript r indicates rank- r truncation of given matrix, such that the dimension of $\boldsymbol{U}_r$, $\boldsymbol{\Sigma}_r$, and $\boldsymbol{V}_r^*$ are $n \times r$, $r \times r$, and $r \times m$, respectively. Then, approximate A could be rewritten by substituting Eq. (2.6) into Eq. (2.3), as

$$\boldsymbol{A} \cong \boldsymbol{X'} \boldsymbol{V}_r \boldsymbol{\Sigma}_r^{-1} \boldsymbol{U}_r^*, \tag{2.7}$$

c) Compute the reduced order $r \times r$ matrix $\boldsymbol{A_r}$, which is a similarity transformation matrix of $\boldsymbol{A}$.

$$\boldsymbol{A_r} = \boldsymbol{U_r^* A U_r} = \boldsymbol{U_r^* X' V}_r \boldsymbol{\Sigma_r^{-1}}. \tag{2.8}$$

d) Compute the eigen-decomposition of $\boldsymbol{A_r}$.

$$\boldsymbol{A_r} = \boldsymbol{W \Lambda W^{-1}}, \tag{2.9}$$

where $\boldsymbol{W}$ is the matrix whose columns are eigenvectors of $\boldsymbol{A_r}$ and $\boldsymbol{\Lambda}$ is the diagonal matrix, whose diagonal elements are the eigenvalues of $\boldsymbol{A_r}$. Since $\boldsymbol{A_r}$ and $\boldsymbol{A}$ are related by matrix similarity, they share the same eigenvalues $\boldsymbol{\Lambda}$, but different eigenvectors.

e) Compute eigenvector matrix $\boldsymbol{\Phi}$ using Eqs. (2.4), (2.7), (2.8), and (2.9):

$$\boldsymbol{\Phi} = \boldsymbol{X'V_r\Sigma_r^{-1}W} = \begin{bmatrix} | & | & & | \\ \phi_1 & \phi_2 & \dots & \phi_r \\ | & | & & | \end{bmatrix}, \tag{2.10}$$

where ϕ_i is ith eigenvector (i.e. ith column vector of $\boldsymbol{\Phi}$).

2.2.2.3 DMD Modes and Eigenvalues

The diagonal elements of $\boldsymbol{\Lambda}$ and column vectors of $\boldsymbol{\Phi}$ obtained from Eqs. (2.9) and (2.10) represent the exact eigenvalue and corresponding eigenvector (DMD mode shapes) of matrix $\boldsymbol{A}$. The DMD mode shapes can be reshaped as 2D images, which are expected to correspond to physically interpretable modes such as planewave images of tissue and bubbles (Fig. 2.2). The continuous-time eigenvalue matrix $\boldsymbol{\Omega}$, defined as

$$\boldsymbol{\Omega} = \log \boldsymbol{\Lambda}/\Delta t = \begin{bmatrix} \omega_1 & 0 & \dots & 0 \\ 0 & \omega_2 & \dots & 0 \\ \vdots & \vdots & \ddots & 0 \\ 0 & 0 & \dots & \omega_r \end{bmatrix}, \tag{2.11}$$

indicates how each DMD mode shape evolves in time. Here, ω_i is ith continuous-time eigenvalue (i.e. ith diagonal element of $\boldsymbol{\Omega}$). The negative real part of ω_i corresponds to the temporal decay rate; the imaginary part corresponds to the angular frequency or rate of change.

2.2.2.4 Mode Classification and Reconstruction

Over the course of pHIFU treatment, the behavior of the transient bubbles at the focus is expected to change as the tissue becomes more disrupted. To identify and monitor these changes,

the discrete-time eigenvalues (i.e. diagonal elements of $\mathbf{\Lambda}$) were classified and tracked on the complex plane using k-means clustering method, which is a widely used method that groups dataset into k clusters by minimizing the distance between each data point and its cluster's centroid. Since the discrete-time eigenvalues for exponentially decaying dynamics are bounded by a unit circle on the complex plane, they are more suitable for clustering than continuous-time eigenvalues (ω_i). The classified eigenvalues and corresponding DMD mode shapes were then characterized with respect to the three metrics: frequency, temporal decay rate, and maximum power level of the DMD mode shape defined as $p_{max} = max(|\phi|^2)$. Based on the metrics, each DMD mode could be associated with the dynamics of tissue or bubbles, and selective reconstruction of those modes could be performed. A bubble mode reconstruction, for example, can be expressed as

$$\boldsymbol{x}_{bubble}(t) = \sum_{i,selected} \phi_i e^{\omega_i t} b_i, \tag{2.12}$$

where $i, selected$ indicates the index of selected modes that were interpreted as components of bubble mode and b_i is ith element of initial mode amplitude vector $\boldsymbol{b}$ related to the initial image x_0 (i.e. $\boldsymbol{b} = \mathbf{\Phi}^{\dagger} x_0$).

2.2.2.5 Connection of DMD Modes to Conventional Doppler Variables

Elimination of certain DMD modes can serve as a wall filter in conventional Doppler processing. For each DMD bubble mode, the consecutive bubble images in (Eq. 2.12) (e.g. $\boldsymbol{x}_{bubble}$ at t_1=Δt and t_2=$2\Delta t$) have a phase shift of $Im\{\omega\}\Delta t$ relative to each other over all the image pixels, where $Im\{\omega\}$ denotes the imaginary part of ω. This means that DMD processing directly provides the phase shift necessary for color Doppler estimation of velocity associated with each mode. Specifically, the angular frequency of a DMD mode (i.e. $Im\{\omega\}$)corresponds to Doppler phase shift, from which Doppler velocity is calculated as:

$$v = {Im\{\omega\}c_0}\Big/{4\pi f_{Img}}, \tag{2.13}$$

where c_0 is the sound speed in tissue and f_{Img} indicates the frequency of planewave Doppler imaging pulses. This also implies that a positive DMD frequency corresponds to motion directed towards the HIFU transducer, whereas a negative frequency corresponds to motion away from it.

2.2.3 *Evaluation of DMD Performance in a Numerical Example*

The performance of DMD was evaluated in a numerically simulated time series of images, meant to represent a simplistic motion from tissue and bubbles with PRF and number of pulses matching the experimental arrangement. The data were processed with DMD and by commonly used wall filters in conventional Doppler processing – SVD and IIR high pass filter – for side-by-side comparison. The similar comparison study between DMD and other modal decomposition methods – principal component analysis (PCA) and independent components analysis (ICA) – can be found in neuroscience paper [60]. As shown in Fig. 2.3(a), the data was a combination of four shapes $\boldsymbol{S}_1$, $\boldsymbol{S}_2$, $\boldsymbol{S}_3$, and $\boldsymbol{S}_4$: a square of uniform brightness, two circles with radially cosine distribution of brightness, and random noise, respectively. Each of them except random noise $\boldsymbol{S}_4$ was spatiotemporally coherent – brightness of all points of the shape had the same behavior in time. The input brightness data $\boldsymbol{X}[n]$ was thus defined as

$$\boldsymbol{X}[n] = \sum_{k=1}^{4} A_k \boldsymbol{S}_k e^{(-\alpha_k + i\cdot 2\pi\cdot f_k)\cdot \Delta t\cdot n}, \tag{2.14}$$

where A_k was the initial brightness amplitude of each shape, f_k was frequency (f_1= 50 Hz, f_2= 500 Hz, f_3= 550 Hz, and f_4= 0 Hz), α_k was temporal decay rate (α_1= 0.1 ms^{-1}, α_2= 2 ms^{-1}, α_3= 5 ms^{-1}, and α_4= 0 ms^{-1}), Δt was time step ($\Delta t = 0.33\, ms$, which corresponded to the experimentally allowable PRF of 3 kHz), and n was sample number or the virtual imaging pulse

number ($1 \leq n \leq 14$). At each time step, random noise $\boldsymbol{S}_4$ was repeatedly generated to ensure that there was no spatial or temporal coherence. The initial brightness amplitudes, frequencies, and temporal decay rates of the modes were chosen to approximate the ultrasound images of slowly moving tissue (the square) which typically dominates the image amplitude, and those of collections of bubbles (the two circles) which are quickly changing and dissolving. Note that each individual bubble is expected to be smaller than the spatial resolution cell of the ultrasound imaging, and thus the decay rate would correspond to that averaged across the collection of bubbles. The initial brightness amplitudes of each shape (A_1, A_2, A_3, and A_4) were 2, 1, 1, and 0.01, respectively. For tissue containing two bubble areas (A_2 and A_3), the amplitudes were designed to have signal-to-noise ratio (SNR) of 40 dB vs random noise level (A_4), and that of tissue (A_1) was set to be twice larger than A_2 or A_3. Fig. 2.3(b) shows the SNR changes of each mode over slow time. The brightness of the two area of bubbles ($\boldsymbol{S}_2$ and $\boldsymbol{S}_3$) rapidly decayed to below the random noise level within a few sampling points (3 sampling points (~ 1 ms) and 6 sampling points (~2.2 ms), respectively), which corresponded to a previously reported decay time for residual cavitation bubbles [46].

Three different methods were applied to the input data described above: DMD, SVD, and IIR high pass filter. In SVD, the data processing followed the same procedure as that described for DMD until step b). IIR high pass filter with the cut-off frequency of 275 Hz and order 3 was utilized to eliminate the image of background tissue (i.e., $\boldsymbol{S}_1$). To assess the robustness of the DMD from random noise $\boldsymbol{S}_4$, the simulation was repeated n=1000 times with random noise regenerated every time. Mean and standard deviation of the frequency and temporal decay rate for each DMD mode, as measured by each of the processing methods, were obtained and compared to ground truth.

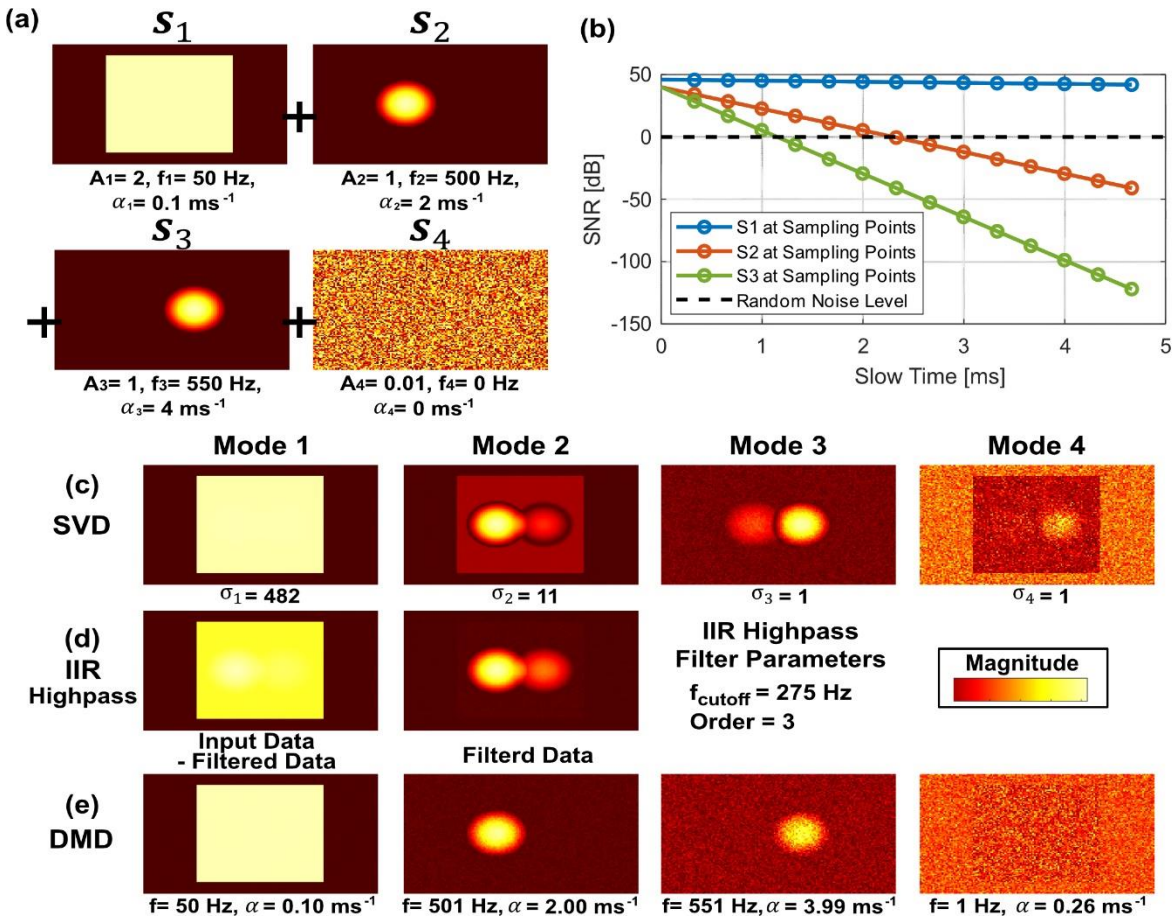

Figure 2.3. Numerical example for testing DMD performance vs SVD and IIR high pass filter. (a) The input data consisting of four components of simulated 2D scan data: a square image with high amplitude, low frequency, and low decay rate, simulating tissue backscatter (S1), left and right-side circles inside the square with low amplitude, high frequency, and high decay rate (S2, S3), simulating backscatter from bubbles, and a low amplitude random noise without any coherence in space and time (S4). (b) Illustration of the amplitude decay for each component of input data across slow time. The amplitude was expressed in SNR, as compared to the random noise level. Separation of modes from numerical example with the different filtering methods: SVD, IIR highpass, and DMD. (c) Four SVD modes corresponding to the first four columns of SVD $\boldsymbol{U}$ matrix with corresponding singular values σ. (d) IIR high pass filtered data and its subtraction from original data. (e) Four DMD modes and their corresponding frequencies and temporal decay rate.

Table 2.1. The Statistical Results of Frequency and Temporal Decay Rate Estimation by DMD (N=1000)

		Mode 1	Mode 2	Mode 3
f [Hz]	Ground truth	50	500	550
	Mean	49.980	500.293	553.160
	Std	0.007	0.763	3.431
α [ms^{-1}]	Ground truth	0.1	2	4
	Mean	0.1008	2.0003	4.0093
	Std	0.0001	0.0034	0.0189

2.3 RESULTS

2.3.1 *Evaluation of DMD Performance in the Numerical Example*

Fig. 2.3(c), (d), and (e) display representative cases of the numerical dataset processed with the three methods: the first four columns of SVD $\boldsymbol{U}$ matrix with the corresponding singular values (σ), the result of IIR high pass filter, and four DMD modes along with their corresponding frequency (f) and temporal decay rate (α), respectively. For DMD, each mode image, and corresponding values of f and α were very consistent across repeated simulation with regenerated random noise. Table 2.1 shows the mean and standard deviation of f and α estimated by DMD. As seen, DMD allowed to effectively decompose spatially coherent patterns and provided f and α estimates with high accuracy, within 0.6% error vs ground truth. The modes 1, 2, and 3 closely corresponded to the shapes of input data without overlapping with each other. However, mode 3 exhibited more contamination by the random noise compared to modes 1 or 2. This was expected, as the amplitude of mode 3 brightness exceeded that of random noise for only 3 out of 14 sampling points. In contrast, SVD was not able to separate modes 2 and 3 ("bubble modes"), and, as seen in Fig. 2.3(c), they overlapped. The singular value of mode 1 ("tissue mode") was an order of magnitude higher than those of modes 2 and 3, which is consistent with the input dataset where mode 1 had the highest initial amplitude and the lowest α. Fig. 2.3(d) shows the result of applying

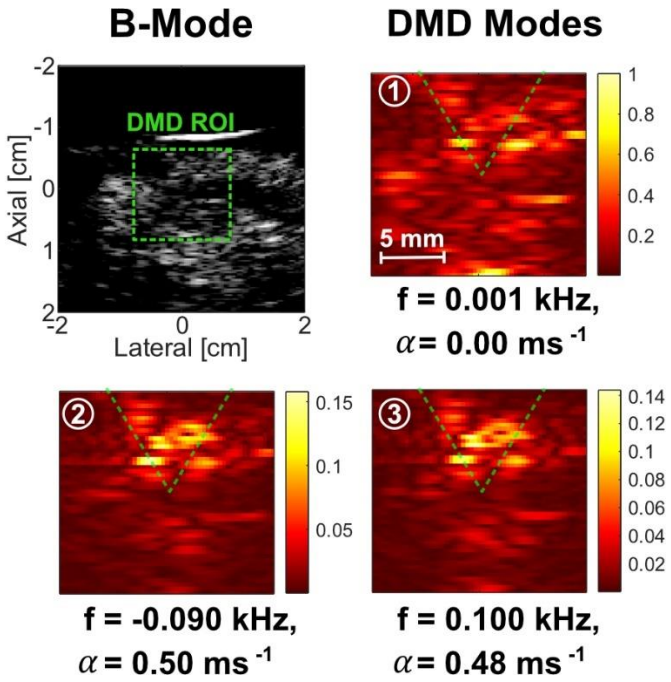

Figure 2.4. DMD modes of bubble Doppler obtained from pHIFU exposure of ex vivo tissue without cavitation. The green box on the B-mode image highlights the region of interest for bubble Doppler. Frequencies and decay rates are presented at the bottom of the corresponding mode images. The color bar scale was normalized to the maximum amplitude value over all DMD modes. HIFU was delivered from top of the images to the target point indicated by V-shaped green dashed line.

IIR high pass filter to the data, meant to eliminate mode 1, leaving only modes 2 and 3, and the result of subtraction of the filtered data from the input data, meant to reconstruct mode 1. Because the appropriate cut-off frequency to filter out mode 1 was known a priori, the separation of the "bubble modes" from "tissue mode" was successful, and the images of the modes had minimal overlap.

2.3.2 *DMD of Doppler Data for ex vivo pHIFU Exposures without Cavitation*

During the first set of pHIFU exposures in ex vivo bovine tongue tissue, the pHIFU amplitude was set to be below the cavitation threshold, as confirmed by PCD. A representative example of DMD modes corresponding to such a HIFU pulse, with corresponding f and α are shown in Fig. 2.4. The DMD-processed region of interest (ROI) is shown within the larger B-mode image, and

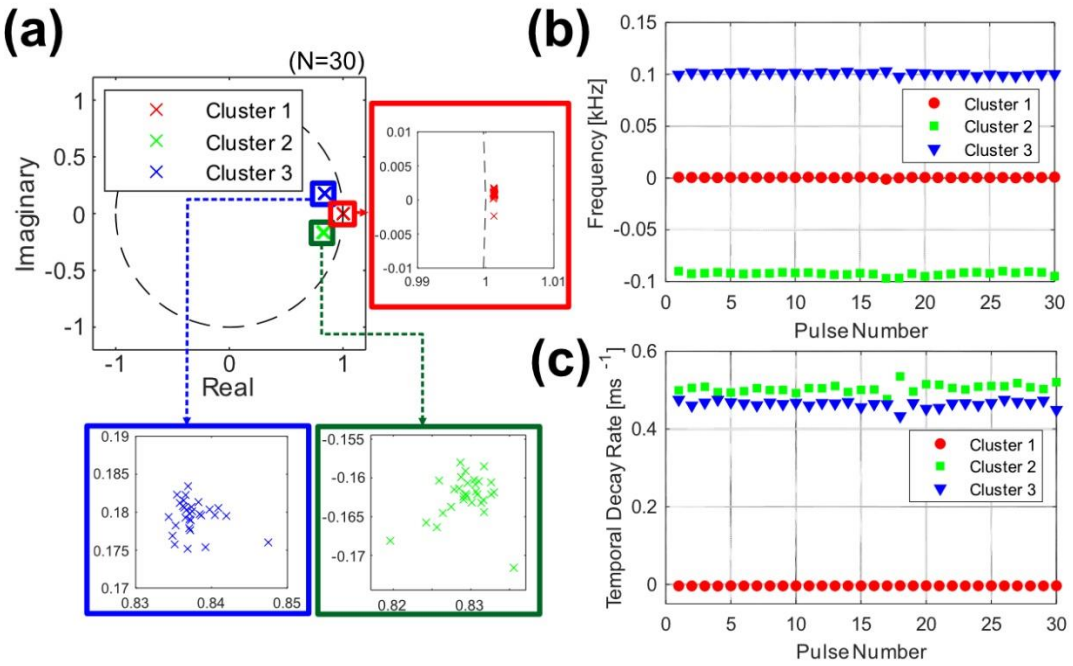

Figure 2.5. DMD eigenvalues during the 30-pulse pHIFU exposure without cavitation. (a) The discrete time eigenvalues for all 30 pHIFU pulses on the complex plane and the results of their k-means clustering. Three eigenvalue clusters were identified and marked with different colors. The (b) frequency and (c) temporal decay rate of the three clusters plotted vs HIFU pulse number.

the pHIFU beam location is denoted by a green dashed V-shape line on each DMD mode image. All DMD modes were normalized to the maximum amplitude across all identified modes and were displayed with adjusted range of color bar for better visualization. Three DMD modes were identified, all with frequencies below 0.1 kHz. The first mode showed nearly stationary tissue speckles with the highest amplitude. The second and third modes, characterized by significantly lower amplitude levels (~15% of the first), showed a paired behavior. The mode images, temporal decay rates, amplitude levels, and absolute values of frequency were very similar, and the only difference was the opposite sign of the frequency, indicating the opposite directions of axial motion of the two modes. The Doppler velocity corresponding to the last two modes, calculated from Ep. (2.13), was 1.4 - 1.5 cm/s. These values align with the expectations based on ARF-induced elastic rebound of tissue, as shown in our previous study [68].

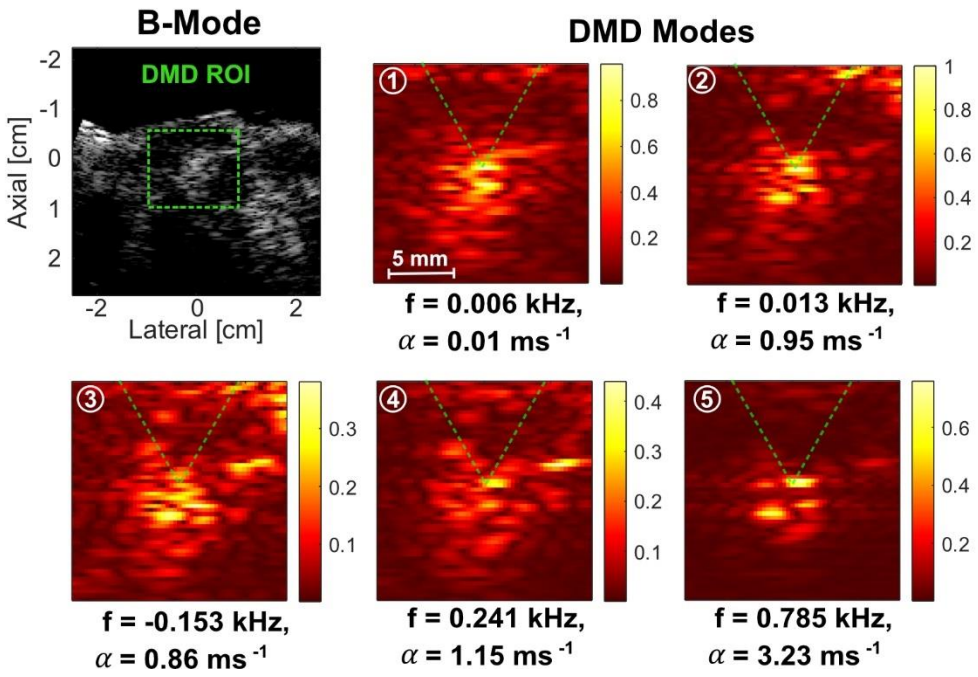

Figure 2.6. DMD modes of Bubble Doppler obtained from pHIFU exposure of ex vivo tissue with cavitation. The green box on the B-mode image highlights the region of interest for bubble Doppler. Five DMD modes were identified, and the corresponding images are presented with frequencies and decay rates. The color bar scale was normalized to the maximum amplitude value over all DMD modes. HIFU was delivered from the top of the images to the target point indicated by V-shaped green dashed line.

The k-means clustering results for discrete-time eigenvalues ($\mathbf{\Lambda}$) over 30 HIFU pulses on the complex plane are shown in Fig. 2.5(a). Each eigenvalue was denoted by a colored cross, and each identified cluster was assigned a different color. Three clusters were identified, each of which showed tight clustering with maximum eigenvalue distances of 0.041, 0.016, and 0.014, respectively. Fig. 2.5(b) and (c) show the values of f and α over 30 HIFU pulses; as seen, those values remained nearly constant, as expected for pHIFU exposures below the cavitation threshold.

2.3.3 *DMD of Doppler Data for ex vivo pHIFU Exposures Inducing Cavitation*

A representative example of DMD modes corresponding to a HIFU pulse that induced cavitation in the *ex vivo* tissue is shown in Fig. 2.6, in the same format as Fig. 2.4. DMD processing

consistently yielded five modes for those pHIFU exposures that represented the dynamics of tissue and residual bubbles immediately following each pulse. The first DMD mode displayed speckles over the entire ROI, with brighter hyperechoic regions at the focus. This mode had the lowest frequency (0.006 kHz) and temporal decay rate (0.01 ms^{-1}), indicating stationary backscatter from tissue and persistent residual bubbles that did not change within the imaging time window. The second mode was similar to the first mode in speckle distribution but had a higher temporal decay rate. The third and fourth modes depicted the speckles around the focus, with higher frequencies and temporal decay rates than the first two modes and lower amplitude level (<40% of the second). The Doppler speeds corresponding to those two modes were 2.4 and 3.7 cm/s with opposite directions, likely linked with ARF-displaced tissue motion similarly to second and third modes in Fig. 2.4. The fifth mode showed a backscatter pattern highly localized to the focal region, and the corresponding frequency, temporal decay rate, and Doppler speed were the highest among all modes (0.785 kHz, 3.23 ms^{-1}, and 12.1 cm/s). This mode was thus hypothesized to be associated with quickly dissolving cavitation bubbles. Indeed, previous studies have shown that most cavitation bubbles in pHIFU exposures dissolved within 1-2 ms following the pulse, which is consistent with α of this mode. The amplitude ratio between the first and fifth mode was initially -2 dB but reached -30 dB after 1 ms. Further, many cavitation bubbles with different radius and dissolution rate are expected to be present within the resolution cell of planewave image. Bubbles dissolving at different rates may be interpreted by DMD as rapidly changing backscattered signal.

The evolution of the DMD eigenvalues and modes over the 60 pHIFU pulses delivered to the same location of the tissue sample is presented in Fig. 2.7. The results of clustering the discrete time eigenvalues over pHIFU pulses on the complex plane are shown in Fig. 2.7(a) in the same format as Fig. 2.5(a). Five clusters were identified corresponding to the five DMD modes in Fig.

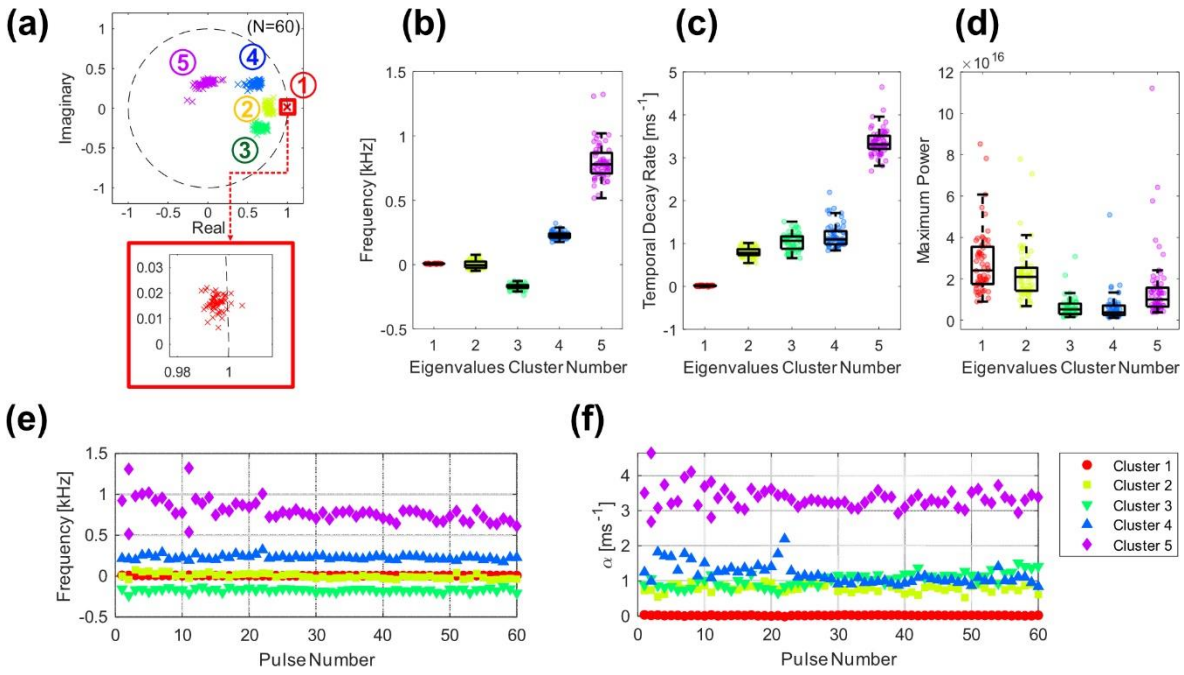

Figure 2.7. DMD eigenvalues during the pHIFU exposure with cavitation. (a) The discrete time eigenvalues over 60 pHIFU pulses on the complex plane and the results of their k-means clustering. Five eigenvalue clusters were marked as different colors and numbers. The box plot for (b) frequency, (c) temporal decay rate, and (d) maximum power of each eigenvalue cluster over all pulses; error bars represent minimum and maximum data points within 1.5 times the interquartile range (IQR), defined as the distance between the 0.25 and 0.75 quantile (also termed whisker). The (e) frequency and (f) temporal decay rate plotted vs HIFU pulse number.

2.6 and labeled with different colors. In particular, cluster 5 corresponding to mode 5, likely to be representative of cavitation, was assigned purple color. The eigenvalues for cluster 5 were clustered more loosely compared to the others; the maximum distances of eigenvalues in each cluster were 0.017, 0.221, 0.198, 0.419, and 0.521, respectively.

Fig. 2.7(b), (c), and (d) show the box plots for the values of frequency, temporal decay rate, and maximum power for each eigenvalue cluster, for the 60 HIFU pulses. Clusters 1 and 2 showed closely distributed f and α, while the maximum power distribution was broad. This reflects the fact that the hyperechoic region at the focus attributed to the persistent residual bubbles increased in brightness over the course of the exposure. On the other hand, cluster 5 exhibited a broad range

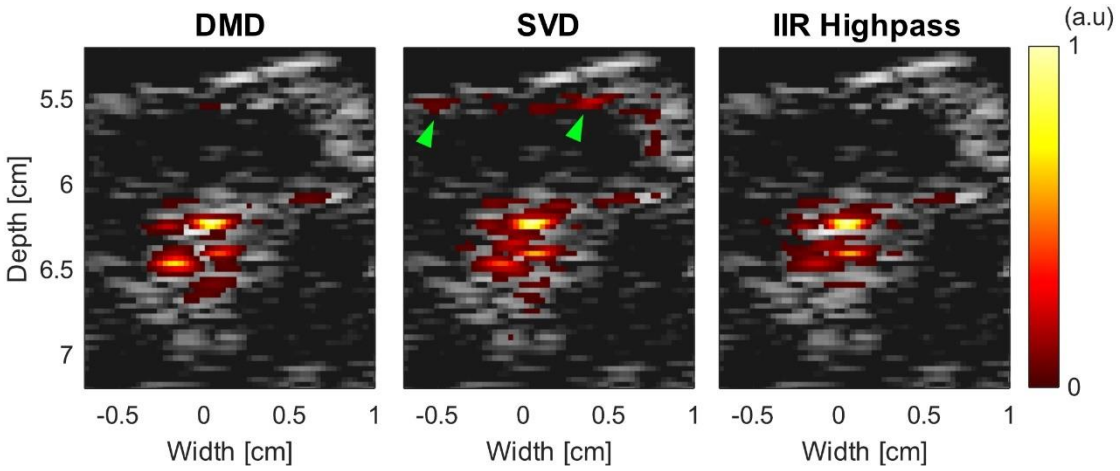

Figure 2.8. Comparison between Doppler power maps reconstructed using only bubble mode from DMD (Fig. 2.6) and, SVD and IIR highpass filtering. Note the Doppler power associated with ARF-induced tissue motion present after SVD filtering (green triangles).

of f from 0.520 kHz to 1.320 kHz and high α with a median of 3.3 ms^{-1}, supporting the hypothesis that it represented the rapidly dissolving residual cavitation bubbles. Additionally, clusters 3 and 4 showed tighter distribution ranges in f and α than cluster 5 and were characterized by the smallest maximum power values.

Fig. 2.7(e) and (f) show the evolution of f and α over the 60 HIFU pulses. The frequency for clusters 1 to 4 and temporal decay rate for clusters 1 to 3 were almost constant, similarly to clusters 1-3 in the exposure without cavitation (Fig. 2.5(b) and (c)). Conversely, in cluster 5, the frequency gradually decreased from around 1 kHz to 0.6 kHz as the treatment progressed. The temporal decay rate in clusters 4 and 5 decreased slightly (*i.e.* became less decaying), from around 2 to 1.5 ms^{-1} and 4 to 3 ms^{-1}, respectively, and became less variable after about 20th pulse. Taken together, those changes suggest that the distribution of bubble sizes, positions and decay rates became more consistent in the second half of pHIFU exposure, which could indicate consolidation of the bubbles in the same disrupted areas of tissue and not inflicting more damage.

The envisioned use of DMD processing during pHIFU exposures is described below. After selection of the bubble modes, the bubble map for each HIFU pulse can be reconstructed using

(12). Note that in this study only cluster 5 corresponded to the bubble mode, but in the case of multiple clusters being associated with bubble mode, a sum of the corresponding maps would be used. Following the reconstruction, conventional autocorrelation can be performed to obtain Doppler power map, which would then be thresholded and superimposed onto the B-mode image in real time. Fig. 2.8 shows an example of such an image, with DMD-filtered Doppler power map alongside the SVD and IIR highpass-filtered maps, superimposed onto B-mode. The dataset for this comparison corresponded to the data from a single HIFU pulse used in Fig. 2.6. In SVD filtering, the first SVD mode was eliminated based on the assumption that the predominant mode originated from stationary tissue. In IIR highpass filtering, the cutoff frequency was set to 100 Hz, and a third order filter was used. Notably, Doppler power map from SVD filtering retains clutter signals from ARF-based tissue motion (green triangles), whereas IIR highpass and DMD-filtered maps are comparable.

2.4 Discussion and Conclusion

This study investigated the utility of DMD technique in imaging transient cavitation bubbles during pHIFU therapy. The effectiveness of DMD to identify spatially coherent patterns and quantify their temporal dynamics was first demonstrated in a numerically simulated image dataset and compared to the performance of SVD and IIR wall filtering. Then DMD was applied to planewave Doppler datasets acquired during pHIFU exposures of ex vivo tissue.

In the simulation study DMD outperformed the SVD and IIR filter in terms of quality of pattern decomposition (Fig. 2.3(c)-(e)) and accuracy of the temporal dynamics metrics associated with them (Table 2.1)–frequency (f) and temporal decay rate (α). The values of f and α obtained through DMD were remarkably accurate for all modes (within 0.6% error), despite the simulation's input data containing two limitations that are inherent in the experimental implementation. First,

the total duration of Doppler ensemble in slow time (*i.e.* 4.7 ms for 14 sampling points with a 3 kHz PRF) was insufficient to encompass even a single cycle of 50 Hz, which was designated as the frequency for the square shape. Second, the SNR for the two circles were intentionally reduced to levels below random noise after 6 and 3 sampling points, respectively, as shown in Fig. 2.3(b). Those advantages of DMD also translated to the experimental dataset. In pHIFU exposures of *ex vivo* tissue, DMD filtering allowed to identify and display as Doppler power map the area of cavitation that was better localized and less cluttered compared to the SVD-filtered map (Fig. 2.8). IIR highpass filtering yielded a similarly shaped cavitation map to DMD in this case, but could not provide the associated temporal dynamics metrics (Fig. 2.8).

Additionally, DMD modes and their f (or corresponding Doppler speed) and α were found to be physically interpretable and consistent with prior studies. In pHIFU exposures without cavitation (Fig. 2.4), the three DMD modes could be identified as stationary tissue (first mode) and ARF-displaced axial tissue motion in both directions (second and third modes). This is because the tissue, immediately after the termination of HIFU pulse, is expected to move towards the HIFU transducer, and then to rebound away within the total acquisition duration (*i.e.* 4.7 ms), as seen prior study [68]. Similarly, each DMD mode in pHIFU exposures resulting in cavitation (Fig. 2.6) can be identified as stationary tissue (first and second modes), ARF-induced axial tissue motion in both directions (third and fourth modes), and transient bubbles (fifth mode). Comparison with the non-cavitation modes from Fig. 2.4 showed that the modes corresponding to the stationary tissue and ARF-induced tissue motion in Fig. 2.6 had a bright area at the focus, suggesting a contribution from residual bubbles. This may be attributed to the fact that some larger size, more stable bubbles moved together with tissue and potentially amplified the ARF displacement [68].

In the bubble mode, the temporal decay rate α can be interpreted as an average rate of bubble dissolution within a resolution cell of a planewave image. However, the physical interpretation of frequency f, or the corresponding Doppler speed, is not as straightforward, considering that residual bubbles are not expected to move or oscillate after the HIFU pulse. A possible explanation is that the speed of the surface of shrinking bubbles within the resolution cell is synchronized, leading to a phase shift in slow time. The DMD then interprets this as motion.

The traceability of tissue and bubble modes is another advantage of DMD. As seen in Fig. 2.7, the k-means clustering on complex planes allows one to track each DMD mode. This ability is particularly useful for quantitative imaging guidance in pHIFU therapy, as it allows for tracking of bubble characteristics, which could be physically interpretable in terms of inflicted tissue damage. For example, the decrease in frequency and temporal decay rate for cavitation bubble mode, observed in Fig. 2.7(e) and (f), could be interpreted as a sign of bubble coalescence and decrease in surrounding tissue stiffness.

In this study the utility of DMD was explored for a relatively narrow application – as a type of wall filter in Doppler-based detection, mapping and quantitation of cavitation bubbles induced by pHIFU. However, we anticipate this technique to be useful in a number of other time-resolved ultrasound imaging tasks, e.g. vascular imaging, characterization of flow patterns in large veins and arteries, and monitoring of tissue ablative interventions over time.

This study is not free of limitations that warrant further investigation. First, the clustering method meant to track the different modes over the course of pHIFU exposure did not include automatic identification of the cluster corresponding to the cavitation bubbles. To automate the labeling process, several algorithms could be considered, including the eigenvalue thresholding (using f and α), mode image-based metrics (*e.g.* contrast-to-noise ratio), or machine learning

techniques. Second, the appropriate r selection for rank-r truncation using SVD, described in step b) of DMD processing section, also affects the decomposition quality of DMD. As mentioned in the methods, a preliminary empirical investigation was performed to identify the most effective truncation method for fast-dissolving bubbles. Such an investigation may need to be repeated if there are changes in acquisition parameters, such as the number of imaging pulses (m) used and Doppler PRF. The r selection problem in SVD is well known and previously reported in works on Doppler clutter filtering [52], [53]. Most importantly, current study only involved pHIFU exposures of stationary *ex vivo* tissue, devoid of circulation or physiological motion. On the one hand, application in the *in vivo* environment will undoubtedly complicate the analysis and increase the number of modes; on the other hand, the advantages of DMD are expected to stand out more. This will be explored in future studies.

Chapter 3.

DYNAMIC MODE DECOMPOSITION BASED DOPPLER MONITORING OF *DE NOVO* CAVITATION INDUCED BY PULSED HIFU *IN VIVO*[2]

3.1 INTRODUCTION

Pulsed high intensity focused ultrasound (pHIFU) therapy has emerged as a promising non-invasive treatment modality, holding significant potential in various clinical applications. These include enhancing drug delivery into tumors by increasing permeability for passive diffusion [9], [10], [11] and modulating the microenvironment of both malignant and non-malignant tissue, thereby resulting in therapeutic outcomes [12], [13], [14], [15]. This pHIFU modality employs relatively short ultrasound pulses, ranging from 1 to 100 milliseconds at frequencies near 1 MHz and at a duty cycle under 5%, to induce *de novo* inertial cavitation in tissue without administration of exogenous contrast agents [9], [10], [11], [12], [13], [14], [15], [48], [49]. This process allows to achieve mechanical disruption of the target area while minimizing thermal effects.

For the pHIFU targeting, ultrasound B-mode imaging, realized with an imaging probe that is incorporated coaxially in the center opening of the HIFU transducer, is currently the most widely used method. While B-mode imaging is quite effective at targeting and qualitative monitoring of cavitation, it faces challenges in quantitative assessment of cavitation and its correlation with tissue damage. This difficulty arises because the rapid dissolution of cavitation bubbles following each pHIFU pulse can degrade the consistency and sensitivity of the B-mode imaging quality [48], [50].

[2] Manuscript in preparation for submission.

Passive methods such as passive cavitation detection (PCD) and passive acoustic mapping (PAM), which are alternatives to the active pulse-echo techniques like B-mode, quantify the broadband noise from inertial cavitation collapse during each pHIFU pulse. Although these methods demonstrate sensitive detection of cavitation activity, they lack the capability to image cavitation with sufficient resolution [48]. Specifically, the axial resolution of PAM is limited by the angular aperture of the imaging probe, making it challenging to map cavitation accurately [40].

A variation of Doppler ultrasound imaging (also termed bubble Doppler) has been proposed for mapping pHIFU-induced cavitation bubbles [46], [51], [52]. This technique employs a series of planewave imaging pulses, emitted immediately following each HIFU pulse. Those imaging pulses interact with residual cavitation bubbles that rapidly dissolve within milliseconds. Doppler processing of the backscattered pulses interprets those changes as motion, and the resulting Doppler power map corresponds to the spatial distribution of bubbles. As in any Doppler processing, selecting the appropriate wall filter is crucial for isolation of bubbles from clutter motion of tissue and blood flow.

Traditional frequency-based Doppler wall filters, like the infinite impulse response (IIR) high pass filter, are designed to eliminate low-frequency tissue clutter motion in Doppler acquisition domain. However, the use of those filters in bubble Doppler is challenging because the rapid dissolution of bubbles places a limitation on the number of usable Doppler pulses in the ensemble, which causes initialization issues and degrades the filtering quality [52]. Similarly, singular value decomposition (SVD) filter, another common choice in vascular imaging [53], [54] and proposed for cavitation imaging [52], encounters the same challenges, greatly reducing decomposition performance. In addition, SVD decomposes a matrix of images into orthogonal modes, and the modes of interest can be selected based on their amplitude of singular values. However, in pHIFU

the amplitudes of SVD modes from tissue and from bubbles can be comparable, which reduces the efficiency of filtering.

Recently, we introduced dynamic mode decomposition (DMD) as an advanced Doppler clutter filtering technique [69]. DMD is a fast-growing data-driven approach to provide spatiotemporal decomposition of a dataset matrix with dimensionality reduction, where each mode is characterized by spatial coherence and same temporal behavior [55], [56], [57]. Unlike the SVD that provides spatial coherence in dataset images without considering their temporal relation, DMD provides not only spatial coherence but also temporal characteristics of the modes, like fast Fourier transform (FFT). We have evaluated the performance of DMD as a Doppler clutter filter during pHIFU exposures in silico and ex vivo to map the fast-dissolving bubbles and additionally capture temporal characteristics, most importantly their dissolution rate. This was achieved under linear approximation of the bubble's temporal behavior (i.e. harmonic motion with exponential growth or decay), which is a reasonable approximation of the Doppler signals backscattered from dissolving bubbles [46]. Each mode and its temporal decay rate, extracted by DMD, are trackable over pHIFU pulses and are physically interpretable as backscatter from stationary scatterers, tissue motion due to acoustic radiation force (ARF), and dissolving residual bubbles.

The goal of this work was to apply DMD to mapping inertial cavitation during pHIFU treatments of in vivo surgically exposed porcine liver, and to correlate bubble Doppler power maps to resulting areas of tissue damage. Porcine liver is a representative model of heterogeneous, highly vascularized tissue, containing vascular and biliary structures of different scales. Externalization was done for precise localization and characterization of the tissue damage by cavitation.

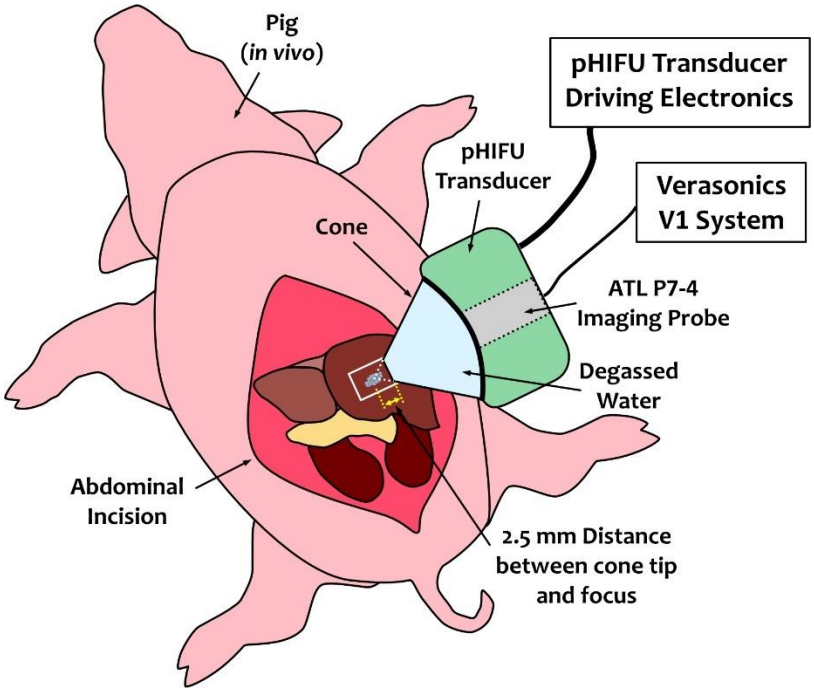

Figure 3.1. Schematics of the experimental setup for pHIFU exposure in a swine model in vivo. A HIFU transducer equipped with water-filled coupling cone on the front and a coaxial imaging probe mounted at the center opening were used to deliver pHIFU pulses and acquire imaging data, respectively. A midline abdominal incision was made, allowing the cone tip to be in direct contact with the liver surface.

3.2 METHODS

3.2.1 *Experimental Setup*

An illustration of the experimental setup associated with US-guided pHIFU exposure of the *in vivo* surgically exposed porcine liver is shown in Fig. 1. HIFU transducer used in this study was a 1.5 MHz, spherically focused 12-element sector array that had 8 cm aperture size, 6 cm nominal focal distance, and 2 cm circular central opening. The size of the focal region of this transducer in linear propagation regime at -6dB was 0.46 mm diameter by 3.8 mm length. A degassed water-filled coupling cone was attached to the front side of the HIFU transducer and sealed with acoustically transparent membrane. The distance from the membrane to the HIFU focus was 2.5 mm, and the diameter of the opening was 13 mm. The transducer was controlled by high power

driving electronics – a custom built 12-channel class D amplifier system [63], [64]. The ultrasound imaging probe was a 64-element ATL P7-4 probe coaxially installed at the center opening of the HIFU transducer, controlled by Verasonics V1 system.

The pHIFU exposures were conducted to target the liver of one female domestic swine (100 lbs), following the animal experiment protocols approved by the Institutional Animal Care and Use Committee at the University of Washington, Seattle, WA, USA. Under the care of a full-time veterinary staff, the pig was anesthetized with Telazol premedication and then maintained under anesthesia with isoflurane over the course of the treatment. As shown in Fig.1, the approximately 20 cm midline abdominal incision was made, and sterile degassed saline was poured into the abdominal cavity for acoustic contact. The HIFU transducer assembly was mounted to a flexible gooseneck holder, and before each exposure the tip of the coupling cone was brought into direct contact with the surface of the liver, with slight pressure, and the transducer position was locked. A total of 12 different target points in the liver were treated consecutively, with 60 HIFU pulses administered at each location. The pig's respiration rate was in the range of 2.3-3.4 seconds/breath with approximately 1-2 mm lateral displacement at the HIFU cone tip. After the treatment, the position of each target was marked on the liver surface at 5 mm distance by a brief contact with a cautery device and photographed for the gross examination of the treated tissue surface. After the exposures the animal was euthanized, and the targeted area of tissue, referred to as lesions from here on out, were collected *en bloc* and fixed in 10% neutral buffered formalin. Following fixation, the lesions were bisected and paraffin-embedded for histology. One 5-micron thick histological section was taken from either side of the bisected lesion and stained with hematoxylin and eosin (H&E).

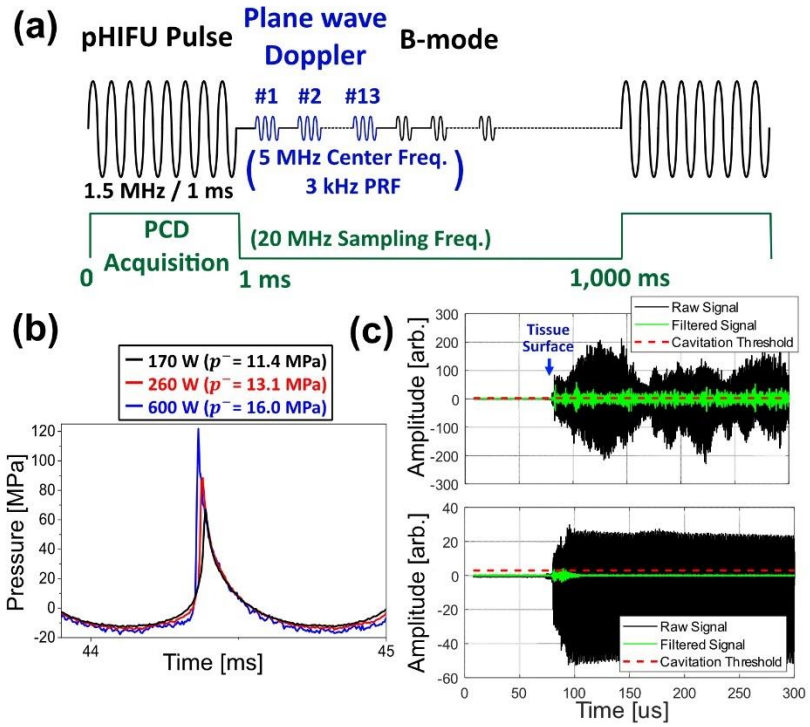

Figure 3.2. (a) Schematic of the ultrasound imaging sequence. 13 planewave Doppler pulses were emitted immediately after pHIFU pulse, followed by conventional ray-line B-mode imaging pulses. The imaging probe was operated in 'listening mode' for passive cavitation detection (PCD), capturing radio-frequency (RF) signals during HIFU pulses to monitor inertial cavitation activity. (b) The focal waveform for three different pHIFU output levels used in this study. (c) Two representative examples of PCD RF signal before (black) and after (green) filtering to isolate broadband emission signal for the pulses where cavitation was present (top) and absent (bottom).

3.2.2 *pHIFU Exposure Parameters and US Imaging Data Acquisition*

The pHIFU pulsing protocol used in this study was the same as that used in previous studies from our group [9], [46], [64]: 1 ms long pulse was delivered at 1 Hz pulse repetition frequency (PRF). As shown in Fig. 3.2(a), each HIFU pulse was immediately followed by 13 planewave Doppler pulses with a 3 kHz PRF and conventional 128 ray-lines B-mode imaging pulses. Each of these Doppler pulses had a center frequency of 5 MHz and a pulse length of 3 cycles. The spatial resolution of the planewave images at the focus, obtained from the full width half maximum of point-spread function from measurement, was 2.17 mm in lateral and 0.46 mm in axial.

Three different HIFU output levels were selected based on preliminary observations [69] to induce various levels of cavitation activity and thus degrees of tissue damage. The focal waveforms corresponding to those output levels were measured in water using a fiber-optic probe hydrophone (FOPH 2000, RP Acoustics, Leutenbach, Germany) and are shown in Fig. 3.2(b). Among the 12 locations treated, three were subjected to the lowest HIFU output level (acoustic power of 170 W, peak positive/negative pressure levels of 67.0/-11.4 MPa), that was expected to be just below the cavitation threshold. Five locations were treated at the intermediate output level (260 W and 87.0/-13.1 MPa), expected to induce low to medium cavitation activity and moderate tissue damage. The other four locations underwent treatment at the highest output level (600 W, 120.2/-16.0 MPa) to generate more severe mechanical tissue damage.

While each HIFU pulse was being delivered, all elements of the imaging probe passively captured the broadband emissions from inertial cavitation collapses at a sampling frequency of 20 MHz, commonly referred to as passive cavitation detection (PCD). PCD processing consisted of the following steps. First, delay-and-sum beamforming was applied to the radio-frequency (RF) signals captured by the imaging probe to align their phases at the HIFU focal point. Subsequently, the beamformed RF signal underwent a two-step filtering process to eliminate the backscattered HIFU harmonics. First, a bandpass filter with a cut-off frequency range of 2.5-7.5 MHz was applied. Then, a comb notch filter with a 500 Hz stopband at HIFU harmonics was used. The resulting signal corresponded to broadband noise from inertial bubble collapses, and two PCD metrics were derived from it. The first was the noise level (NL), which reflects the temporal average of broadband noise amplitude:

$$NL = \frac{1}{N}\sum_{k=1}^{N}|x_k|, \tag{3.15}$$

where x represents the filtered RF signal, and N is the total number of sampling points in the signal. The other metric was the amplitude ratio (AR), indicating the ratio between the maximum absolute value of signal and the cavitation threshold, defined as maximum absolute value of background noise multiplied by $\sqrt{5}$, in accordance with Rose criterion [70]:

$$AR = \frac{max(|x|)}{\sqrt{5}\times max(|x_{noise}|)}, \tag{3.16}$$

where x_{noise} denotes the background noise of the filtered RF signal. Fig. 3.2(c) shows the two representative examples where substantial cavitation activity was observed throughout the HIFU pulse in the top figure, while in the bottom figure, cavitation was only transiently observed at the beginning of the pulse. The latter case was expected to produce negligible tissue damage.

3.2.3 *Planewave Doppler Processing Methods*

The signal processing described in this section was performed offline using MATLAB 2022a (v9.12) (MathWorks). The overall processing procedure is shown in Fig. 3. The processing was applied to the 2-dimensional in-phase quadrature (I/Q) modulated planewave image datasets acquired by Verasonics.

3.2.3.1 Dynamic Mode Decomposition

In our study, DMD was used for two purposes. The first was to isolate cavitation bubble images (or modes), akin to Doppler clutter filter. The other purpose was to obtain the temporal characteristics of the bubble modes in slow time – frequency and decay rate. To perform DMD, each of the 13 planewave I/Q images, acquired immediately after a HIFU pulse, was reshaped into column vectors, and then arranged into matrices $\boldsymbol{X}$ and $\boldsymbol{X'}$, each having 12 columns. These

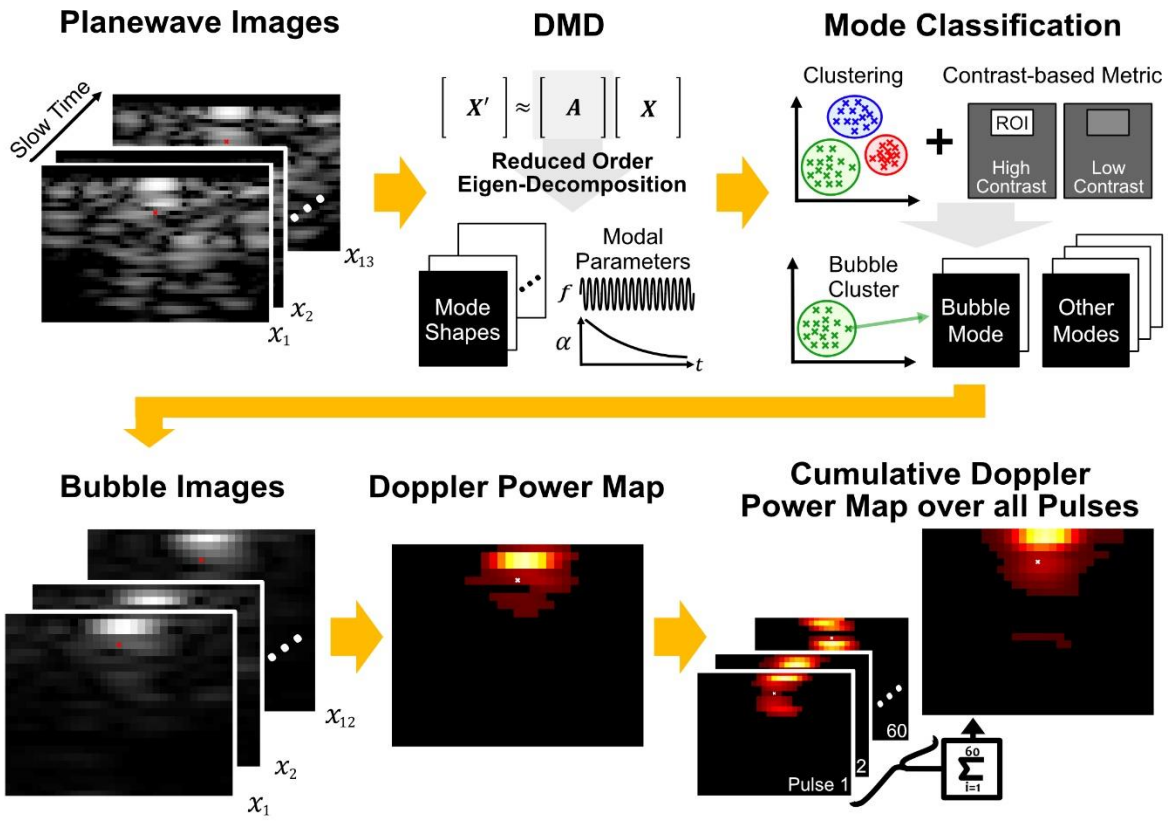

Figure 3.3. Schematic of the image processing method for generating a DMD-based cumulative Doppler power map. I/Q modulated planewave images underwent DMD processing, yielding a reduced order set of spatiotemporal modes along with modal parameters such as mode frequency and temporal decay rate. From these unclassified modes, bubble modes were identified using k-means clustering and a contrast-based thresholding method. These bubble modes were then reconstructed into bubble images, which were further processed using a conventional Doppler power algorithm, Finally, the Doppler power maps corresponding to each pHIFU pulse were cumulatively summed over all pHIFU pulses, enabling a comparison with histological images.

matrices corresponded to the 1st–12nd and 2nd–13rd planewave images, respectively. The number of rows (n) in these matrices was on the order of 10^3, corresponding to the total pixel count within the DMD processing window (≅1 cm square). In the linear approximation, the two matrices are related as:

$$\boldsymbol{X'} = \boldsymbol{AX}. \tag{3.17}$$

Here, $\boldsymbol{A}$ is an $n \times n$ matrix, and its direct calculation can be computationally expensive. Instead, DMD provides a rank-r approximation of eigenvectors ($\boldsymbol{\Phi}$) and eigenvalues ($\boldsymbol{\Lambda}$) of $\boldsymbol{A}$, expressed as

$$\boldsymbol{A} \cong \boldsymbol{\Phi}\boldsymbol{\Lambda}\boldsymbol{\Phi}^{-\mathbf{1}}, \tag{3.18}$$

where $\boldsymbol{\Phi}$ is an $n \times r$ matrix, each of columns is eigenvector of $\boldsymbol{A}$; $\boldsymbol{\Lambda}$ is an $r \times r$ diagonal matrix, each of diagonal elements is eigenvalue of $\boldsymbol{A}$; and the superscript $-\mathbf{1}$ indicates the inverse of the given matrix.

DMD processing aims to find $\boldsymbol{\Phi}$ and $\boldsymbol{\Lambda}$, and was described in detail in our previous study on pHIFU *ex vivo* [69] and other studies in fluid mechanics [55], [67], [71]. Thus, we provide an abbreviated description of the procedure here.

a) Calculate the truncated singular value decomposition (TSVD) of $\boldsymbol{X}$, with the truncation rank r determined such that the cumulative sum of the top r singular values exceeds 97% of the total sum of them [69]:

$$\boldsymbol{X} \cong \boldsymbol{U}_r\boldsymbol{\Sigma}_r\boldsymbol{V}_r^*, \tag{3.19}$$

where columns of $\boldsymbol{U}_r$ and $\boldsymbol{V}_r$ matrices are the left and right singular vectors truncated to rank r, $\boldsymbol{\Sigma}_r$ is a rank r diagonal matrix where each element is a singular value, and the asterisk denotes the conjugate transpose.

b) Compute the reduced order $r \times r$ matrix $\boldsymbol{A_r}$, which is a similarity transformation matrix of $\boldsymbol{A}$:

$$\boldsymbol{A_r} = \boldsymbol{U_r^*}\boldsymbol{A}\boldsymbol{U_r} = \boldsymbol{U_r^*}\boldsymbol{X'}\boldsymbol{V}_r\boldsymbol{\Sigma_r^{-1}}. \tag{3.20}$$

c) Find matrix $\boldsymbol{\Lambda}$ through the eigen-decomposition of $\boldsymbol{A_r}$:

$$\boldsymbol{A_r W = W \Lambda}, \tag{3.21}$$

where $\boldsymbol{W}$ is the eigenvector matrix of $\boldsymbol{A_r}$.

d) Calculate matrix $\boldsymbol{\Phi}$:

$$\boldsymbol{\Phi = X' V_r \Sigma_r^{-1} W}. \tag{3.22}$$

Each eigenvector (column vectors of $\boldsymbol{\Phi}$) is also referred to as mode shape. These can be transformed into 2D images, with the expectation that they correspond to physically interpretable modes such as bubbles, near-stationary tissue, ARF-induced motion, or blood vessels [69]. The discrete-time eigenvalues (diagonal elements of $\boldsymbol{\Lambda}$) provide information about how these corresponding DMD mode shapes evolve over slow time with regard to frequency and temporal decay rate.

3.2.3.2 Identification of Bubble Modes

As DMD provided unclassified sets of modes, it was necessary to identify the modes associated with bubbles based on their spatiotemporal characteristics. We hypothesized that, as a temporal characteristic, bubbles would be rapidly dissolving or undergoing size changes. Furthermore, as a spatial characteristic, these bubbles were expected to occur at the confined area around HIFU focus, in contrast to tissue or vasculature. In light of this hypothesis, we used a dual approach for automatic bubble mode identification: k-means clustering of eigenvalues to assess the temporal characteristics and the contrast-based metric thresholding of the DMD mode shapes to evaluate the contrast in the area where bubbles are expected.

In each pHIFU exposure, the discrete-time eigenvalues for all HIFU pulses were plotted on the complex plane. Here, the angle corresponding to a data point represents the frequency, and the distance from the origin indicates growth or decay rate. Subsequently, the eigenvalues were

grouped using k-means clustering, an unsupervised learning method that groups the dataset into 'k' clusters by minimizing the distance between each data point and the centroid of its corresponding cluster [69]. The number of input clusters was set as the average number of modes identified by DMD across the HIFU pulses. This process enabled the grouping of modes with similar temporal characteristics into the same cluster, under the assumption that the temporal behavior of the same modes (*e.g.* bubbles or tissue) had similar dynamics over the course of pHIFU exposure.

Within the set of clusters, the bubble clusters were identified using a peak-to-sidelobe ratio (PSR) thresholding method. PSR stands as a contrast-based metrics, similar to the contrast-to-noise ratio (CNR), designed to quantify the level of contrast within the region of interest (ROI) in comparison to the background. The distinction between PSR and CNR is PSR's utilization of the maximum value within the ROI, as opposed to the average value. PSR was defined as

$$\text{PSR} = \frac{max(S_{ROI}) - mean(S_{background})}{\sigma_{background}}, \tag{3.23}$$

where S_{ROI} and $S_{background}$ represent the mode shape image within ROI and all other regions, respectively, and $\sigma_{background}$ denotes the standard deviation of the brightness of the pixels in the background region. In this method, the size of ROI was set to be laterally 3.5 mm around HIFU focus and axially 2.5 mm, positioned just below the tissue surface, as bubbles were expected in that area. The clusters were identified as associated with bubbles when over 50% of modes within the same cluster exceeded the PSR threshold. Finally, the bubble images in slow time were generated for each HIFU pulse using only the modes that surpassed the PSR threshold within the identified bubble clusters:

$$\boldsymbol{x}_{k,bubble} = \boldsymbol{\Phi}_B \boldsymbol{\Lambda}_B^{k-1} \boldsymbol{b}_B, \tag{3.24}$$

where $\boldsymbol{x}_{k,bubble}$ represents kth bubble images in slow time, subscript B denotes bubble modes, and $\boldsymbol{b}$ is the initial mode amplitude vector corresponding to the first planewave image x_1 (i.e. $\boldsymbol{b} = \boldsymbol{\Phi}^{\dagger} x_1$, where † denotes pseudo inverse).

3.2.3.3 Cumulative Doppler Power Map

Following the generation of 12 bubble mode images in slow time, a conventional zero-lag autocorrelation was applied to them to obtain a Doppler power map. Note that this Doppler image corresponded to a single HIFU pulse. Subsequently, the cumulative Doppler power map was normalized by the spatially averaged power level of the lowest frequency mode shape among the DMD modes corresponding to the first HIFU pulse. This mode shape is representative of the brightness level from near-stationary tissue around the targeted area (*i.e.* lowest frequency mode), before the tissue damage occurs (*i.e.* first HIFU pulse). This normalization step was expected to account for natural variability in backscattered signal amplitude between pHIFU exposures. The final processing step involved summing the Doppler power maps over the 60 HIFU pulses. The resulting cumulative Doppler power map was directly compared to the distribution of tissue damage within the corresponding histological section.

3.2.4 *Histological Analysis of Tissue Damage*

To quantify the tissue damage induced by each of the pHIFU exposures, we first selected a representative H&E-stained histological section for each treatment lesion, specifically choosing the one that showed the most extensive damage. Subsequently, we conducted a manual outlining the damaged area within this selected histological section, as shown in Fig 4. Separate outlines were used for damage of different severity, graded in three levels [28], [72]. Grade 3 indicated gross tissue damage, with tissue structures broken down to the subcellular level, similar to the

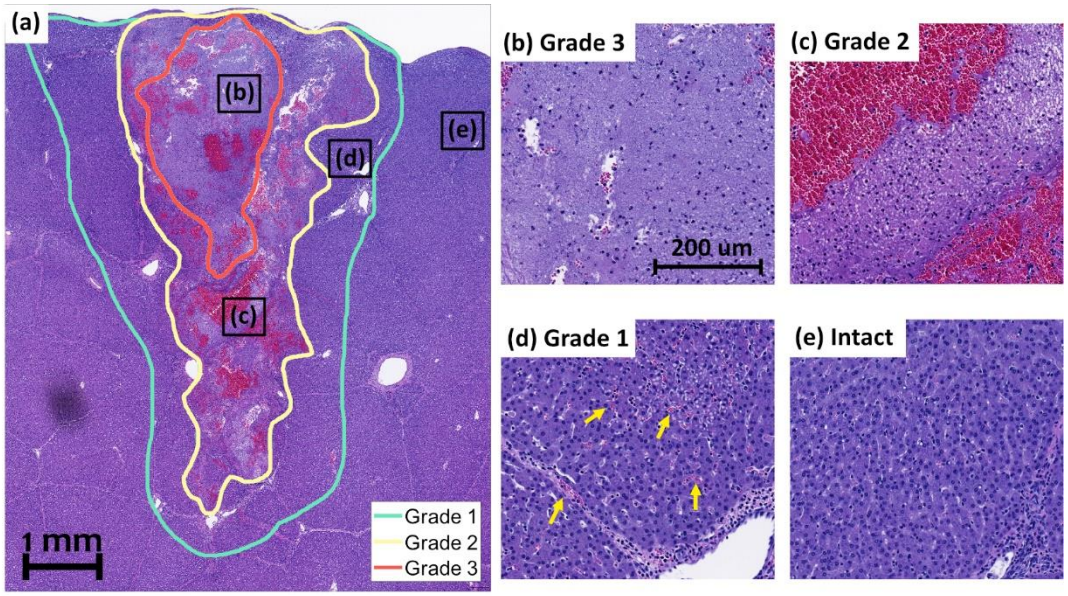

Figure 3.4. Representative example of the tissue damage grading method on an H&E stained tissue section. (a) A wide-view histological image of an area treated with 600 W pHIFU output pulses, where the tissue damage is categorized into three distinct grades. The zoom-in versions of each damage grades were presented: (b) grade 3, showing the most severe damage with the destruction in subcellular level, (c) grade 2, indicating moderate damage with visible hemorrhages, (d) grade 1, depicting minor damage with petechial hemorrhages marked as yellow arrows, and (e) an intact area, representing one without noticeable damage.

lesions induced by mechanical ablation techniques (*i.e.* histotripsy) [73]. This grade may also encompass hemorrhagic regions embedded within the completely fractionated damage area. Grade 2 was characterized by gross hemorrhage and distinct tissue disruption, with preservation of the overall tissue structure. This grade includes widely spread hepatic cords disruption. Grade 1 indicated the damage with evidence of petechial hemorrhage and localized hepatic cords disruption, marked with yellow arrows in Fig. 3.4(d), with tissue architecture comparable to undamaged tissue. Areas that did not fall into any of these grades were indicative of intact tissue with no visible damage.

3.2.5 *Comparison of Tissue Damage Maps with PCD and Cumulative Doppler Power Maps*

In order to compare the overall extent of tissue damage to the PCD metrics NL and AR for each pHIFU exposure, scaled damage area (SDA) was calculated for the graded histological maps as follows:

$$\mathrm{SDA} = \sum_{G=1}^{3} G \cdot A_G, \tag{3.25}$$

where G indicates the grade within the range of 1 to 3, and A_G represents the area assigned to each grade.

Comparison of the spatial distributions of tissue damage to the cumulative Doppler power maps in each pHIFU exposure was performed as follows. The cumulative Doppler power map was superimposed onto the graded histological image by aligning the position of the HIFU focus on both images. In the histological image, the distance from the focus location to the tissue surface was determined using raw RF signals from PCD. Specifically, we measured the distance corresponding to the time between arrival of the reflection from the tissue surface and the time of flight corresponding to the focus, as measured by FOPH. The lateral focus location was defined as the centroid of the area presenting the highest grade of tissue damage. Subsequently, the Doppler power levels falling within each of the three damage grade regions were averaged.

3.3 RESULTS

3.3.1 *Gross Observations and PCD Metrics for Different pHIFU Output Levels*

Representative photographs of the liver surface after pHIFU exposures at the three output levels are presented in Fig. 3.5(a). A bruise resulting from subsurface inertial cavitation was observed for all treatment points except those corresponding to the lowest HIFU output level (170

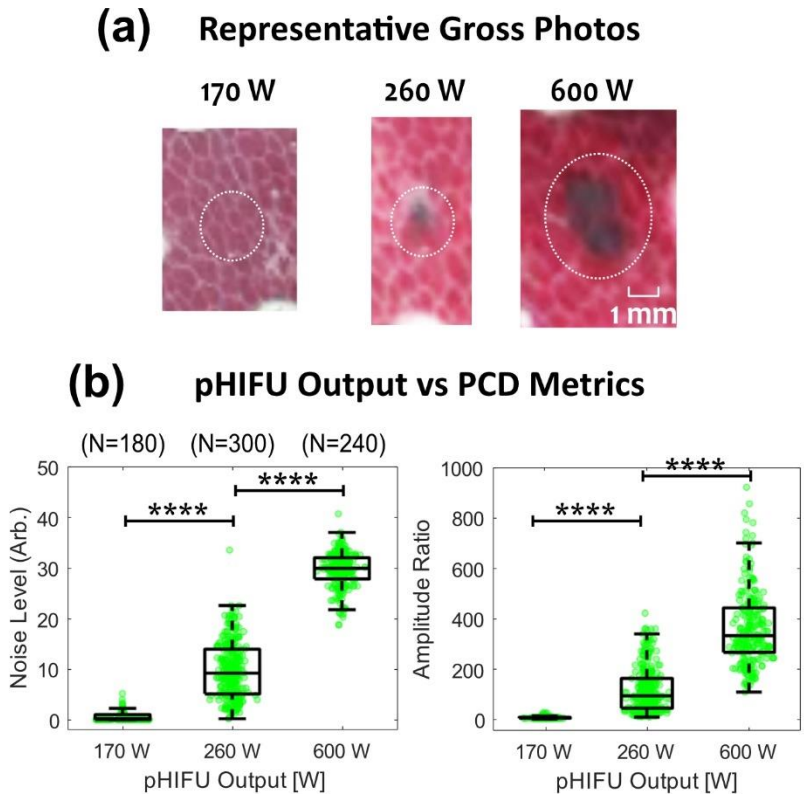

Figure 3.5. (a) Representative gross photos of lesions treated with varying pHIFU output levels. The treated areas on the tissue surface are marked in white dotted circles, and surface bruises are clearly visible for 260 and 600 W treatments (b) Box graphs presenting the relationship between passive cavitation detection (PCD) metrics–noise level (left) and amplitude ratio (right)–and the pHIFU output level. Each green circle indicates data point from a single pHIFU pulse. The box graphs display median values, upper and lower quantiles, and extremes. The two-sample t-test between datasets of subsequent output levels was performed and statistical significance is indicated by asterisks ($p < 0.0001$).

W), but the size of the bruise varied depending on the HIFU output level. The diameter of surface bruises was approximately 1.2 mm for 260 W and 3.5 mm for 600 W treatment areas.

In Fig. 3.5(b), the PCD metrics NL and AR corresponding to all HIFU pulses across all exposures are presented as box plots for each HIFU output level. As expected for sub-threshold output level, both NL and AR are near zero for the vast majority of pules at 170 W, which is in agreement with the absence of grossly visible damage at the tissue surface. As expected, the values of both NL and AR at the two higher output levels were not only progressively and statistically

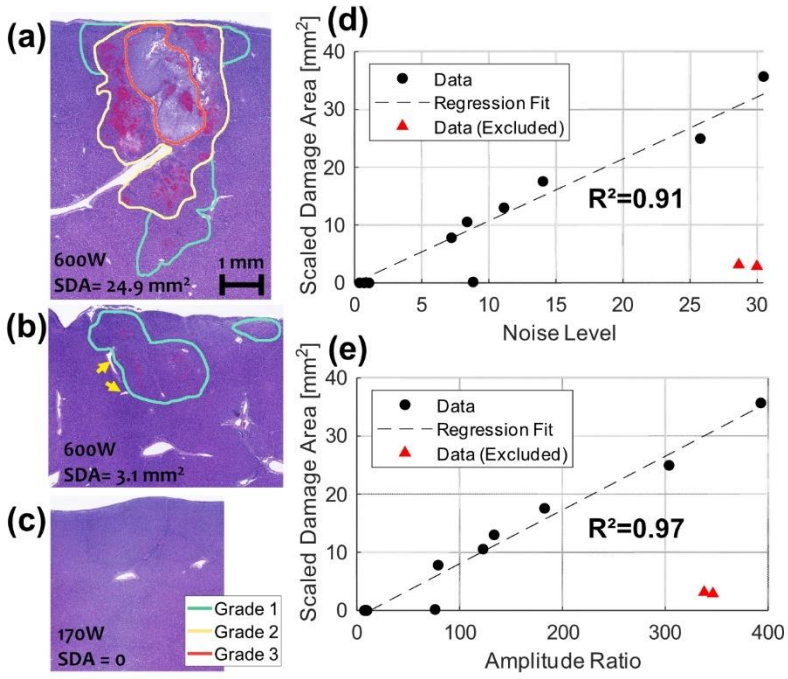

Figure 3.6. Representative results of tissue damage grading: (a) severe damage with 600 W pHIFU output, (b) an outlier case of minor damage with 600 W due to the presence of large scale vascular and biliary structures within the HIFU focal area (yellow arrows), and (c) no discernible damage with 170 W. The graphs on the right show the correlation between overall damage level from histological image, termed scaled damage area, and PCD metrics, (d) noise level and (e) amplitude ratio. Notably, anomalous cases like (b) are marked with red triangles and excluded from the regression fits.

significantly higher, but also varied from pulse to pulse and depending on location. These variations can be attributed to the structural differences within tissue between treatment points and the stochastic nature of cavitation nucleation, especially at the intermediate output level.

3.3.2 *Correlation of Overall Tissue Damage with PCD Metrics*

Fig. 3.6 (a)-(c) shows representative histological images of tissue damage induced by a pHIFU exposure. The highest pHIFU output (600 W) resulted in significant variability in tissue damage. Specifically, Fig. 3.6(a) illustrates a cohesive damaged area that includes the most severe grade (grade 3), while Fig. 3.6(b) shows only scattered areas of minor disruption in the superficial layer. Of the four locations treated at this power level, half showed the former type of severe damage,

and the other half – the latter. This variation in tissue damage could be attributed to the presence of large scale vascular and biliary structures within the HIFU focal area (yellow arrows in Fig. 3.6(b)), and preferential nucleation of cavitation within those structures [74]. Large scale (*e.g.* hundred microns) connective tissue structures are known to be less susceptible to cavitation damage even in histotripsy [75].

At a moderate pHIFU power of 260 W, the extent of tissue damage also varied: two out of five lesions included grade 3 damage, albeit smaller in size compared to those shown in Fig. 3.6(a); two lesions included grade 2 damage; and one lesion only minor damage akin to that in Fig. 3.6(b). At the lowest power setting of 170 W, no discernable damage was observed (Fig. 3.6(c)), consistent with PCD observations indicating little to no cavitation activity at that power.

Figs. 3.6(d) and (e) show a strong positive correlation between the PCD metrics (NL and AR) and SDA, with coefficients of determination (R^2) of 0.91 and 0.97, respectively. Notably, data points marked in red triangles, corresponding to minor tissue damage induced at the highest power setting as shown in Fig. 3.6(b), were excluded from this correlation analysis. This exclusion highlights a current limitation of PCD: its inability to spatially map cavitation occurrence and differentiate between cavitation within vasculature and tissue parenchyma.

3.3.3 *DMD Based Doppler Power Map and Comparison with Tissue Damage*

Figs. 3.7(a) - (e) shows the distribution of DMD eigenvalues on the complex plane for all pulses of five different pHIFU exposures to illustrate the process of bubble mode selection. The eigenvalues are denoted as colored crosses, with each color representing a separate cluster. DMD modes that exhibited high contrast within the ROI, surpassing the PSR threshold, are further highlighted with squares atop the crosses. The modes were designated bubble clusters when half of the points in the same cluster exceeded the PSR threshold, as described in the methods section.

Areas of the complex plane associated with bubble clusters were marked with gray background for clearer visualization.

The absence of bubble clusters was observed in lesions with no damage (Fig. 3.7(a)) and those with minor damage where cavitation activity within vasculature was expected (Fig. 3.7(e)). Clusters in these instances were more compact compared to cases where bubble clusters were present. The cluster distribution in Fig. 3.7(a) occupied the right side of the plane, which indicated low frequency of the modes. This is consistent with our prior observations in *ex vivo* tissue pHIFU exposures without cavitation, and corresponds to near-stationary tissue and its acoustic radiation force-induced motion [69]. Conversely, the bubble clusters in Fig. 3.7(b) - (d) predominantly occupied the left sector of the eigenvalue circle, indicative of higher mode frequency. They were also more spread out compared to the non-cavitation cases, likely due to the stochastic nature of the cavitation over pHIFU pulses and larger and more variable ARF-induced motion. An increase in the number of bubble modes, marked as squares in bubble clusters, was observed with the severe tissue damage level, reflecting an increase in the complexity of bubble modes behavior (*i.e.* increase in rank of the bubble mode).

A more detailed investigation of a specific exposure corresponding to Fig. 3.7 (d) is shown in Fig. 3.7(f) - (k). The DMD eigenvalues were grouped into 10 clusters, with three of them (clusters 8-10) designated as bubble clusters. Fig. 3.7(f) shows the representative mode shapes for each cluster, arranged in ascending order of their frequencies. Thes mode shapes are the most dominant patterns within their respective clusters. They are obtained through an additional SVD process, followed by the selection of the first SVD mode that corresponds to the largest singular value. Fig. 3.7(g) and (h) display the corresponding B-mode image, captured at the last (60^{th}) pHIFU pulse, and histological image with damage grading, respectively. The connective tissue structures,

observed in the histological image and identified in the B-mode and DMD images, are marked by the green triangles in Fig. 3.7(f), (g), and (h). In Fig. 3.7(f), clusters 1 and 2 display tissue speckles throughout the images, which are expected to represent stationary tissue, as indicated by their low frequency nature. Clusters 3 and 4 more prominently highlight connective tissue structures, as denoted by green triangles. Clusters 5 - 7 show hyperechoic areas with a slight central focus, with background tissue speckles, suggesting mixed modes resulting from residual bubbles and ARF-induced tissue motion. Clusters 8 - 10, designated as bubble clusters, were much more localized to within the ROI compared to other clusters.

Fig. 3.7(i) presents a cumulative Doppler power map using only bubble modes superimposed onto a B-mode image at the 60^{th} pHIFU pulse. The contour Doppler power map in Fig. 3.7(j) is superimposed onto the histological image. The overall shape of the power iso-levels corresponds quite closely to that of tissue damage area, whereas the width is slightly larger, and the length is substantially smaller. This may be attributed to the two opposite effects: tissue shrinking during the fixation process (both width and length) and the slight compression applied to the tissue by the coupling cone during pHIFU treatment (length). Because in this exposure vascular landmarks could be identified in both B-mode and histological images (green triangles in Figs. (g) and (h)), it was possible to compensate for the compression by aligning the Doppler map with these landmarks by axially stretching it. Fig. 3.7(k) represents such adjustment with 20% axial elongation, thereby providing a better agreement with the tissue damage region. Unfortunately, not all treated regions had the available landmarks for such alignment, and all the analyses presented below were based on Doppler power maps without compression compensation.

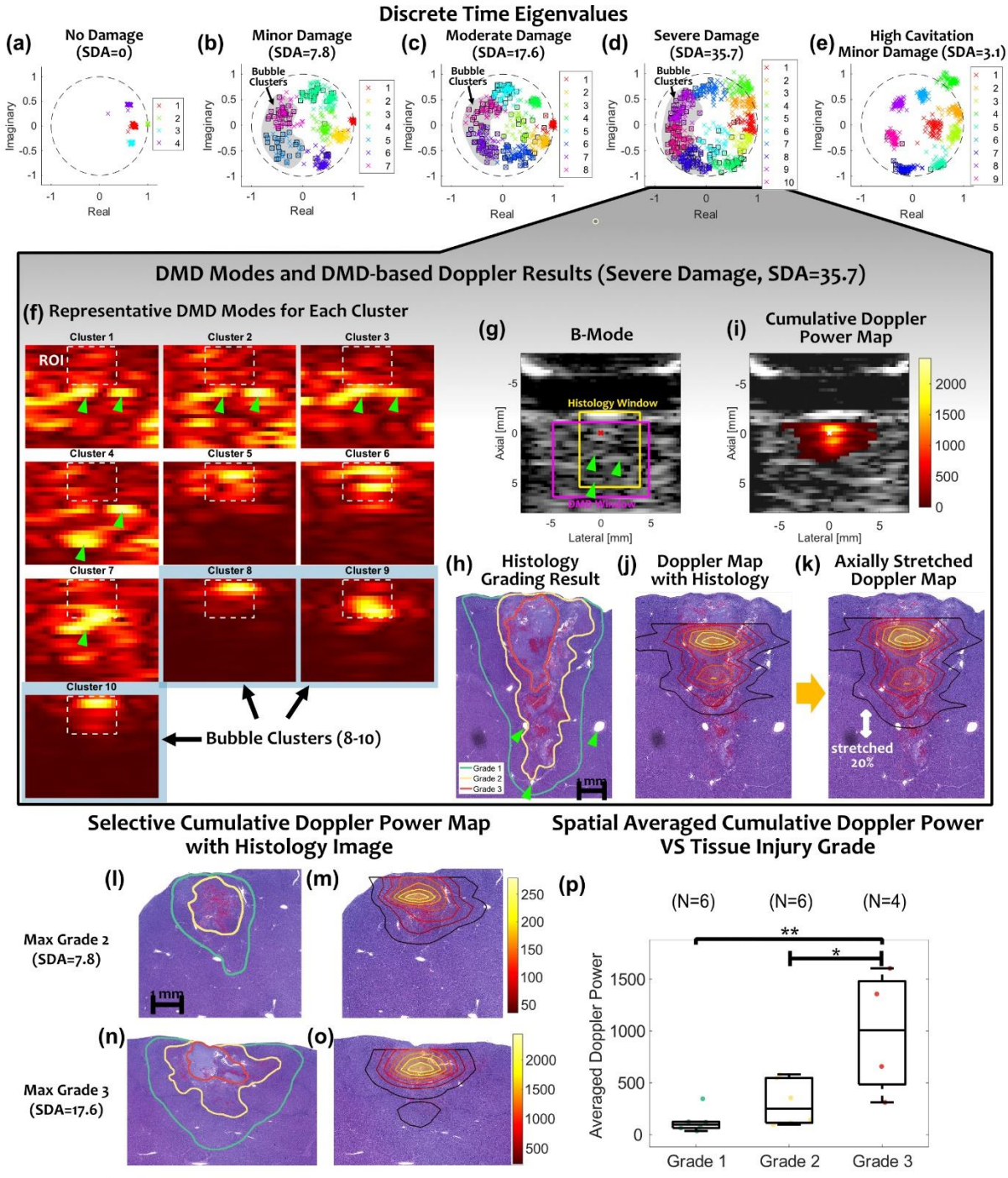

Figure 3.7. Representative results of bubble mode identification using discrete time eigenvalues on the complex plane: (a) no discernible damage at a pHIFU output level of 170 W, (b) low and (c) moderate damage at 260 W, (d) severe damage at 600 W, and (e) an anomalous case of minor damage at 600 W. Further investigations of DMD based Doppler power map for the severe damage lesion corresponding to (d) are shown below: (f) representative mode shapes in each cluster, (g) B-mode image, (h) histological image with damage grading (green arrows show vessels seen in B-modes as well), (i) a cumulative Doppler power map superimposed onto the

B-mode, (j) a contour map of cumulative Doppler power superimposed onto the histological image, and (k) stretched axially by 20% in the contour map to compensate for the pressure applied during the treatment. Other representative examples of cumulative Doppler power map and corresponding histological images of the damage with (l), (m) maximum grade 2, (n), (o) maximum grade 3. (p) A box plot showing the correlation between spatially averaged cumulative Doppler power level and damage grade, (*$p < 0.05$, ** $p < 0.001$)

Two other representative cases of cumulative Doppler power maps and corresponding histological grading for different tissue damage levels are presented in Fig. 3.7(l) - (o). Specifically, Figs. 3.7(l) and (m) represent a lesion with maximum damage level of grade 2, whereas Fig. 3.7(n) and (o) show a lesion with maximum damage level of grade 3. Overall, the shape of the iso-levels in Doppler power maps are qualitatively consistent with the damaged areas graded histologically. Fig. 3.7(p) shows the correlation between the damage severity and corresponding Doppler power levels, calculated by spatially averaging within each histologically graded damage region, as described in methods. This result suggests that more severe damage corresponds to areas of higher Doppler power level.

3.3.4 *DMD Mode Frequency and Decay Rate*

The DMD mode frequency and temporal decay rate over the course of pHIFU treatment were analyzed for eigenvalue clusters corresponding to a representative pHIFU treatment described in Fig. 3.7(d). The box plots for the mode frequency, temporal decay rate, and spatially averaged mode power levels for each eigenvalue cluster are presented in Fig. 3.8(a) through (c). The power of a mode is defined by $|\phi|^2$, where ϕ represents one column vector of mode shape matrix $\mathbf{\Phi}$. The bubble clusters are distinctively characterized by frequencies exceeding 0.7 kHz, marginally high temporal decay rates ranging between 0.5 to 2.5 ms^{-1}, and low average power levels compared to clusters corresponding to stationary tissue and connective tissue structures. Cluster 6 is an outlier, situated centrally in the eigenvalue circle in Fig. 3.7(d). The modes in this cluster likely

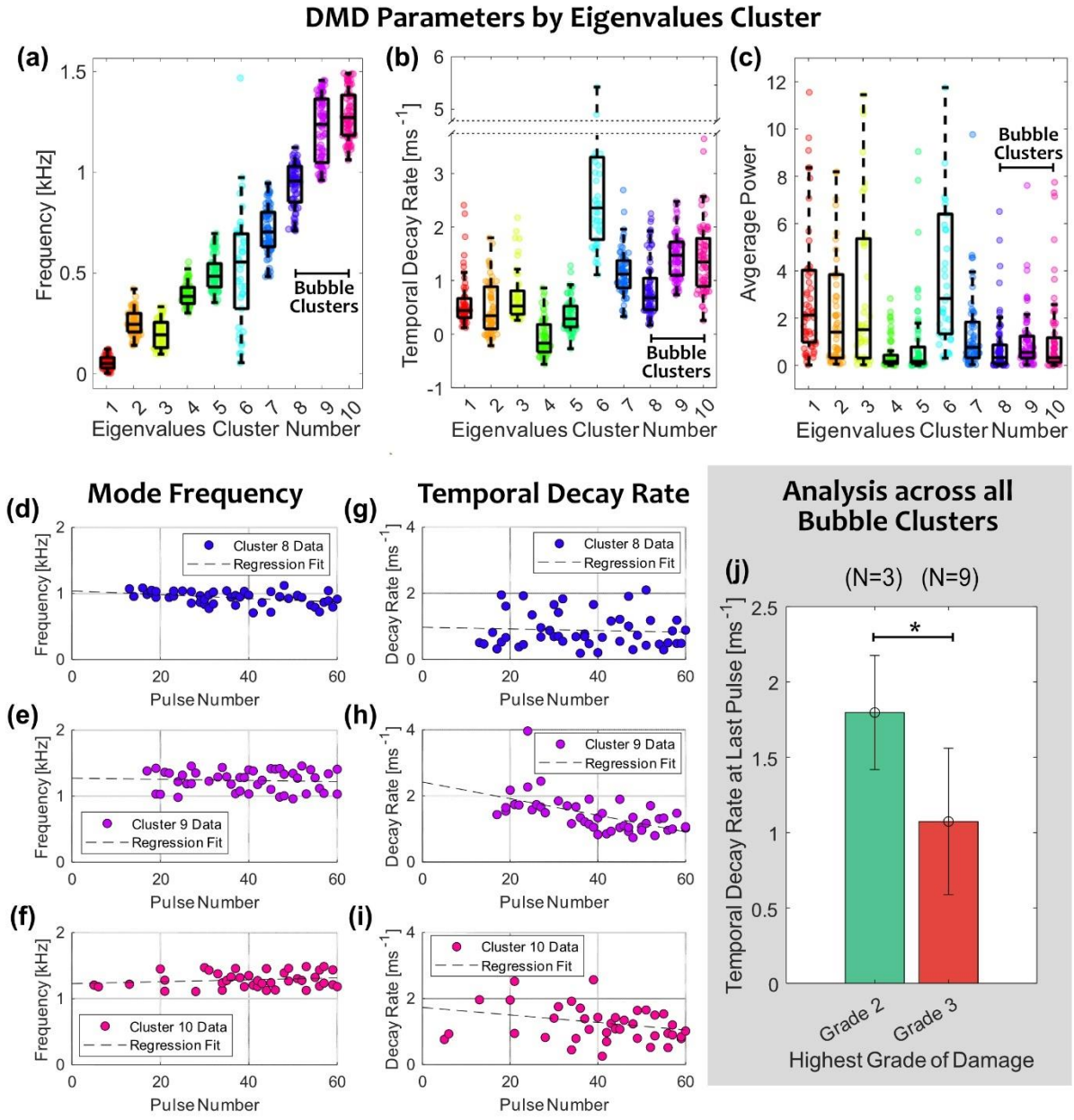

Figure 3.8. Evolution of DMD mode parameters over the course of pHIFU treatment that resulted in a lesion with grade 3 damage. The box graphs show (a) mode frequency, (b) temporal decay rate, and (c) average power of each DMD cluster for 60 HIFU pulses. Changes of (d)-(f) frequency and (g)-(i) temporal decay rate for bubble clusters (cluster 8-10) with respect to pHIFU pulse number. (j) Temporal decay rate at the last HIFU pulse, averaged across all bubble clusters from all HIFU exposures, for lesions with highest damage grades 2 and 3 (*$p < 0.05$)

represent noise due to motion out of the imaging plane caused by the respiration motion, leading to random fluctuations in pixels over slow time.

The progression of mode frequency for each bubble cluster (clusters 8-10) with respect to the pHIFU pulse number is shown in Fig. 3.8(d) to (f). Early in treatment before the 20th HIFU pulse, the identification of bubble modes across the clusters was inconsistent. Notably, the bubble mode in cluster 10, corresponding to the highest frequency, was initially detected at the 5th pHIFU pulse, whereas clusters 8 and 9 were discernible from the 13th and 17th pulses, respectively. Overall, the frequencies of all clusters remain within the same range over the course of treatment, with substantial variability and no overall trend. The frequencies of clusters 8 and 9 slightly decrease, and that of the cluster 10 increases over the course of treatment. This is consistent with the physical interpretation of frequency in the context of bubble modes [69]. The frequency likely reflects the velocity of the bubble wall, averaged over multiple bubbles of multiple sizes within a pixel, during their dissolution following each HIFU pulse. The average velocities can be estimated as 15-40 cm/s, which is consistent with the dissolution of approximately hundred-micron sized bubbles within 1-2 ms, as reported previously [46].

Fig. 3.8(g) through (i) show the changes in temporal decay rate of the bubble clusters over the course of treatment. In all three bubble clusters the temporal decay rates decrease over the course of treatment and become less variable, although the slopes of these trends differ among the clusters. These trends were observed across all pHIFU exposures, suggesting a gradual slowdown in the dissolution rate of residual bubbles as the treatment progressed, as well as merging of the bubbles.

The temporal decay rate at the last (60th) HIFU pulse collected across all exposures, averaged across all bubble clusters for each exposure, and grouped by maximum observed damage grade, is shown in Fig. 3.8(j). The results indicate that bubble modes from exposures with more severe damage had a lower temporal decay rate at the end of the treatment. This phenomenon could be

attributed to the presence of contiguous liquefied area in grade 3 tissue damage, which may provide greater stability to the bubbles, preventing their dissolution.

3.4 Discussion and Conclusion

In this study, DMD was applied to planewave Doppler-based imaging of residual bubbles during pHIFU treatment *in vivo*, and to evaluating bubble dissolution rate following each HIFU pulses. A fully automated bubble mode identification method was developed based on two assumptions: that residual bubbles dissolve rapidly, within milliseconds, and that the bubbles are localized to the HIFU focal regions. Accordingly, to identify bubble modes, a combination of k-means clustering of discrete time eigenvalues within the left half of the complex plane and PSR based thresholding of modes for localization to ROI were used. Subsequently, DMD filtered cumulative Doppler power maps were compared to the outlines of tissue damage on H&E-stained histological images. In addition, the evolution of the frequency and decay rate of bubble modes over the course of pHIFU treatments were investigated.

First, DMD demonstrated its ability to image the residual bubbles with high contrast while efficiently filtering out background tissue, vascular flow, and acoustic radiation force-based signals. Spatial distribution of cumulative Doppler power corresponded well, both qualitatively and quantitatively, to the distribution of cavitation-caused tissue damage and its severity evaluated from histological sectioning. Contrasting with the IIR highpass Doppler wall filter, which relies on the frequency characteristics of bubbles and tissue, DMD-based filter leverages additional parameters: the temporal decay rates and bubbles' spatial characteristics (*i.e.* their confinement to the HIFU focus), as well as their frequencies.

The comparison of DMD-filtered cumulative Doppler power maps with the extent of tissue damage from histological examination suggests a relationship between Doppler power levels and

the tissue damage severity. The correlation provides a candidate quantitative indicator – Doppler power within bubble modes – of tissue damage that could be displayed in real-time to inform treatment completion. Note that, although in this work the DMD filtering and bubble mode selection were performed in post-processing, these operations are rapid, taking 0.11 seconds per Doppler ensemble. Further, because the adequate regions for bubble cluster identification on the complex plane were confirmed in this work, it may be feasible to select bubble modes directly in real-time, without needing to cluster the entire set of eigenvalues from all pHIFU pulses.

Crucially, DMD offers a convenient analytical perspective on the residual bubbles, much like modal analysis does in structural dynamics, by providing DMD modal parameters (*e.g.* mode frequency and decay rate). Following the termination of a pHIFU pulse, the residual bubbles are expected to reduce in size, at variable rates, which will cause overall amplitude reduction and rapid phase change within each pixel. DMD can efficiently extract these changes as mode decay rates and frequencies, respectively. For instance, the descending trends in decay rate over pHIFU exposure, as shown in Figs. 3.8(g) – (i) can be interpreted as indicative of increased bubble stability, a consequence of tissue disruption providing more space. This information can be applied to evaluate tissue damage during treatment. The decay rate of 1.5 – 2 ms^{-1} for the current pHIFU pulse suggests an expected tissue damage level of grade 2, while a rate below 1.5 ms^{-1} indicates a grade 3 tissue damage level, as shown in Fig. 3.8(j). Furthermore, as shown in Fig. 3.7(p), cumulative Doppler power level can reinforce this evaluation. Although each individual parameter – decay rate or Doppler power level – displays large variance in correlation with tissue damage level, employing both parameters concurrently could enhance the reliability of the real-time damage level assessment.

This study is not without limitations. First, the current study was conducted on the liver tissue of only one pig; the number of damage regions was limited. Additionally, the pHIFU exposure was performed on a surgically exposed organ, and the Doppler images were devoid of noise from intervening tissues. Another challenge lies in the high complexity of planewave image datasets, which can contain multi-structural motions, potentially diminishing the decomposition quality of the DMD analysis. Due to the rapid dissolution of residual bubbles, the dataset size for DMD in slow time is necessarily limited; for instance, only 13 planewave images were utilized in this study, which consequently caps the maximum achievable decomposition rank. To mitigate this, the DMD processing window was carefully adjusted to the confined area around HIFU focus, as mentioned in methods. Further enhancements in decomposition quality could be achieved through the implementation of a high PRF acquisition scheme to increase the dataset [69] or by compensating for respiration motion [76]–a primary factor to the dataset's complexity. Furthermore, the accuracy of eigenvalue clustering could be refined by advancements in unsupervised clustering techniques, particularly those employing state-of-the-art machine learning algorithms.

Chapter 4.
QUANTITATIVE ASSESSMENT OF BOILING HISTOTRIPSY PROGRESSION BASED ON COLOR DOPPLER MEASUREMENTS[3]

4.1 INTRODUCTION

Boiling histotripsy (BH) is a non-invasive tissue liquefaction technique that uses sequences of millisecond-long high intensity focused ultrasound (HIFU) pulses with shock fronts [73]. High-amplitude shocks formed in the focal region of the HIFU beam due to nonlinear propagation effects play an essential role in BH method by enhancing the localized heating at the beam focus that results in reaching boiling temperature within milliseconds and formation of a mm-sized vapor cavity in tissue [21]. Interaction of the incident shocks with the vapor cavity enables tissue fractionation mechanisms such as atomization, micro-fountain [22], [23], and formation of prefocal cavitation cloud [25]. As a result of BH treatment, soft tissue at the focus is transformed into a liquid lesion filled with subcellular debris. Connective tissue structures, such as blood vessels, ducts, and organ capsule have been found to be more resistant to BH ablation than cellular tissue, thus providing an additional margin of safety [77]. Sharp borders and negligible thermal effects are characteristics for BH lesions. Due to these beneficial attributes BH is being developed for a wide range of clinical applications [4] such as liver, pancreas, and kidney tumor ablation [26],

[3] *© 2022 IEEE. Reprinted, with permission, from Minho Song et al. "Quantitative Assessment of Boiling Histotripsy Progression Based on Color Doppler Measurements", IEEE Transactions on. Ultrasonics, Ferroelectrics, and Frequency Control, Vol. 69, No. 12 (2022).*

[30], liquefaction of large hematomas for fine-needle aspiration [33], and potentiating anti-tumor immune response [30], [36].

To date, BH ablation has primarily utilized ultrasound imaging and sensing for real-time treatment planning, guidance, and evaluation of treatment outcomes, although MRI imaging has been explored as well [78], [79]. Coaxial B-mode imaging offers excellent qualitative guidance in real-time [26], [73] due to the fact that mm-sized vapor bubbles and μm-sized cavitation bubbles mediating the treatment appear as hyperechoic regions [80], [81]. Conversely, as tissue loses structure in the course of the treatment, the lesion progressively becomes hypoechoic. In addition, B-mode imaging provides a practical way to determine the HIFU output level necessary for inducing boiling through detecting the formation of the hyperechoic region when BH pulse amplitude is gradually increased. Various ultrasound sensing methods have also been used to detect boiling and cavitation bubble activity in BH sonication. In particular, fluctuation of the input voltage on a single-element HIFU transducer was used to determine the initiation of boiling [21], [73], [78]. Passive cavitation detection (PCD) prevalently used in many other cavitation-based ultrasound therapies gives another option for treatment planning and monitoring [21], [24].

Although coaxial B-mode ultrasound provides a means for BH planning, targeting, and real-time feedback on treatment progression, the information on treatment completeness is only qualitative. Having a quantitative metric of the degree of tissue fractionation obtained in real time during the treatment is important because tissues have inherently variable sensitivities to BH fractionation, depending on their mechanical properties, structure, and composition [4]. As a result, different tissue types, even within the same targeted volume, require different treatment duration (or number of BH pulses of certain frequency, duration and shock amplitude delivered per focus location) for complete fractionation [26]. For example, in volumetric BH treatments of *in vivo*

porcine kidney, the number of pulses required for full liquefaction were largest for collecting system, smaller for medulla, and smaller yet for cortex [26]. The use of the same BH treatment duration in all targets could lead to overtreatment and excessively long treatment time or undertreatment. Thus, a real-time ultrasound-based strategy that would provide spatially resolved, quantitative information on the degree of tissue liquefaction is needed.

Although a quantitative liquefaction metric for BH is yet to be developed, several candidate metrics and methods have been investigated for other histotripsy regimes – shock-scattering histotripsy and microtripsy [82]. These histotripsy techniques use shorter pulses than BH (microseconds rather than milliseconds) and higher *in situ* pressure levels to engage different cavitation regimes and arrive at mechanical tissue ablation. In early studies, B-mode ultrasound backscatter signal intensity from liquefied lesions was quantified over the course of shock-scattering histotripsy treatment and correlated to the degree of tissue liquefaction [83]. This metric decayed exponentially with treatment time because subcellular debris and liquefied tissue are less scattering than intact tissue [84]. However, the trend became less obvious towards the end of the treatment, when the tissue within the lesion became almost fully liquefied, making it difficult to determine treatment completion. In another method, Young's modulus of the treated tissue was measured using shear wave elastography [85], and peak-to-peak tissue displacement using acoustic radiation force impulse-induced shear wave was correlated to the tissue damage [86]. These two shear wave methods were based on the hypothesis that the tissue stiffness will be gradually reduced with liquefaction. Even though this metric outperformed the backscatter intensity for assessing tissue damage, using it for interrogating large volumes of liquefied tissue would be challenging, since shear waves do not propagate through a liquid. Further, liquefaction indicators derived from passive cavitation imaging (PCI) or sensing have also been explored in phantoms and ex vivo

tissue [87], [88]. PCI was shown to provide a more sensitive measure of tissue liquefaction compared to B-mode, although with limited axial resolution.

Another method of cavitation-induced tissue damage assessment was termed bubble-induced color Doppler (BCD). In BCD, each HIFU pulse is followed by a color Doppler ensemble to elicit the acoustic responses of and/or detect the dissolution of the residual bubbles. Thus, BCD is a sensitive means to detect the presence of bubbles and potentially evaluate their size based on dynamics of their dissolution [46]. In the context of microtripsy, where a very short HIFU pulse is used to generate a large contiguous bubble at the focus, its expansion, collapse, and subsequent surrounding tissue motion are affected by the amount of liquid around the bubble, thus it could serve as metric for tissue liquefaction. According to the studies using BCD in cavitation-cloud histotripsy [47], [89], [90], the spatially averaged velocity over the cavitation cloud area is directed away from the HIFU transducer immediately after the pulse and then tissue rebounds in the opposite direction in about 10 ms. It was reported that the time when the rebound velocity reaches its peak increases and then saturates as the tissue is liquefied.

In this paper, BCD was applied to BH with the goal of developing quantitative metrics of tissue liquefaction based on the observations of the motion of bubbles and tissue debris within the lesion following BH pulses. Compared to cavitation cloud histotripsy, a single BH pulse is much longer and expected to transfer a much higher momentum to the tissue at the focus. Bubble dynamics and distribution following each BH pulse are also different: relatively large bubbles are slowly dissolving (rather than collapsing) and are distributed throughout the lesion [73]. With these considerations, we hypothesize that the bubbles and tissue debris will move within the liquefied lesion due to HIFU radiation force, at progressively higher velocity as the tissue is more liquefied. This Doppler-measured velocity could then serve as quantitative metric of tissue liquefaction. To

test this hypothesis, the following experiments were performed. First, anticoagulated bovine blood and intact bovine myocardium were considered as the limiting cases of fully liquefied and fully intact tissue, correspondingly. The tissue motion induced by BH pulses of varying amplitudes was investigated experimentally using high pulse repetition frequency (PRF) color Doppler. Then, volumetric BH treatments of different duration were performed in bovine myocardium, and the resulting lesions were bisected and evaluated grossly for size and degree of liquefaction. Thus, obtained observations of lesion progression were correlated with Doppler-measured velocity maps within the lesion following each BH pulse, and candidate metrics were proposed for determination of treatment completeness.

4.2 METHODS

4.2.1 *Experimental Setup*

The experimental setup used in this study is illustrated in Fig. 4.1. A 1.5 MHz 256-element spiral array with electronic focus steering custom-designed for volumetric BH treatments of abdominal organs (IMASONIC, Voray-sur-l'Ognon, France) was driven by a power enhanced Verasonics V-1 acquisition platform (Verasonics Inc, Kirkland, WA, USA) [91]. The transducer has a 14.4 cm aperture and 12 cm radius of curvature (f-number of 0.83) and circular central opening of 4 cm diameter to accommodate an ultrasound imaging probe. A typical BH pulsing protocol was used: 10 ms pulses were delivered at PRF of 1 Hz [92]. A 64-element phased array with 2 cm aperture (ATL P4-2, Phillps, Bothell, WA, USA) coaxially mounted at the central opening of the HIFU array was controlled by a separate Verasonics V-1 system for B-mode and BCD imaging. The HIFU and imaging transducer assembly was placed into a tank filled with de-ionized and degassed water at room temperature, with dissolved oxygen less than 10% of saturation level.

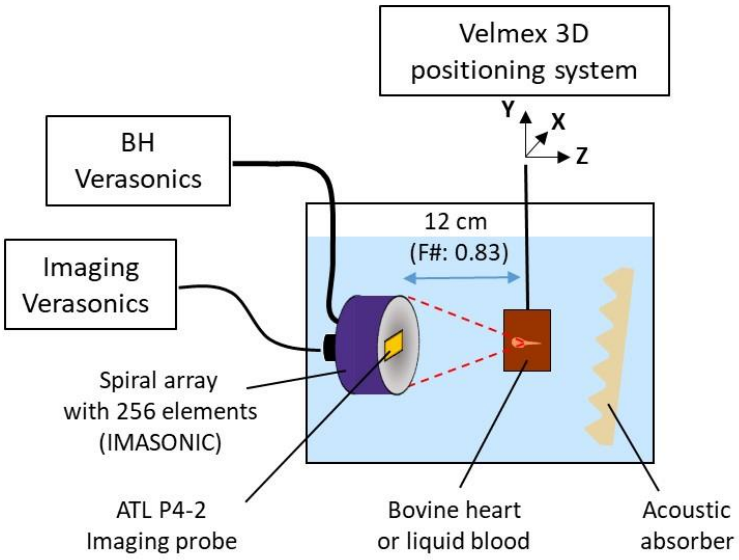

Figure 4.1. A schematic of the experimental setup for BH exposures of liquid blood or ex vivo tissue samples and data acquisition for coaxial B-mode and Doppler imaging. 256-element HIFU array and ATL P4-2 imaging probe were connected to separate V-1 Verasonics systems to control therapeutic and imaging pulses, respectively.

Fresh bovine myocardium tissue and blood were acquired from a local abattoir and treated within 48 hours. The blood was immediately mixed in a plastic container with the anticoagulant solution (CPD, No. C7165; Millipore-Sigma, St. Louis, MO, USA) at 9:1 volume ratio. The myocardium tissue samples were trimmed, degassed in saline in desiccant chamber for 1 hour, and embedded into degassed agarose gel to be fitted in a 4 × 4 × 8 cm size holder on the day they were obtained. The prepared tissues and blood were kept on ice in the refrigerator. Then immediately before the experiment the blood was degassed for 1 hour and poured into a latex balloon with approximately 8 cm diameter when expanded, sealed, and fixed in the holder. All tissues were kept at room temperature for approximately 1 hour before the experiment. The sample holders were attached to a 3D positioning system (Velmex Inc, Bloomfield, NY, USA) and placed into the water tank in front of the transducer focused inside the sample. A rubber acoustic absorber was placed behind the sample to reduce the reverberation artefact on US imaging.

Table 4.2. Physical Properties of Bovine Blood and Myocardium Tissue

	Density, kg/m^3	Sound speed, m/s	Attenuation, Np/cm (at 1.5 MHz)	Nonlinear parameter	Volumetric heat capacity, $J/C/m^3$	Dynamic viscosity, Pa·s	Shear wave speed, m/s
Bovine blood	1,060	1,580	0.036	4	3.834×10^6	3.65×10^{-3}	N/A
Bovine myocardium	1,060	1,570	0.09	4	3.940×10^6	N/A	5

4.2.2 *HIFU Focal Pressure Levels and Focus Position*

The HIFU focus position was pre-registered with the imaging system as described below. At shock-forming output level of the transducer, the maximum peak positive pressure position was found in water using a fiber-optic probe hydrophone (FOPH 2000, RP Acoustics, Leutenbach, Germany). The tip of FOPH in the corresponding B-mode image thus corresponded to the HIFU focus in water. To account for an axial shift of the focus position due to the difference of the sound speed in water and in tissue causing refraction at the water/tissue interface, additional adjustment of axial focus position was performed before each experiment. The average values for speed of sound in water and tissue were taken from the literature (Table 4.2), and Snell's law was used to estimate this additional shift (which ranged within 1-3 mm). The resulting HIFU focus position was displayed on the B-mode images as a pink cross.

The *in situ* peak positive (p^+), negative (p^-) pressures, and shock amplitude (p_s) at the HIFU focus in *ex vivo* tissue samples were obtained from numerical simulations of the nonlinear field using the Westervelt equation, performed for experimental conditions of our study. The simulation method and its validation by hydrophone measurements in water for this HIFU array is described in detail in previous studies [91], [93]. The acoustic properties of the samples used in the simulation are specified in Table 4.2 [66], [92]. The focal pressure levels noted throughout the manuscript were obtained from these simulations.

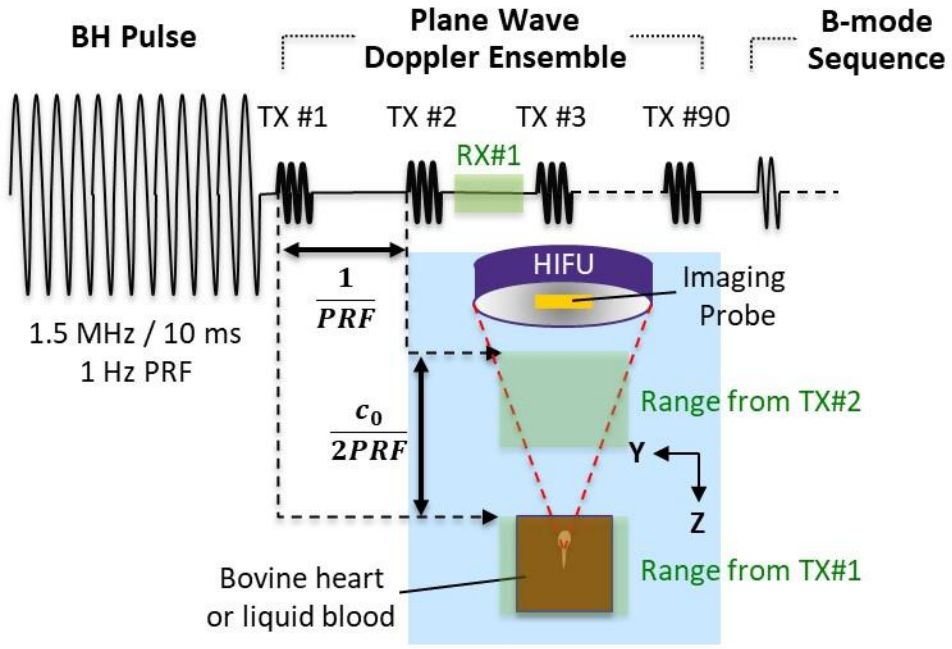

Figure 4.2. A schematic of ultrasound imaging sequence. 90-pulse plane wave Doppler ensemble was emitted immediately after the BH pulse, and then 48-ray-line B-mode sequence followed. Echoes from two consecutive Doppler transmit pulses (for example, TX#1 and TX#2) were received within a single receive gate. Echoes of TX#1 covered the region of interest, while echoes of TX#2 arriving at the same time corresponded to the area of water-filled standoff with minimal scattering, and thus did not contaminate the signal

4.2.3 *Ultrasound Imaging Sequence*

The ultrasound imaging sequence used in this work is illustrated in Fig. 4.2. Each BH pulse was immediately followed by a plane-wave Doppler ensemble and then a B-mode sequence. B-mode was conventional 48 ray-line imaging with 3 MHz center frequency and 4.5 kHz PRF. The beamforming and scan conversion processing of the B-mode was performed by Verasonics.

The plane-wave Doppler ensemble consisted of 90 pulses of 3-cycles with 2.81 MHz center frequency, 1.3 MPa pressure amplitude measured with needle hydrophone (HNR-0500, ONDA Corporation, Sunnyvale, CA, USA) in water at the HIFU focus, and the beam width of 1.6 cm / 0.45 cm at -6 dB level transverse / elevational, respectively. Kaiser amplitude window was used to suppress the side lobes when both transmitting and receiving the Doppler pulses.

Based on the round-trip time-of-flight in water calculated as

$$PRF_{max} = \frac{c_0}{2d}, \tag{4.26}$$

where c_0 is the sound speed and d is the distance from the probe to the furthest part of the region of interest (ROI), the maximum available Doppler PRF, PRF_{max}, for d = 18 cm is 4.2 kHz. With this PRF, the maximum measurable speed calculated as

$$|v|_{max} = \frac{PRF_{max} \cdot c_0}{4f_0}, \tag{4.27}$$

where f_0 is the center frequency of the Doppler pulse, is 52 cm/s [94]. The presence of velocities exceeding this value would cause an aliasing artifact on the BCD image. According to our preliminary studies, velocities of bubbles and debris inside the lesion immediately after a BH pulse could reach several meters per second, thus higher PRF was needed to avoid aliasing.

To address this challenge, high-PRF plane-wave Doppler was used as illustrated in Fig. 4.2. A twofold increase of the PRF was achieved based on the fact that at least half of the propagation distance from the imaging transducer to the ROI was occupied by water with minimal scattering. Unlike conventional Doppler imaging, in high PRF Doppler, the imaging probe transmits two pulses within the round-trip time of the flight window, for example, TX#1 and TX#2 (Fig. 4.2). Although echoes from the two pulses are recorded within one receive gate, the gate can be positioned in such a manner that echoes from the first pulse would cover the ROI, whereas echoes from the second pulse could only arrive from the water-filled standoff with no scattering. With this technique, PRF and the corresponding maximum measurable speed can be increased twofold and reach 9.375 kHz and 128 cm/s, respectively. At this PRF, the 90-pulse Doppler ensemble was 9.6 ms long.

4.2.4 *BCD Signal Processing*

Scan-converted in-phase and quadrature (I/Q) data was saved onto the internal hard drive by Verasonics, and then post-processed to obtain BCD images. The I/Q data were converted into BCD images within a sliding processing window that included 12 Doppler ensemble pulses and was shifted along the 90-pulse ensemble with a step size of 1 pulse to obtain each BCD image, for a total of 79 BCD images. Conventional color Doppler processing in MATLAB was used for each of the 12-pulse processing windows as follows. The slow-time data were wall-filtered with 2nd order infinite impulse response (IIR) high-pass filter with 80 Hz cut-off frequency. Because only 12 pulses were included in the processing window, projection initialization technique was implemented to improve the high pass filter performance [95]. Doppler power and velocity were then calculated per Kasai *et al.* [45], using autocorrelation algorithm with one sample lag $R(1)$. Doppler power, defined as the absolute value of $R(1)$, and mean Doppler frequency shift ($\bar{\omega}$) defined as the product of Doppler PRF and phase of $R(1)$ were calculated. The axial component of the velocity $\bar{v}$ then was obtained as directly related to $\bar{\omega}$:

$$\bar{v} \cdot cos\theta = \frac{\bar{\omega} c_0}{4\pi f_0}, \tag{4.28}$$

where θ is the angle between the direction of motion and Doppler pulse propagation direction. Because it was expected that motion of the bubble remnants and tissue debris would be induced by acoustic radiation force, which is primarily directed axially, the dominant component of the velocity was also expected to be axial. This expectation was validated qualitatively by observing the real-time B-mode image during the anticoagulated blood experiment described in the following paragraph (Supplement videos 1 and 2). Thus, hereinafter the axial velocity $\bar{v} \cdot cos\theta$ will be referred to as the velocity. Next, the BCD image pixels Doppler power falling below power

threshold were identified and assigned zero value. The power threshold was selected as the larger value of the double average of Doppler power level and the power level corresponding to the maximum background noise. To display the resulting velocity maps, a traditional color Doppler colormap was used: motion directed towards the imaging probe was assigned a positive sign and warm color range (red to yellow), and motion directed away from the transducer - the negative sign and cold color range (blue to cyan). For display, the BCD images were overlaid onto the corresponding B-mode image.

4.2.5 *BH Exposures of Anticoagulated Blood*

Anticoagulated blood served as a model for a limiting case of very large, fully liquefied BH lesion. The HIFU array focus was positioned inside the 8 cm diameter blood-filled balloon, at a distance of 2 cm from its proximal surface. BH pulses were delivered to this single focus location at different BH output levels. The *in situ* p^+ and p^- within each pulse were 4.3 −124.2 MPa and -3.5 −-17.1 MPa, respectively, based on the simulation as described in the previous section. BCD data were acquired 5 times per BH output level. Each acquisition was separated by at least 5 seconds to allow enough time for the movement from prior BH pulse to stop. In order to increase Doppler signal to noise ratio (SNR) for lower BH levels and correspondingly lower flow velocities, a larger Doppler processing window was used. Instead of using 12 pulses as with the higher range (*in situ* p^+ = 101.9 – 124.2 MPa), 40 and 85 pulses were applied for p^+ = 17.5 – 87.8 MPa and p^+ = 4.3 – 14.1 MPa, respectively. This increased overall ensemble length from 1.3 ms to 4.3 ms and 9.1 ms, respectively and the associated averaging of the velocity measurement over that time period was not expected to affect the measurement precision substantially. To measure the higher velocities in excess of 200 cm/s for *in situ* p^+ at the range of 101.9 – 124.2 MPa, $\bar{\omega}$ was compensated to range within -2π – 0 instead of -π – π, so that the measurable velocity range

was -240 – 0 cm/s. This approach is only possible when the velocity detected at every spatial point is expected to have the same direction as it was in a liquid. For each exposure the absolute value of the maximum velocity within the ROI, v_{max} was extracted from the BCD image obtained within the first Doppler processing window.

4.2.6 *Single Focus BH Exposures of Soft Tissue*

Bovine myocardium tissue motion immediately following a BH pulse was investigated as the opposite limiting case using color Doppler measurements and theoretical estimations. To avoid tissue liquefaction, but still have sufficient Doppler SNR for velocity estimation, a BH pulse was delivered at the output level just below the boiling threshold. With this BH power, p^+, p^-, and shock amplitude (p_s) were 95.5 MPa, -15.2 MPa, and 76.4 MPa, respectively. The HIFU focus was positioned at the depth of 1.8 cm in tissue. A single BH pulse was delivered to the tissue, and the same procedure was repeated 11 times to the other locations in tissue. In terms of the Doppler processing, an IIR low pass filter was used instead of a high pass filter, because tissue motion was expected to be relatively slow. As a metric, v_{max} was investigated as a function of time after BH pulse.

The theoretical tissue velocity at the focus was calculated by considering radiation force from a nonlinear BH pulse with shock fronts on the tissue [96], [97], as

$$v_z(t) = \frac{\beta a f p_s^3}{6\rho^3 c_t c_l^5} V(T), \tag{4.29}$$

where β is the nonlinear parameter of tissue, a is the HIFU beam radius, f is the BH source frequency, p_s is the shock amplitude, ρ is tissue density, c_t is shear wave speed, c_l is longitudinal wave speed in tissue, and

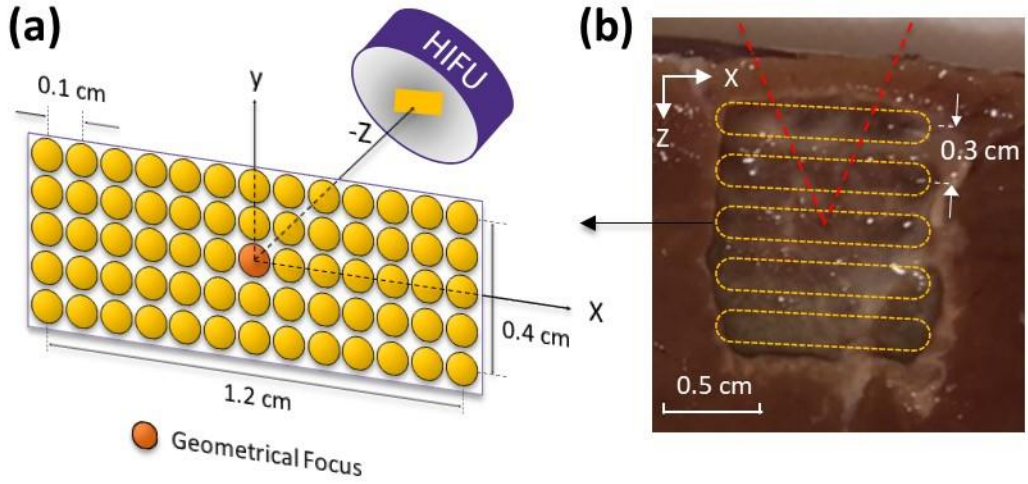

Figure 4.3. (a) Target locations marked as yellow circles: 65 target points spaced 0.1 mm apart in the -0.6 ≤ x ≤ 0.6 cm, -0.2 ≤ y ≤ 0.2 cm range within an elemental treatment volume. (b) Five elemental treatment volume with 0.3 cm spacing (yellow dashed contours) on the actual photograph of the composite-volume BH lesion bisected through the imaging plane x-z. Target locations (a) were located in the middle of each contoured area along the z coordinate.

$$V(T) = \begin{cases} 0 & (T < 0) \\ \frac{T}{1+T^2} & (0 < T < T_0) \\ \frac{T}{1+T^2} - \frac{T-T_0}{1+(T-T_0)^2} & (T > T_0) \end{cases}, \tag{4.30}$$

where $T = \frac{c_t t}{a}$, $T_0 = \frac{c_t t_0}{a}$, and t_0 is the BH pulse duration. According to Eq. (4.30), during the BH pulse, the velocity initially increases with time in the direction of ultrasound propagation, then decreases with $\frac{1}{T}$ asymptotic behavior. Immediately after the end of the BH pulse, the velocity in the opposite direction rapidly increases and then decays representing the first tissue rebound. The physical properties used in this estimation are listed in Table 4.2.

4.2.7 *Volumetric BH Treatments in ex vivo Bovine Myocardium*

Two types of volumetric BH treatments with electronic focus steering were performed in bovine myocardium samples and are illustrated in Fig. 4.3. The first type, resulting in an elemental-

volume treatment, corresponded to a 2D distribution of the discrete focus steering positions shown in Fig. 4.3(a). The distribution consisted of 65 target points in the X-Y plane (i.e. elevational plane of the imaging probe) orthogonal to the HIFU axis, and the central target point corresponded to the HIFU focus. The target locations were positioned in a 13×5 rectangular grid with 0.1 cm spacing: $-0.6 \leq x \leq 0.6$ cm and $-0.2 \leq y \leq 0.2$ cm. The steering limits of the BH beam in the elevational direction of the imaging probe were selected to be within the elevational beamwidth of the probe at the HIFU focus (4.5 mm). These limits allowed for expanding the ablation volume achievable with only electronic steering of the BH pulse. However, it was less sensitive to observe motion away from the imaging planes. Based on the hydrophone measurements, the pressure amplitude of the imaging pulse diminished to 88% and 57% one and two millimeters off the imaging plane. Nevertheless, this reduction in sensitivity still remained sufficient to image bubble motion. To achieve the same *in situ* pressure amplitude at all target locations *via* electronic steering, power compensation specific to each location per characterization reported previously [91] was applied. In this case, p^+, p^-, and p_s were 117.7 MPa, -16.6 MPa, and 108.2 MPa, respectively. The power compensation was achieved by controlling the apodization factor on all elements rather than the system driving voltage, as it provided faster switching between target locations and facilitated higher PRF of the BH treatment [91], [98]. A single BH pulse was applied to all 65 targets in the rectangular grid in a sequence, and the sequence was repeated until each location received 15 pulses. In each sequence, the central line within the imaging plane ($y = 0$) was treated first, followed by the lines just outside of the imaging plane, within the elevational plane: y = -0.1, 0.1, -0.2, and 0.2 cm. The order of the sonication points within a line was random.

The second type - composite-volume treatment - was achieved by merging five elemental-volume treatments along the HIFU axis *z* with 0.3 cm spacing (Fig. 4.3 (b)). One elemental-volume

corresponded to the position of the geometrical focus of the HIFU array, z = 0, two volumes were positioned postfocally (z = 0.3 and 0.6 cm), and the other two prefocally (z = -0.3 and -0.6 cm). To eliminate the shielding effect of the residual bubbles from the already treated area, the volumes were treated consecutively, moving from the furthest postfocal volume to the one most prefocal.

4.3 RESULTS.

4.3.1 *BH-Induced High Velocity Streaming in Anticoagulated Blood*

Two representative color Doppler images for lower (p^+ = 17.5 MPa, p^- = -9.0 MPa *in situ*) and higher (p^+ = 124.2 MPa, p^- = -17.1 MPa *in situ*) BH output levels are shown in Fig. 4.4 (a) and (b), respectively. The boundary of the latex balloon containing the blood is seen as a bright white interface in the background B-mode image at -2 cm axial location. While the observed velocity ranges are very different for these two cases, the direction of motion is away from the HIFU transducer as expected. At the lower output level, the maximum observed velocity of 35 cm/s was reached on the HIFU axis slightly postfocally (around 0.2 cm), whereas at the higher output level the maximum velocity was almost an order of magnitude higher (over 200 cm/s) and was reached about 0.6 cm postfocally. Theoretically, the maximum velocity would be expected at the focus where acoustic radiation force is largest. The observed postfocal shifts of the maximum may correspond to the fast-moving liquid displacement from the focus over the duration of the Doppler processing window. The area of detectable motion was also noticeably larger in both dimensions in the higher output case. In addition, a large hyperechoic area can be seen at the focus on the B-mode image in Fig. 4.4 (b) clearly indicating the formation of bubbles at that output level, which could enhance radiation force and streaming.

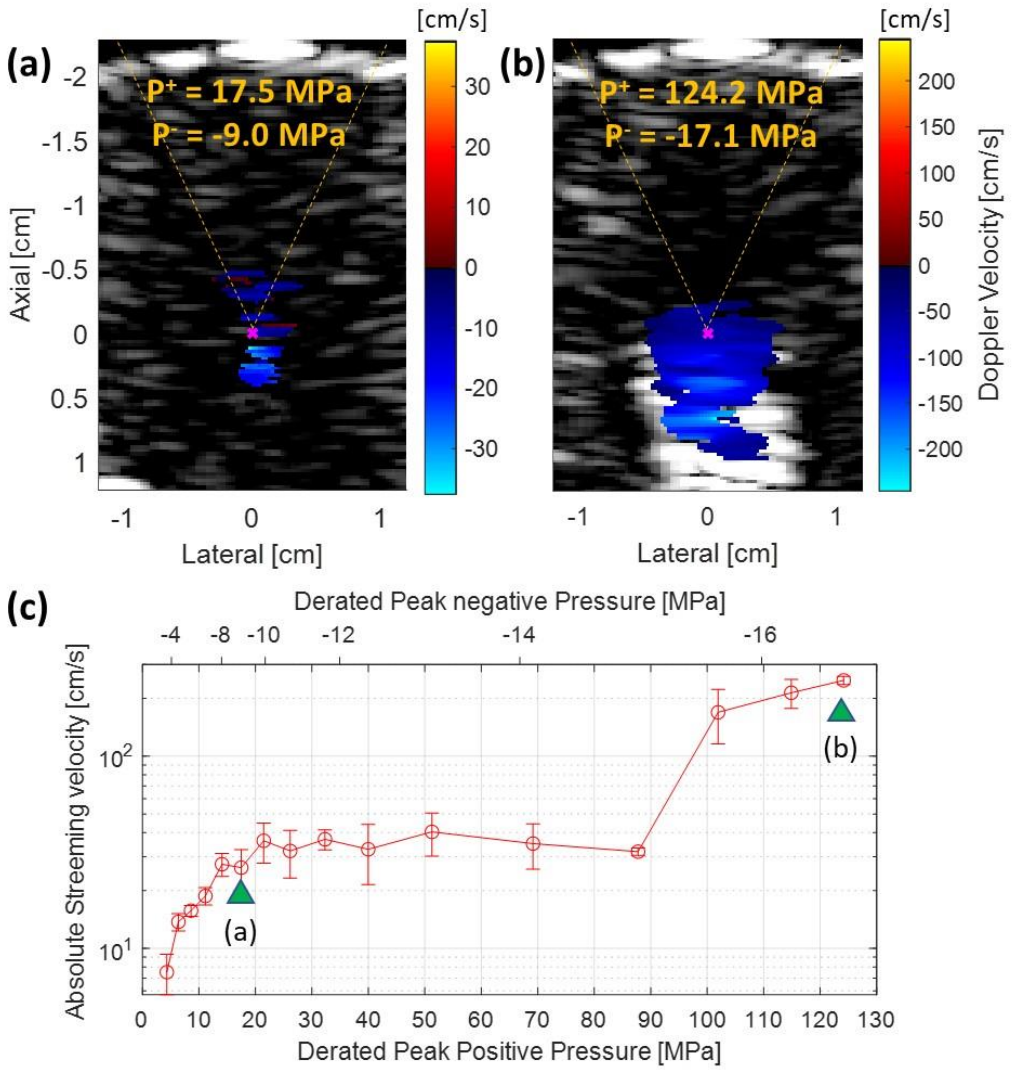

Figure 4.4. Blood streaming visualization by color Doppler for the low BH power (in situ focal pressures indicated in yellow) (a) and for the high BH power (b). The HIFU focus is denoted by the pink 'x' mark. (c) The measured absolute value of maximum streaming velocity in the liquid blood. Shock amplitude of 80.6 MPa is formed at 101.9/15.6 p+/p- peak focal pressures.

The value of the maximum velocity, v_{max}, determined from the color Doppler images immediately following the BH pulse and averaged over 5 different exposures is plotted in Fig. 4 (c) for different output levels corresponding to the *in situ* p^+ (bottom abscissa) and p^- (upper abscissa); error bars correspond to standard deviation. The measured maximum velocity values gradually increase, as expected, below p^+ = 20 MPa and v_{max} = 30 cm/s, then plateau at 30 - 40

cm/s within the range of p^+ from 20 to 90 MPa. This may be attributed to the fact that the turbulent effect begins at this velocity range. The velocity of 40 cm/s, at which the discrepancy becomes prominent, corresponds to the Reynolds number of 1,500, which is a little lower than what is generally considered as non-laminar flow (*Re* = 2,000). Further, blood is known to be a non-Newtonian fluid, with viscosity decreasing by orders of magnitude at high shear rates [99]. This can result in exponential increase in Reynolds number and significant turbulent effect as the streaming velocity increases. Interestingly, at 90-100 MPa there was a discontinuity: the velocity increased abruptly to about 200 cm/s and continued to grow with p^+. There are two potential reasons for this observation; first, this output level corresponds to the shock formation in HIFU focal waveform [91] and thus substantially increased acoustic radiation force [97]. In addition, a hyperechoic region corresponding to bubble activity was also first observed on B-mode images at that level, which would further enhance acoustic radiation force.

4.3.2 *BH-Induced Motion in Intact Soft Tissue*

The limiting case opposite to that of fully liquid medium considered above is the case of intact soft tissue in the absence of liquefaction. A representative example of a color Doppler image corresponding to the first 12 pulses in the Doppler ensemble is shown in Fig. 4.5 (a). Unlike the case of liquid blood, the tissue moved towards the transducer at low but detectable velocity of a few cm/s. This motion represents the rebound of elastic tissue following the termination of acoustic radiation force applied by the BH pulse. Note that the surface of the sample is also moving in the same direction, albeit at much lower velocity, although it is located outside of the focal area. Most probably this is due to the partial reflection of the BH pulse from the water-sample interface, and therefore enhanced radiation force. Fig. 4.5 (b) compares evolution of the measured and theoretically estimated velocity over time after the BH pulse. The mean and standard deviation

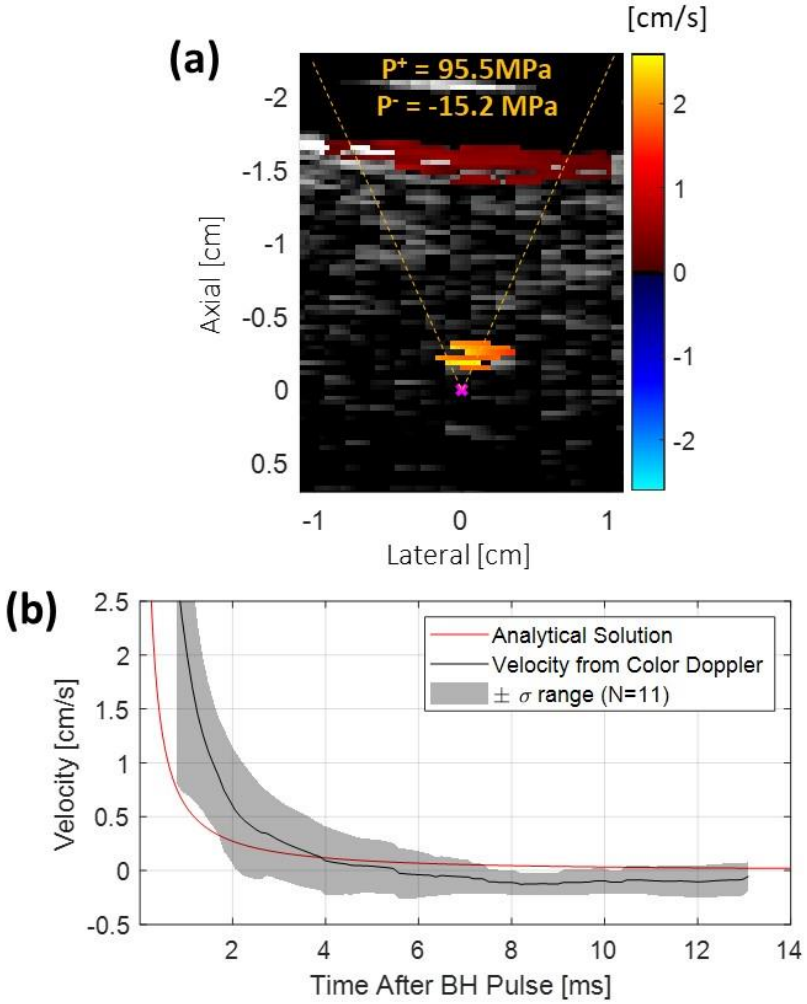

Figure 4.5. (a) Color Doppler image for the first Doppler processing window in myocardium tissue for pulsed exposures in the absence of boiling and liquefaction. (b) Tissue motion from the color Doppler compared to the analytical solution (Eq. 4 and 5). The mean value from 11 different Doppler acquisition is represented by black line and its standard deviation is shown as the transparent gray zone.

from eleven different acquisitions are represented by a black line and gray shade, respectively. The velocity values are in good agreement, and both graphs decline exponentially over time. Of note, the measured tissue motion changed direction within a 4 – 6 ms time frame, representing the second rebound. This second rebound was not observed in the theoretical curve because the theoretical model assumes uniform radiation force in the axial direction.

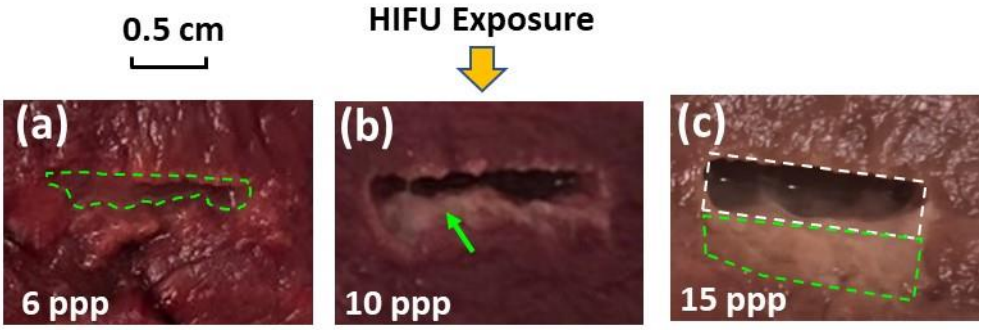

Figure 4.6. Photographs of the elemental-volume BH treatments bisected in the imaging plane after specified number of BH pulses per target point (ppp). BH pulse was incident from the top of the images. Green dashed boxes in (a) and (c) indicates partial liquefaction area and white boxes in (c) indicates fully liquefaction area

4.3.3 *Elemental-Volume BH Treatment*

Fig. 4.6 (a), (b), and (c) show representative photographs of the elemental volumetric BH lesions bisected along the ultrasound imaging plane after 6, 10, and 15 BH pulses were delivered per target point, respectively. All photos were taken after rinsing out the liquefied debris from the cavity. BH sonications were incident from top of the images in Fig. 4.6. Partial tissue liquefaction can be observed in Fig. 4.6 (a) within the lesion marked by the green dashed line. The proximal border is relatively smooth, but the distal border is irregular. On the other hand, the lesion (b) and (c) show more uniform liquefaction with sharp and smooth proximal and side boundaries and slightly irregular distal boundaries. For example, an area of residual connective tissue can be observed at the distal border on the left side of the cavity in Fig. 4.6 (b) marked as a green arrow. Notably, the lateral size of all three lesions is the same (1.3-1.5 cm) and corresponds to the size of the planned BH treatment grid. However, the axial size increases with the number of pulses and is about 0.2, 0.4, and 0.7 cm, after 6, 10 and 15 pulses, respectively. The degree of tissue fractionation also increases with the number of pulses. The most complete lesion in Fig. 4.6 (c) has a fully liquefied area of 0.4 cm axial size indicated as white dashed box and also has a wider blanched

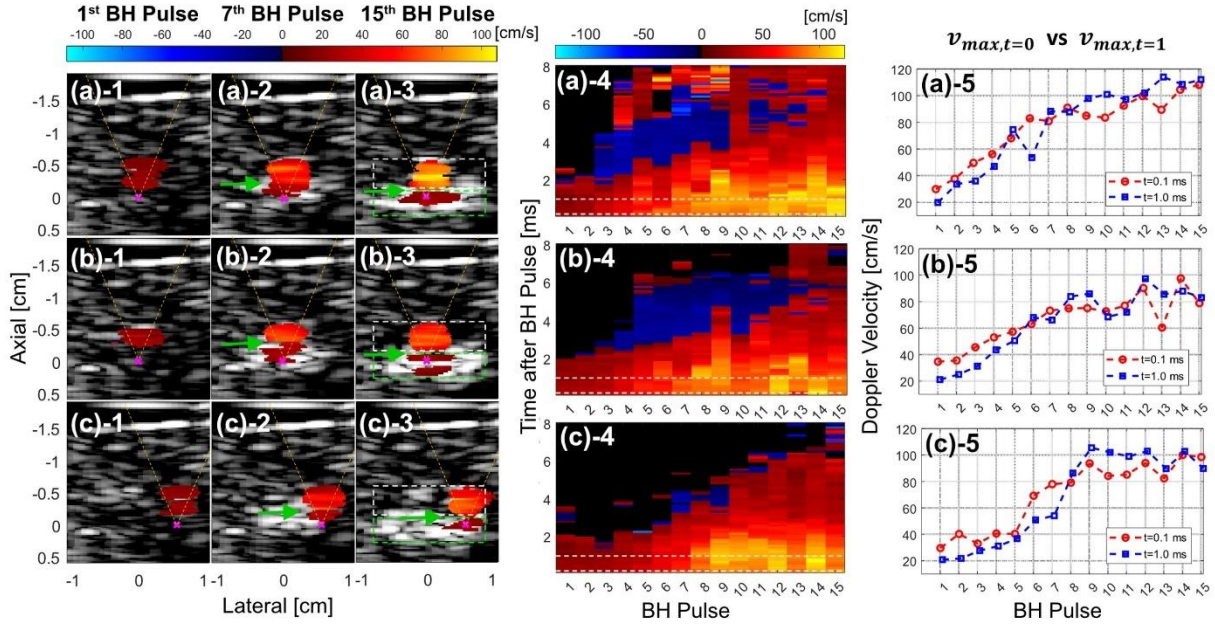

Figure 4.7. BCD images and metrics for elemental-volume BH treatment for three HIFU focus positions: (a) center (x = 0, y = 0), (b) furthest elevational margin (x = 0, y = 0.2 cm), and (c) furthest lateral margin (x = -0.6 cm, y = 0). The first three columns show BCD images for the 1st, 7th, and 15th BH pulses, the fourth column shows the maximum velocity determined from BCD with respect to the BH pulse number and time after BH pulse , and the fifth column shows maximum velocity dependence on the BH pulse number at two specific time points after the BH pulse corresponding to the white dashed lines in the fourth column: immediately (red dashed line), and 1 ms after BH pulse (blue dashed line).

border of 0.2 - 0.3 cm width at the distal border marked as green dashed box, which was observed previously in BH treatments of bovine myocardium [76]. The border most probably represented partially fractionated tissue resulting from incomplete merging of the distal "tails" of the BH lesions.

Fig. 4.7 shows the BCD images and corresponding metrics from a representative elemental-volume treatment. The top, middle, and bottom figures correspond to the target locations at the center (x = 0, y = 0), furthest elevational margin (x = 0, y = 0.2 cm), and furthest lateral margin (x = -0.6 cm, y = 0), respectively (target (a), (b), and (c)). BCD images in the left 3 columns in Fig. 4.7 are superimposed on the corresponding B-mode for the 1st, 7th, and 15th BH pulses at the

time point immediately after the BH pulse. As seen, the motion is directed towards the transducer regardless of target location and the number of BH pulses delivered. This behavior is similar to the intact tissue motion mentioned above, but the velocity is about tenfold higher, around 20 – 30 cm/s for the first BH pulse. The area of detectable motion in all target points after the first BH pulse is located 0.1 - 0.2 mm prefocally and is 0.28 - 0.49 cm axially. The axial size of that area is extended to 0.53 - 0.59 cm and 0.70 - 0.79 cm for 7^{th} and 15^{th} BH pulses, respectively. This size for the 15^{th} BH pulse corresponds well with the axial size of the BH lesion in Fig. 4.6 (c). The Doppler velocity is uniform for the first BH pulse; on the other hand, there is noticeable velocity variation axially as marked by green arrow for the 7^{th} and 15^{th} BH pulses: the velocities immediately above and below the arrow are 55 cm/s and 30 cm/s for the 7^{th} BH pulse (Fig. 4.7 (a)-2) and 71 cm/s and 22 cm/s for the 15^{th} BH pulse (Fig. 4.7 (a)-3). Also, the axial size of the area above the arrow is about 0.35 cm and 0.45 cm for the 7^{th} and 15^{th} BH pulses, respectively. The white and green boxes for the 15^{th} BH pulse indicate large and small velocity area, respectively, and correspond well with the fully and partially liquefied area mentioned in Fig. 4.6 (c). For the different target locations, overall size of the areas is similar, but the axial size in Fig. 4.7 (b)-1 and size above the arrow in Fig 4.7 (b)-2 are slightly smaller, which may result from the fact that the imaging plane is slightly outside.

Three figures in the fourth column show the maximum velocity value in the BCD images, v_{max}, with respect to the number of BH pulses and time after each BH pulse. As seen, for the 1^{st} and 2^{nd} BH pulses, regardless of the target location, the rebound tissue motion settles down in approximately 2 ms and no motion is detected after that. As the treatment progresses, i.e. within the range of the 3^{rd} – 13^{rd} BH pulse, the second rebound motion displayed in blue is observed, and its onset is gradually delayed from 2 to 5 ms. The second rebound is observed more clearly in (a)

and (b) compared to (c), which may be attributed to the fact that Doppler SNR for this laterally steered target was too low to detect all motion over entire time range so that the rebound motion for which Doppler power is lower than the threshold was filtered out.

In the rightmost (fifth) column graphs, the maximum velocity values v_{max} immediately after ($v_{max,t=0}$) and 1 ms after BH pulse ($v_{max,t=1}$) as functions of the BH pulse number are shown. The overall trends of $v_{max,t=0}$ and $v_{max,t=1}$ are very similar between the three focus positions (a)-(c): both metrics gradually increase from 20-30 cm/s to 90-100 cm/s over the first 9 BH pulses and then plateau. This saturation corresponds to the formation of adjacent fractionated lesion that 9-10 BH pulses can generate as shown in Fig. 4.6 (b). However, note that the initial value of $v_{max,t=1}$ is lower compared to $v_{max,t=0}$, whereas the saturation value is similar Therefore, $v_{max,t=1}$ appears to be a more sensitive candidate metric of the liquefaction progression. Specifically, the rate of change (ROC) between the maximum and minimum values for the $v_{max,t=0}$ and $v_{max,t=1}$ of target (a) is 262% and 475%, respectively calculated as

$$ROC(\%) = \frac{\max(v_{max},t=t_0)-\min\,(v_{max,t=t_0})}{\min\,(v_{max,t=t_0})} \times 100, \tag{4.31}$$

where t_0 is 0 or 1 depending on the metric.

4.3.4 *Composite-Volume BH Treatment in Bovine Myocardium Tissue*

Photographs in Fig. 4.8 (a), (b), and (c) show representative cross sections of the composite-volume lesions obtained by merging five elemental-volume lesions with a different BH pulse number: 5, 7, and 15 pulses per target, respectively. With 5 pulses per target (Fig. 4.8 (a)), noticeable residual tissues are observed throughout the lesion and the lesion boundary from intact tissue is unclear. With 7 pulses per target (Fig. 4.8 (b)), the lesion volume is more homogenously liquefied, with occasional strands of residual tissue attached to the surrounding intact tissue (green

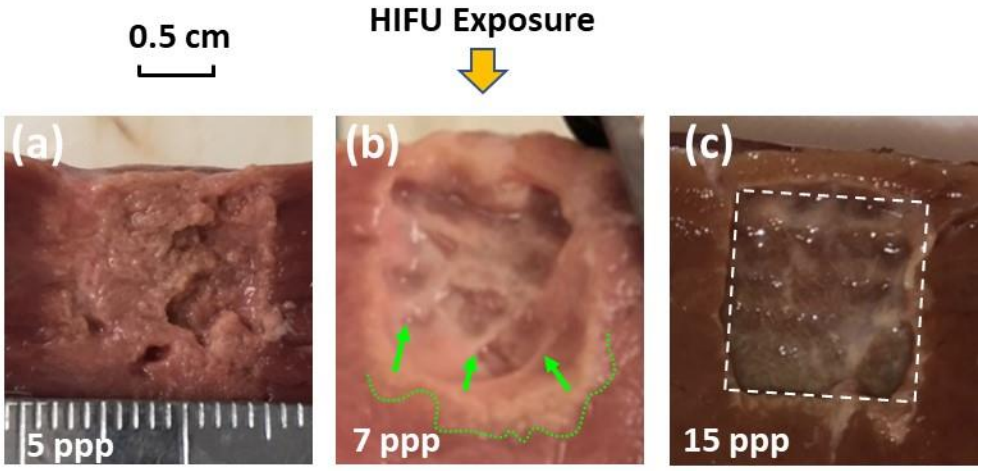

Figure 4.8. Photographs of composite-volume treatments bisected in the imaging plane after specified number of BH pulses per target point (ppp). The BH exposure of all lesions was directed from top to bottom of the images. White box in (c) indicates the targeted area.

arrows) and somewhat irregular boundary (green dashed line). Further increase to 15 pulses per target (Fig. 4.8 (c)) resulted in a homogenously liquefied volume with smooth and sharp boundaries.

Shown in Fig. 4.9 are BCD images corresponding to the 1st, 7th, and 15th BH pulses delivered to the central target point (x = 0, y = 0) at t =1 ms after sonicating the 2nd and 5th elemental-treatment volumes. Since the lesion was formed in order from postfocal to prefocal elemental-volumes, the size of the pre-existing lesion differed between the 2nd and 5th treatment volumes, as indicated by the white dashed box. A green dashed box outlines the current treatment volume with axial position corresponding to the boiling bubble shown on the B-mode for the 1st BH pulse of each treatment volume. Unlike a single elemental-volume treatment, the BCD observations here differ depending on the size of the adjacent previously treated tissue. In the case of generating the 2nd elemental-volume, motion is observed in the pre-existing first elemental-volume lesion as well as in the current treatment volume. The motion in both volumes is directed towards the transducer, but the velocities in the two volumes are quite different. The velocity inside the current volume is

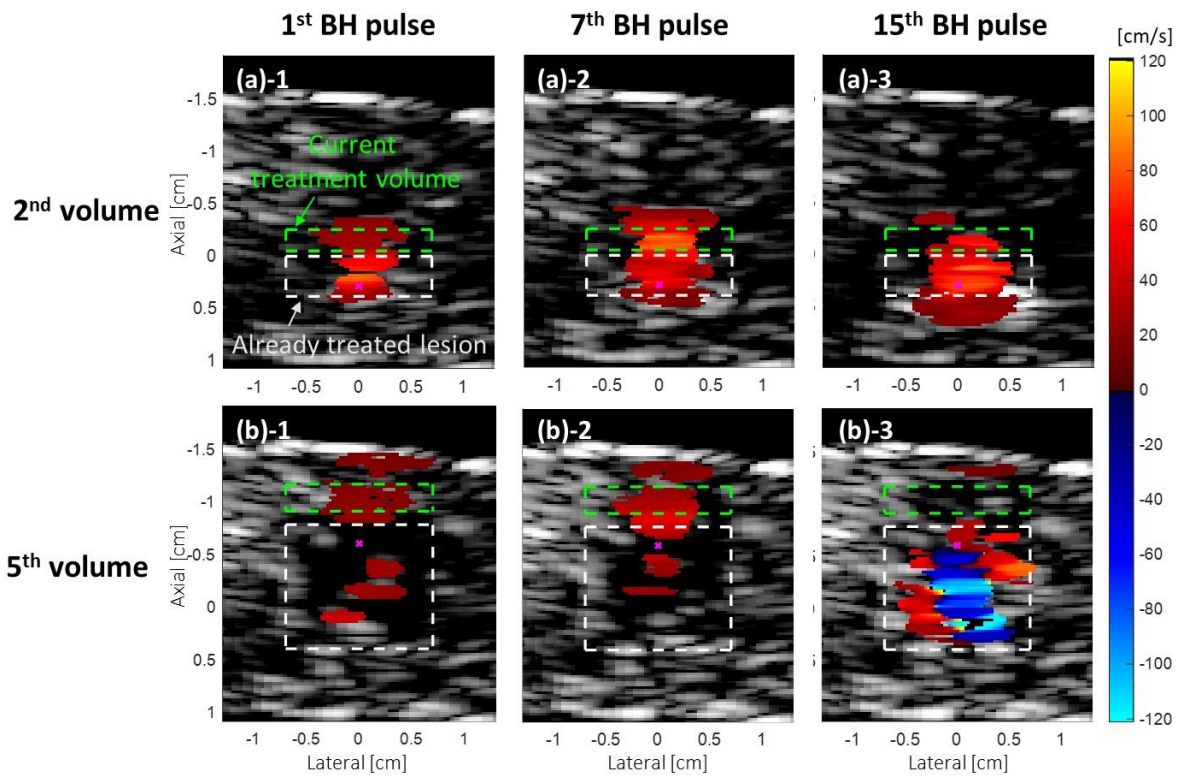

Figure 4.9. BCD images at 1 ms after BH pulse delivered to the central target point (x = 0, y = 0) for the 2nd (first row) and 5th (fifth row) elemental-treatment volumes that form a composite-volume BH treatment. Current elemental-volume treatment and previously treated volume are marked as green and white dashed boxes, respectively. The 1st BH pulse (first column), 7th BH pulse (second column), and 15th BH pulse (third column) were selected for the display.

initially lower than in the pre-existing one, then becomes higher for the 5th – 9th BH pulses, and lower again after the 10th pulse. The distal boundary of the lesion starts to be extended after the 7th BH pulse, similarly to the elemental-volume treatment. This fact also corresponds to the irregular distal boundary as shown in Fig 4.8. (b).

In the 5th treatment volume, with a large pre-existing liquid volume composed of four elemental volumes, several separate areas of motion towards the transducer are observed in both the current and pre-existing volumes, during the first part of the treatment, i.e. pulses 1st – 8th. Compared to the 2nd treatment volume case, the trend of maximum velocity location for the 1st – 8th pulses was similar; however, for the 15th BH pulse, diminished motion was detected in both the

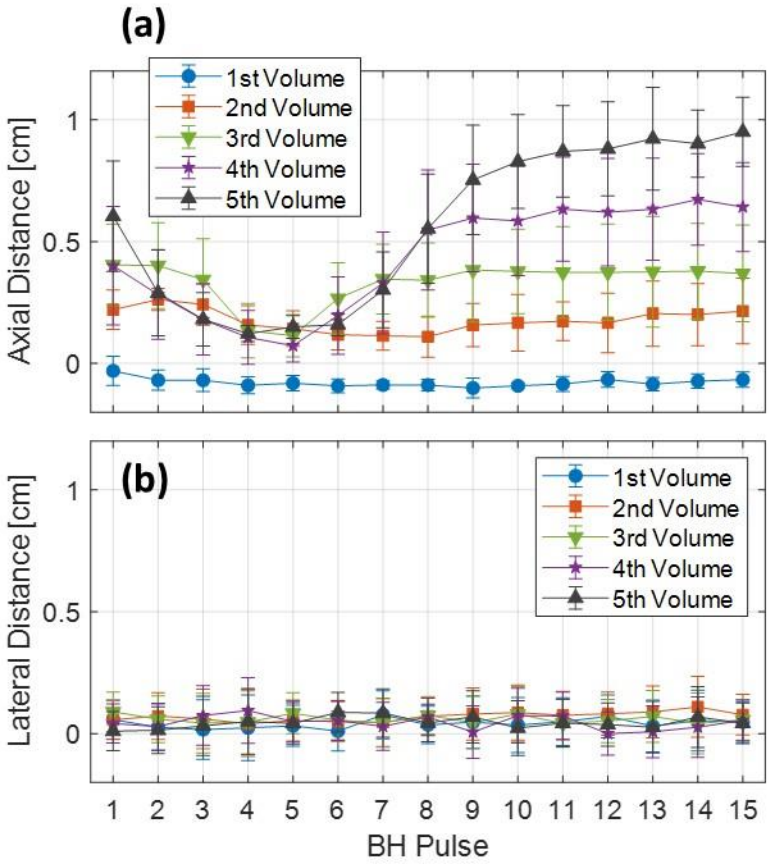

Figure 4.10. The axial (a) and lateral distance (b) between the target point and maximum velocity location for each of consecutive elemental treatment volumes averaged over all targets within the same elemental treatment volume. Error bars correspond to the standard deviation.

region distally to the pre-existing lesion and the current treatment volume. As the two volumes start to merge after the 8th BH pulse, the observed motion changes direction, i.e. streaming in direction of the wave propagation is observed, at gradually increasing velocity as treatment progresses. Ultimately, as indicated in Fig. 4.9 (b)-3, the streaming velocity reaches 120 cm/s, and streaming in the opposite direction develops on both sides of the focus, consistent with expectations for streaming in confined volume. This spatial pattern of velocity was only observed for the 4th and 5th elemental treatment volumes, i.e. only for large liquefied volume with axial size exceeding 1 cm.

Based on the above observations, additional metrics were investigated for the composite-volume treatment at $t = 1$ ms after BH pulse: the distance between BH target location and maximum velocity location ($\overrightarrow{\Delta x}_{max,t=1}$) and velocity at the target position ($v_{targ,t=1}$). These two metrics are determined for the current target location within a certain axial range that corresponds to the span of the current treatment volume (i.e. axial size of the green dashed box in Fig. 4.9). The distance $\overrightarrow{\Delta x}_{max,t=1}$ is a two-dimensional scalar defined as the lateral and axial distances between the location of $v_{max,t=1}$ and center point of the axial range within the ultrasound imaging plane. The values of $\overrightarrow{\Delta x}_{max,t=1}$ averaged over all targets within the same elemental treatment volumes for the BH exposure described in Fig. 4.9 are plotted against the BH pulse number in Fig. 4.10. Reflecting the observations from the BCD images above, the axial component of $\overrightarrow{\Delta x}_{max,t=1}$for the 2nd – 5th treatment volumes is positive, i.e. is distal relative to the center of the treatment volume. For those volumes, the metric is initially 0.2 – 0.6 cm, then it decreases to approximately 0.1 cm at the 4th – 5th BH pulse regardless of the treatment volume number, and then progressively increases and saturates depending on the treatment volume location. Interestingly, the saturation level for the 2nd and 3rd treatment volumes was nearly identical to the value corresponding to the initial BH pulse and was higher for 4th and 5th treatment volumes. Unlike the axial component of $\overrightarrow{\Delta x}_{max,t=1}$, its lateral component remained almost constant at 0.1 cm over all treatment points of all treatment volumes.

Based on the observations of BCD during composite-volume BH treatment described above, it is clear that v_{max} alone is not a reliable indicator of the degree of tissue liquefaction in the current treatment volume because of the interaction with the pre-existing distal volumes. At the same time, the lateral component of the maximum velocity location $\overrightarrow{\Delta x}_{max,t=1}$ is stable over the treatment and

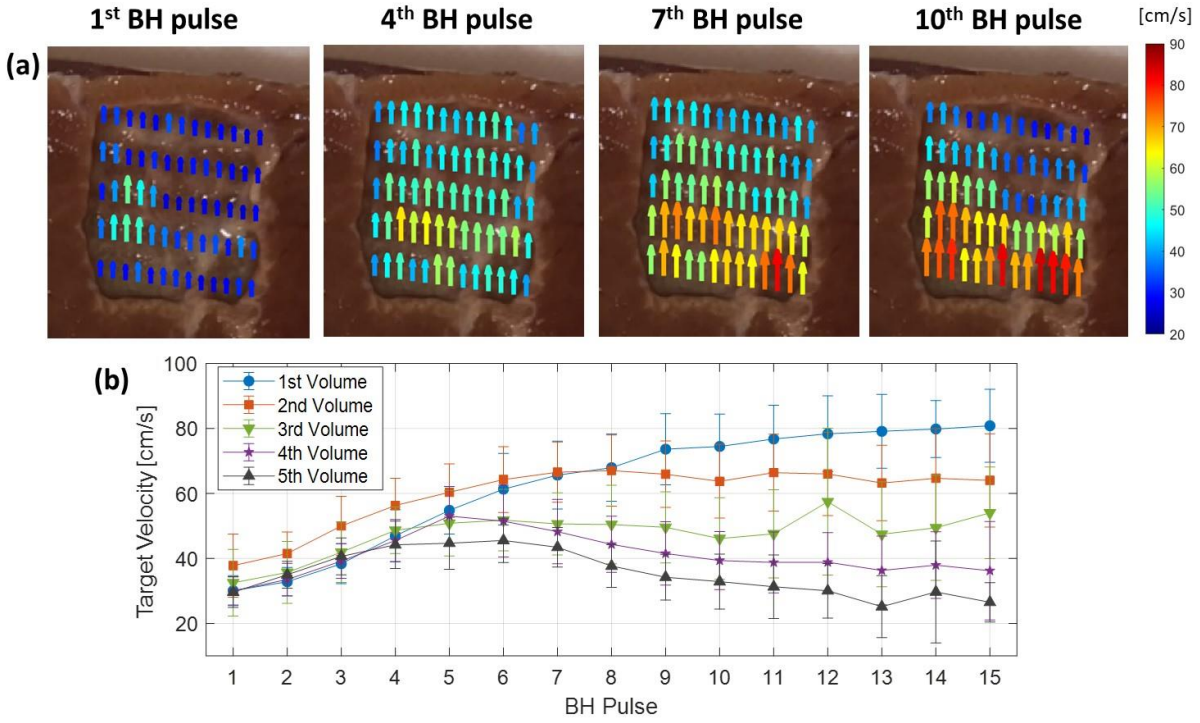

Figure 4.11. Target velocity map at 1 ms after a BH pulse (first row) for the 1st, 4th, 7th, and 10th BH pulse. The color and size of arrows correspond to the target velocity averaged over targets that lie on the same line in elevational direction. The position of arrows corresponds to the BH target point. Each arrow was acquired for the different number of BH pulses, but they are displayed together if the same number of BH pulse were delivered. The graph below (b) shows the target velocity averaged in all targets with respect to the BH pulse. Error bars correspond to the standard deviation.

is within 1 mm. For these reasons, maximum velocity at t = 1 ms after BH pulse within the current treatment volume, $v_{targ,t=1}$, was selected as a metric and termed "target velocity".

Fig. 4.11 (a) shows the $v_{targ,t=1}$ map for the selected BH pulses superimposed on the photo of the cross-sections of a lesion shown in Fig. 4.8 (c). Each arrow in the figure represents $v_{targ,t=1}$ averaged over targets along the elevational direction and positioned at the corresponding target location. As seen, the value of $v_{targ,t=1}$ is initially low and uniform across all target points, then gradually increases while maintaining its uniformity until around the 5th – 6th BH pulse. However, from the 7th BH pulse, the trends change depending on the treatment volume. For the 1st and 2nd

volumes (bottom two rows of arrows), the velocity continues to increase and slowly saturates. For the other three volumes it either does not change or decrease. For all elemental treatment volumes, the pattern of the $v_{targ,t=1}$ map does not change noticeably within the 10th – 15th BH pulses. The graph in Fig. 4.11 (b) shows $v_{targ,t=1}$ averaged in all targets within the same treatment volume versus the number of BH pulses. As expected, the line for the 1st treatment volume exhibits similar results to $v_{max,t=1}$ in the elemental-volume treatment. Specifically, it starts from 30 cm/s, gradually increases, and then saturates around 80 cm/s. The other lines saturate or decline due to the interaction with the pre-existing lesion. In general, these shifts in trend begin around the 5th BH pulse.

4.4 Discussion and Conclusion

In this chapter, I investigated tissue motion during BH-treatment using high PRF color Doppler imaging with the ultimate goal of identifying quantitative metrics of liquefaction progression and treatment completion. The experiments were performed in progressively more complex scenarios: 1) a single BH target in the two limiting cases of the target medium - liquid blood and intact soft tissue without liquefaction; 2) an elemental-volume BH treatment with 65 BH targets; and 3) a composite-volume BH treatment with 5 adjacent and merging elemental-volume treatments equidistantly distributed in axial direction.

The experiments with liquid blood showed that a BH pulse results in streaming in wave propagation direction at the focal region of the HIFU beam, with velocities dependent on the focal pressures. Conversely, intact soft tissue moves towards the HIFU transducer after a sub-threshold BH pulse with a much lower velocity, consistent with elastic rebound following axial displacement caused by acoustic radiation force.

One noteworthy observation from the BH exposures of liquid blood was that at the HIFU power sufficient to form a shock front in the focal waveform, bubbles were generated at the focus and streamed away from the transducer at much higher velocities (up to 200 cm/s). Whether the bubbles were gas or vapor bubbles or a mixture thereof was not clear, as boiling was unlikely to be achieved in liquid given the high streaming velocity of material through the focus, and shock fronts are also known to promote inertial cavitation [16], [64]. Regardless of the origin of bubbles, this result is aligned with the findings in the early study of cavitation cloud histotripsy [47], that when the bubbles are generated, the radiation force is significantly amplified, resulting in considerable velocity increase. Assuming that acoustic and mechanical characteristics of anticoagulated blood are similar to those of the liquefied tissue inside a BH lesion, this indicates that when tissue is liquefied at and around the HIFU focus, such a high-speed streaming can be expected. This could potentially play a role in tissue disintegration as well as serve as an indicator of treatment completion.

Tissue motion observations during BH treatment progression were qualitatively different for small (elemental) and large (composite) volume treatments. For axially small volumes, the motion was directed towards the transducer with gradually increasing and then saturating velocity as the treatment progressed from partially to fully liquefied tissue. This motion was consistent with elastic rebound of the tissue proximal and distal relatively to the forming lesion, and the velocity was about 10-fold larger than that at sub-threshold BH exposures of soft tissue. We speculate that there are two contributing factors that potentiate this behavior. First, similarly to the observations in liquid, when bubbles are formed in tissue at the focus, the radiation force and corresponding tissue displacement are both increased, thus increasing the rebound velocity. Second, as the tissue at the focus becomes more and more liquefied, the streaming velocity is expected to increase and

impact the distal border of the lesion, contributing to the tissue strain and subsequent rebound velocity after the BH pulse. If the HIFU focal region is axially larger than the lesion, the push imparted by radiation force will affect intact elastic tissues both proximal and distal to the liquefied lesion. In addition, in that case the streaming motion is weak due to the insufficient distance to build up and unlikely to continue in the constrained space following the BH pulse. Indeed, in larger composite volume BH treatments the high-speed streaming motion could only be observed when the size of the liquefied lesion was over 1 cm in the axial direction (Fig. 4.9 (b)-3), i.e. larger than the axial dimension of the HIFU focal lobe, which is 1.2 cm between the first nulls [91]. In these cases, neither the push induced by the radiation force nor the high-speed streaming jet reach the tissue distal to the already liquefied lesion. Therefore, the rebound motion of the distal tissue is diminished and high-speed streaming away from the transducer within the lesion can be observed (Fig. 4.9 (b)-3). Importantly, the maximum streaming velocity reached over 130 cm/s, similar to that in blood under the same acoustic conditions and therefore is expected to be similar across other soft tissue types. In addition to that, the vortical flow, a low speed reversed motion, was observed on both sides of the main streaming jet (Fig. 4.9 (b)-3) due to the confined volume of the lesion and the condition of continuity.

Thus, observation of streaming away from the HIFU transducer within the lesion could be a good candidate metric to ensure treatment completion in the case of large-size volumetric lesions, as it confirms the merging of the elemental treatment volumes as well.

As for candidate treatment progression metrics for smaller lesions, the maximum velocity within the whole motion-detected area (v_{max}) in an elemental volume treatment was observed to grow monotonically over the treatment time. More specifically, v_{max} measured 1 ms after BH pulse ($v_{max,t=1}$) outperformed v_{max} measured immediately after BH pulse ($v_{max,t=0}$) in

sensitivity because v_{max} is rapidly decaying within 1 ms after the 1st – 4th BH pulse. In addition, the target velocity at t = 1 ms ($v_{targ,t=1}$) defined as a maximum velocity within the target range also has a monotonical increment and saturation. Both metrics have the potential to be useful in determining tissue liquefaction in the elemental-volume BH treatments.

The aforementioned candidate metrics are not applicable to the lesions with axial sizes between those of elemental- and composite-volume lesions with < 1 cm size: $v_{max,t=1}$ does not represent the current treatment volume and is affected by the presence of distal liquefied volume; $v_{targ,t=1}$ saturates at 5th – 7th BH pulse that does not correspond to complete liquefaction; and high-speed streaming within the lesion is not observed. However, the axial component of $\overrightarrow{\Delta x}_{max,t=1}$ may represent a good metric in this lesion size range. This distance initially decreases with treatment time, as the location of maximum velocity shifts from a pre-existing distal cavity to the current treatment volume, has a local minimum at the 4th – 6th BH pulse, and then increases again and saturates after the 9th – 10th BH pulses, depending on the volume position (Fig. 4.10 (a)). We propose the following interpretation of this dependence. At the start of the treatment (1st – 5th BH pulses) the rebound motion in the current treatment plane is consistent both qualitatively and quantitatively with that of a separate elemental volume (Figs. 4.11 (b) and 7 (a)), and the velocity is initially lower than that in the liquefied distal cavity, but is monotonically increasing until it becomes comparable. This is reflected in the decrease of $\overrightarrow{\Delta x}_{max,t=1}$. Thereafter, the communication between the two lesion volumes – current and pre-existing – starts and causes the shift of the maximum velocity distally again, hence the increase of $\overrightarrow{\Delta x}_{max,t=1}$. Saturation of this metric could thus indicate full merging of the lesion volumes and thus serve as an indicator of treatment completion. In particular, in present case (2nd and 3rd treatment volumes in Fig. 4.10 (a)), $\overrightarrow{\Delta x}_{max,t=1}$ saturates at 9th – 10th BH pulse.

In summary, the following metrics could be considered as candidates for determining completion of BH treatments with 10 ms long pulse depending on the axial size of the lesion:

(1) Saturation of $v_{max,t=1}$ or $v_{targ,t=1}$ with respect to BH pulses for elemental-volume treatment.

(2) Saturation of the axial component of $\overrightarrow{\Delta x}_{max,t=1}$ to the value corresponding to the initial BH pulse for the small size volumetric lesion (less than the axial dimensions of the HIFU focal lobe, $<$ 1 cm for the current study).

(3) Observing high-speed streaming motion directed away from the transducer for large size volumetric lesion ($>$ 1 cm for the current study)

Note that for ablation volumes of different sizes one should plan on using different combinations of the metrics above.

In light of these considerations, the measurement from which the proposed metrics can be derived is the distribution of directional velocity along the HIFU propagation axis within an expanded axial range. This measurement can provide all three metrics: target velocity in the current treatment volume, maximum velocity location within the axial range, and the motion in the pre-existing, distal lesion. Note that such measurement does not require imaging. In fact, the SNR and spatial resolution of this measurement would be improved if the Doppler beam was in the form of ray-line, aligned with each HIFU focus location. The benefits of this approach will be investigated in future studies.

It is interesting to compare the physical mechanism of motion observed with different histotripsy methods – BH here and previously reported cavitation cloud histotripsy. In both methods, the tissue is observed to rebound after a treatment pulse but the mechanism and dynamics of momentum transfer to tissue are different. In BH, acoustic radiation force induced by a

millisecond-long ultrasound pulse causes the tissue displacement or liquid streaming away from a transducer during the pulse. Cavitation cloud histotripsy uses much shorter micro-second duration pulses that were shown to not impart significant radiation force [47]. Rather, the net motion of asymmetrically collapsing bubbles within the cloud during and after the pulses are hypothesized to cause the displacement away from the transducer [89]. After the pulse transfers the momentum to the tissue in both histotripsy methods, tissue rebounds toward the transducer. The amount of displacement and velocities are also vastly different – 1 cm/s for cavitation cloud histotripsy versus 30-100 cm/s for BH. Accordingly, different liquefaction metrics were proposed for the two techniques. In cavitation cloud histotripsy, the time-to-peak rebound velocity toward the transducer was found to grow and then saturate with tissue liquefaction due to progressively longer lasting bubbles. Importantly, in those studies, relatively small treatment volumes were considered (about 6 mm in size). In BH, the absolute rebound velocity rather than the time to reach it appeared to be a better metric and also potentially more practical for larger, clinically relevant treatment volumes.

This study has limitations; only a specific BH pulsing protocol (10 ms long BH pulse with PRF of 1 Hz) was used, and exposures were performed in one type of soft tissue - *ex vivo* bovine myocardium. We expect the BH pulse length and amplitude to affect the absolute velocity of both tissue rebound and streaming motions following BH pulses, because the momentum transfer caused by the radiation force from the HIFU pulse increases with both of these parameters. However, shorter BH pulses use higher amplitudes to achieve boiling within each pulse, which will have the opposite effect on absolute velocity. It is not immediately clear which effect will be dominant. However, we expect the qualitative trends to be similar and the proposed metrics applicable to these other arrangements. Similarly, tissue homogeneity, primarily in terms of

elasticity distribution, is expected to affect the absolute velocities, but not the key trends – saturation of the rebound velocity and initiation of streaming with treatment progression at the corresponding target locations. Those metrics could thus serve as indicators of local complete liquefaction of inhomogeneous tissues, with the spatial resolution corresponding to the spacing of the treatment grid. These considerations will be confirmed in future studies, and the proposed metrics will be validated by correlating them to 3D histology of the BH lesions.

Chapter 5.

DOPPLER-BASED ASSESSMENT OF BOILING HISTOTRIPSY-INDUCED VOLUMETRIC TISSUE LIQUEFACTION *IN VIVO*[4]

5.1 INTRODUCTION

Boiling histotripsy (BH) is a promising high-intensity focused ultrasound (HIFU) technique that produces mechanical tissue fractionation and liquefaction at the subcellular scale, offering a non-invasive alternative to traditional surgical treatment [4], [17], [21], [25], [26], [73], [75]. Within the BH technique, a series of millisecond long pulses (1-10 ms) are emitted, with focal peak negative pressure ranging from 9 to 19 MPa, delivered at a relatively low pulse repetition frequency (PRF) between 1 and 10 Hz. An essential prerequisite for BH pulses is the formation of shock fronts exceeding 40 MPa at the focus, which efficiently elevates the temperature to the boiling point within a few milliseconds (0.1 – 5 ms). Once boiling occurs and millimeter size vapor cavity is generated, the interaction with a following shock fronts induces tissue atomization with jet streaming at the vapor-tissue interface [22], [23] and generation of cavitation cloud proximal to the vapor cavity [25], resulting in mechanical tissue fractionation. The treated tissue is typically turned into liquid state with sharp boundaries and no discernible thermal damage. This tissue ablation capability of BH is now widely applied to various pre-clinical and clinical studies, including tumor ablation in liver [26], [27], [28], kidney [26], prostate [29], [30], [31], [32], and myocardium [28], [68], large hematomas [33], abscess treatment [34], [35], and immune response [30], [36], [37].

[4] *Manuscript in preparation for submission*

In terms of monitoring guidance during BH treatment, synchronized conventional ultrasound ray-line B-mode imaging is commonly used to capture images between BH pulses. This imaging technique is capable of detecting residual bubbles that were generated during the BH pulses and persist for a duration ranging from a few milliseconds to several seconds, thus enabling the B-mode imaging pulses to visualize these bubbles. However, B-mode imaging primarily provides qualitative assessment, which may lead to variability in interpretation among different practitioners. Along with the B-mode imaging, a pre-determined dose metric–the number of pulses delivered at each target point–is a common way to set up the end point of BH treatment. Although the prior study showed that this metric was well aligned with the extent of tissue damage in *ex vivo* liver and myocardium tissue shown in the histological images [28], the deterministic nature of the metrics could not allow the flexibility or real-time control in response to the unpredictable suppression of the boiling coming from various reasons such as subject's physiological motions, inhomogeneous tissue composition, or rib coverages. In light of these limitations in current monitoring guidance methods, the effective real-time technique, enabling both sensitive imaging of the treatment area and quantitative metrics to evaluate tissue liquefaction and determine treatment completion, would significantly enhance the accuracy and efficiency of BH treatment.

Recently, we proposed color Doppler-based metrics to address the limitations mentioned above [68]. This proposed technique was specifically designed to capture the translational motions of residual bubble in axial direction (*i.e.* along BH transducer axis) within the liquefied treatment volume immediately following each BH pulse. This was motivated by the hypothesis that the bubbles can move due to the intensive acoustic radiation force (ARF), and their velocity increases as the tissue liquefaction progressed. The study suggested that the maximum velocity, measured by color Doppler, gradually increased and reached over 1 m/s as the specific target point received

more BH pulses. Notably, the observed velocity was directed toward the transducer if the axial size of the liquefied volume was less than the axial dimension of the HIFU focal lobe, suggesting that the bubbles motion is influenced by the surrounding tissue elastic rebound motion induced by ARF.

Although the feasibility of the proposed Doppler imaging and metrics for tracking the movement of residual bubbles has been demonstrated in *ex vivo* myocardium tissue [68], these experiments assessed tissue liquefaction through gross evaluation of the bisected treated volume taken immediately after the treatment. Here, Doppler imaging and the corresponding quantitative metrics were tested on the abdominal tissues, specifically the liver and kidney, in *in vivo* pig studies. The effectiveness of these Doppler-based metrics was then assessed through their correlation with liquefaction quality, as determined by histological image evaluations.

5.2 METHODS

5.2.1 *Experimental Apparatus*

Fig. 5.1(a) shows a schematic of experimental setup for BH exposures within pig's abdominal organs in vivo. In terms of BH transducer, a 1.5 MHz 256-element composite piezoelectric type spiral array that we have used for many prior BH studies [68], [91], [100], [101], [102] was utilized (IMASONIC, Voray-sur-l'Ognon, France). The BH transducer was connected to an electronic controller, a power enhanced Verasonics V-1 system (Verasonics Inc., Kirkland, WA, USA). This setup provided precise control of pulse timing and delay across different elements, enabling the electronic steering of BH beams without physically adjusting the transducer's position [91]. This transducer has an aperture size of 14.4 cm, focal depth of 12 cm, f-number of 0.83, and a circular center opening diameter of 4 cm for the imaging probe installation. The transducer was mounted to a robotic arm to control its position during the treatment, and the surface of the transducer was

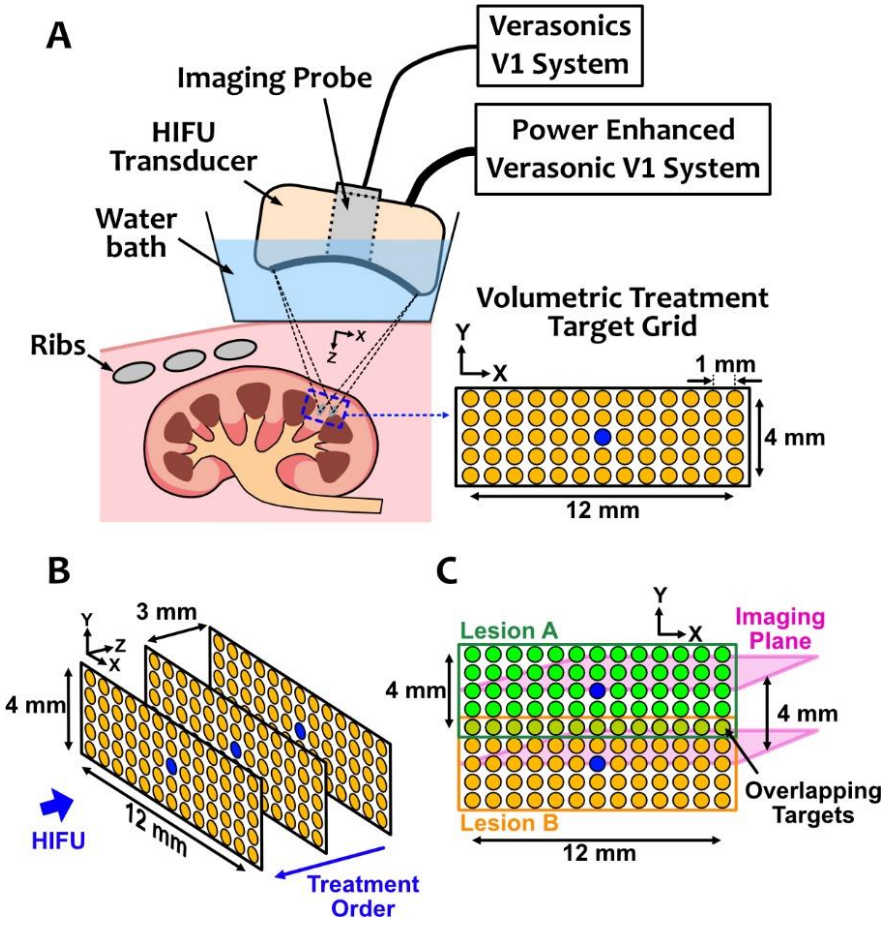

Figure 5.1. (a) Schematic of experimental setup for BH treatment within abdominal *tissue in vivo* in pig model. The BH transducer was capable of electronically steering the HIFU beam, enabling volumetric treatment. The treatment target grid plane covering lateral (x-axis) and elevational (y-axis) targets is shown on the right side. (b) The target grid arrangement for multi-layer treatment volume. (c) Combination of target grid layers in elevational direction; the layers overlapped by 1 mm.

submerged in degassed water for effective acoustic coupling. The imaging probe was either ATL P4-2 (Phillps, Bothell, WA, USA) or 3PE (Humanscan, Gyeonggi-do, South Korea), both of which have a similar -6 dB bandwidth of 2.0 – 4.0 MHz or 2.2 – 5.2 MHz, respectively. This probe was controlled by another Verasonics V-1 system for B-mode and color Doppler imaging.

5.2.2 *Animal Experiment Preparation*

BH treatments were performed to target the liver or kidney of four female domestic swine weighting 95 – 104 lbs. Total five exposures in the liver and three exposures in the kidney from four and two pigs, respectively, were collected for this study. The experiments were performed according to the protocols approved by the Institutional Animal Care and Use Committee at the University of Washington, Seattle, WA, USA. The pig was premedicated with Telazol and remained under anesthesia with isoflurane during the treatment. The pig's respiration rate was ranging from 17 to 28 breath/min with approximate axial and lateral displacement of 1.2 – 5.5 mm and 3.2 – 12.6 mm, respectively. In some cases of BH exposure, the pig's respiration motion was compensated based on either gating the BH pulse (n=2 for both liver and kidney) or controlling the axial position of the BH transducer using robotic arm (n=1 for liver and none for kidney); whereas the other exposures were not compensated (n=2 for liver, n=1 for kidney) [76]. The effect of these compensation methods was expected to be limited in this study because the velocities associated with pig's respiration motion were expected to be less than 3 cm/s, which is much lower than the expected velocity in the residual bubbles (30 - 100 cm/s). Following BH treatments, the animal was euthanized. Each targeted tissue volume, referred to as the lesion hereinafter, was then excised *en bloc* and preserved in 10% neutral buffered formalin. After fixation process, the lesions were cut into several segments along the US imaging plane and embedded in paraffin for histological sectioning and staining. From each segment of the lesion, a series of 5-micron thick histological sections at every 500 microns were collected and stained with Masson's trichrome (MT).

Table 5.3. BH Pulse and Imaging Parameters

Tissue	BH Pulse			Imaging Pulse				Motion Compensation
	Pulse Length	PPP	n planes	Probe Model	Pulse Type	Frequency, MPa	PRF, kHz	
Liver	10 ms	10	1	P4-2	Planewave	3	7.81	NA
		7	1	P4-2	Planewave	2.5	9.77	Gating
		7	1	P4-2	Planewave	2.5	9.77	NA
		7	1	3PE	Focused	3.75	10.05	Axial MC
		5	3	3PE	Focused	3.75	10.05	Gating
Kidney	10 ms	7	4	P4-2	Planewave	2.5	9.77	NA
		5	1	3PE	Focused	3.75	10.05	Gating
		5	1	3PE	Focused	3.75	10.05	Gating

5.2.3 *Boiling Histotripsy Pulse and Treatment Protocol*

A single BH pulse parameter set, conventionally used in our prior studies was used: 10 millisecond long pulses delivered at 1 Hz PRF (*i.e.* 1% duty cycle). The number of pulses per point (PPP) varied between the BH exposures, as specified in Table 5.1. The output level (*i.e.* system driving voltage) was set to be 10% higher than the boiling threshold that was determined prior to each volumetric BH exposure. The *in situ* peak positive, negative pressures, and shock amplitude at the HIFU focus for each BH exposure were ranging 113.9 – 135.1 MPa, -18.7 – -23.8 MPa, and 105.8 – 136.4 MPa, respectively. These pressure ranges were calculated from derating method using pressure level measured by hydrophone in degassed water and the attenuation coefficient of 0.054 and 0.122 Np/cm for liver and kidney, respectively [26], [65], [103]. The treatment target grid was predesigned and set prior to the treatment where the 65 target points were arranged with 1 mm spacing within 12 × 4 mm size plane (x-y plane) which is perpendicular to the imaging plane (x-z plane), as shown in Fig. 5.1(a). This dimension was determined by the maximum allowable HIFU steering limits along the x-axis and the furthest extent that could still be monitored within imaging plane on the y-axis. The treatment trajectory of target points was also predefined as follows: a) 13 targets on imaging plane (y = 0) including geometric focus (marked in blue in Fig. 5.1(a)) in randomly selected order, b) 13 targets in random order on lines outside the imaging

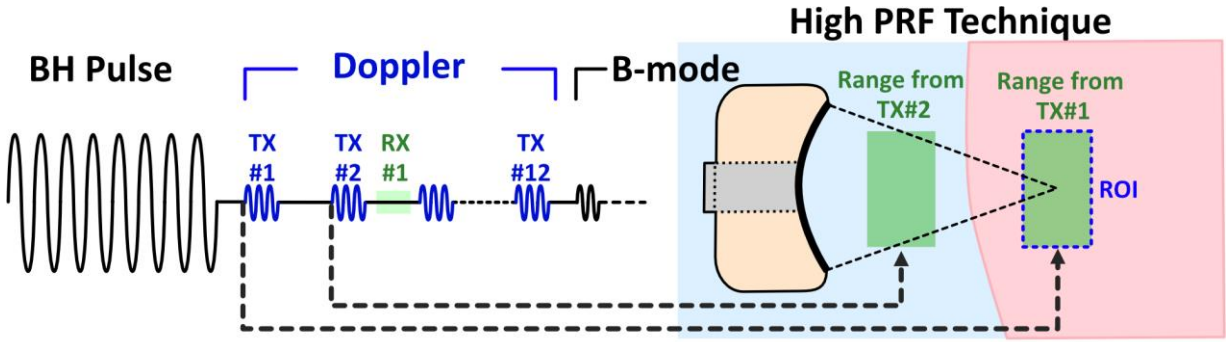

Figure 5.2. Imaging sequence for Doppler and B-mode. The high PRF technique was applied for Doppler ensemble, leveraging the gated receiving where the first pulse covers ROI while the second one covers water-filled standoff which has minimal scattering.

plane from near to far (y = -1, 1, -2, and 2 mm), and c) repetition of procedure a) and b) until each target point received the planned number of BH pulses. One BH exposure from liver and kidney was treated with multiple target grid planes in axial direction (z axis) where each grid plane was 3 mm apart from each other as shown in Fig. 5.1(b). In this case, the treat order between each target grid plane was from distal to proximal to the HIFU transducer to avoid the shielding effect from the residual bubbles within the pretreated volume. Two BH exposures for kidney were elevationally adjacent to each other with the 20% overlapping volume, as illustrated in Fig. 5.1(c).

5.2.4 *Ultrasound Imaging Sequence*

Immediately following each BH pulse, the imaging probe transmitted imaging pulses for Doppler and B-mode. The Doppler ensemble consisted of 12 pulses with a center frequency of 2.5 – 3.75 MHz, a pulse length of three cycles, and beam type of either plane wave or focused waves synchronized to the HIFU steering target point (Table 5.1). To increase the maximum measurable Doppler velocity, which is associated with the ultrasound center frequency and PRF, a high PRF technique was employed [68]. This technique breaks the maximum PRF limit of the traditional pulse-echo method by not waiting for the pulse to travel to and backscatter from the region of interest (ROI). Instead, two imaging pulses were transmitted within a single time-of-flight duration.

As illustrated in Fig. 5.2, the first pulse covers the ROI while the second pulse is traveling in a water-filled standoff with minimal scattering, enabling the assumption that the RF signal predominantly originates from the ROI. With this high PRF technique, the PRF was set to range from 7.81 to 10.05 kHz, with corresponding maximum measurable Doppler velocity of 97.7 – 146.6 cm/s.

5.2.5 *Doppler Signal Processing and Metrics Calculation*

The Doppler signal processing was performed offline using MATLAB 2022a (v9.12) (MathWorks, Natick, MA, USA). The input datasets were acquired directly by Verasonics with a data format as a 2-dimensional scan-converted in-phase and quadrature (I/Q) complex data corresponding to each Doppler pulse. A conventional autocorrelation-based color Doppler processing was performed to obtain the Doppler velocity maps per each BH pulse [45], [68]. The 12 I/Q dataset associated with 12 Doppler ensemble pulses were first filtered in slow time domain using third-order infinite impulse response (IIR) high pass filter with 100 Hz cutoff frequency and projection initialization due to the limited sample size [95]. The filtered data were then processed with one sample lagged autocorrelation, referred to as R(1), followed by Doppler power level-based thresholding. Here, the Doppler power map was defined as the absolute value of R(1) and the threshold level was set to 1.5 times the spatial average value of the Doppler power map. Doppler velocity maps were then computed as

$$\bar{v} = \frac{\angle\{R(1)\}\cdot PRF\cdot c_0}{4\pi f_0}, \tag{5.32}$$

where $\angle\{R(1)\}$ is the phase of R(1), c_0 is the sound speed in the medium, and f_0 denotes center frequency of imaging pulses.

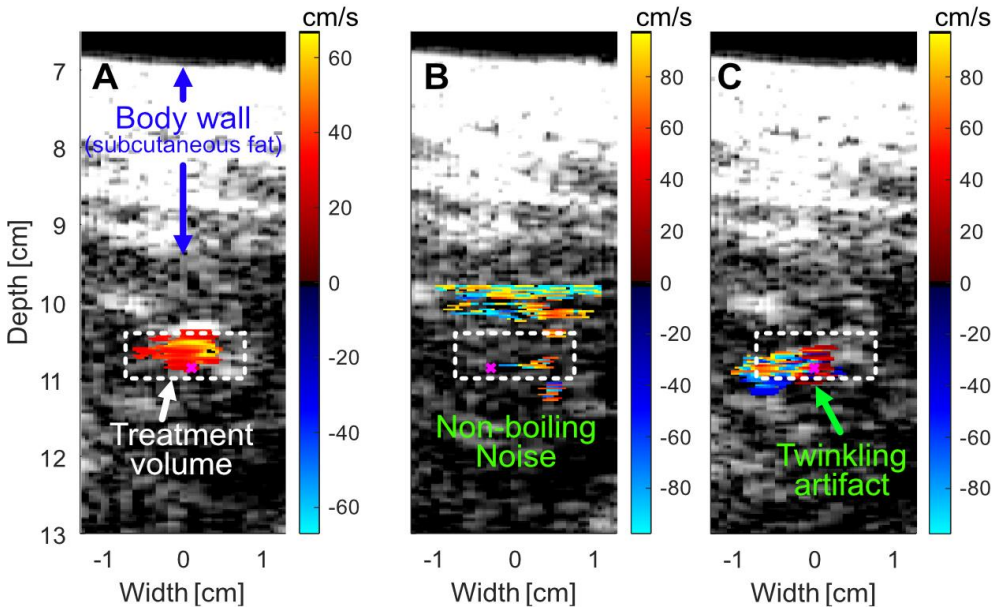

Figure 5.3. Doppler velocity maps for (a) boiling case, (b) the case in which the BH pulse amplitude was not sufficient to induce boiling and (c) cavitation activity induced at the blood vessels or bile ducts near the focus, which is characterized by twinkling artifact.

Following the acquisition of the Doppler velocity maps, the occurrences of boiling were assessed based on these maps. There were several factors that potentially inhibit heat deposition and boiling at the target area during the treatment, including the presence of blood vessels or bile duct–typically known for the resistance in boiling–and aberration which could be different depending on the focus locations. Fig. 5.3 shows representative Doppler velocity maps: Fig. 5.3(a) corresponds to the case when boiling occurs, whereas Fig. 5.3(b) and (c) show the cases where boiling did not occur. If the BH pulse amplitude was not sufficient to induce boiling, the Doppler velocity map was characterized by the random noise patterns (Fig. 5.3(b)) with the Doppler power level an order of magnitude less. Additionally, if the blood vessels or bile ducts were placed near the target point, cavitation was promoted within these structures, leading to the twinkling artifact-like patterns (Fig. 5.3(c)). In this case, the Doppler power level was comparable to that observed in boiling case. For further metric calculations, only cases where boiling occurred such as those shown in Fig. 5.3(a) were considered.

From our previous investigation in *ex vivo* pig's myocardium tissue [68], we calculated five metrics from the Doppler velocity maps for cases of boiling: maximum velocity (v_{max}), target velocity (v_{target}), lateral and axial distance between the BH target location and the location of maximum velocity (Δx_{max} and Δz_{max}, respectively), and the number of boiling occurrences. Here, the definition of v_{target} was the maximum velocity measured within a confined area around the target to which the corresponding BH pulse is delivered. The size of the area was laterally $\pm$ 1.5 mm from the target location and covered an axial range of 4 mm, optimally encompassing the region detected in the Doppler velocity map. These metrics were assigned to the specific target grid points, and then the metrics on the imaging plane (y = 0) at the last PPP and the elevational averaged metrics at the last PPP–averaging the values from points ranging from y = -2 to y = 2–were calculated.

5.2.6 *Histological Analysis of Tissue Liquefaction*

Of the histological sections taken every 500 microns for a single lesion, the image showing the highest degree of liquefaction (*i.e.* from the center of the lesion) was selected as representative and used for further analysis. In this representative image, the position of HIFU geometrical focus and its left-right orientation relative to the imaging plane were determined. This involved aligning the landmarks–stationary scatterers originating from tissue boundaries, large blood vessels, or bile ducts–in the corresponding B-mode image with the histological image. From the determined position of the HIFU geometrical focus, the planned target area was demarcated on the histological image. The dimensions of this target area were based on our prior observation [68]: a rectangular shape measuring 13 mm laterally (*i.e.* x-direction) and 4 mm axially (*i.e.* z-direction) for lesions treated with a single plane target grid, which was extended by 3 mm axially when an additional plane target grid was treated. This rectangular planned target area was further divided into thirteen

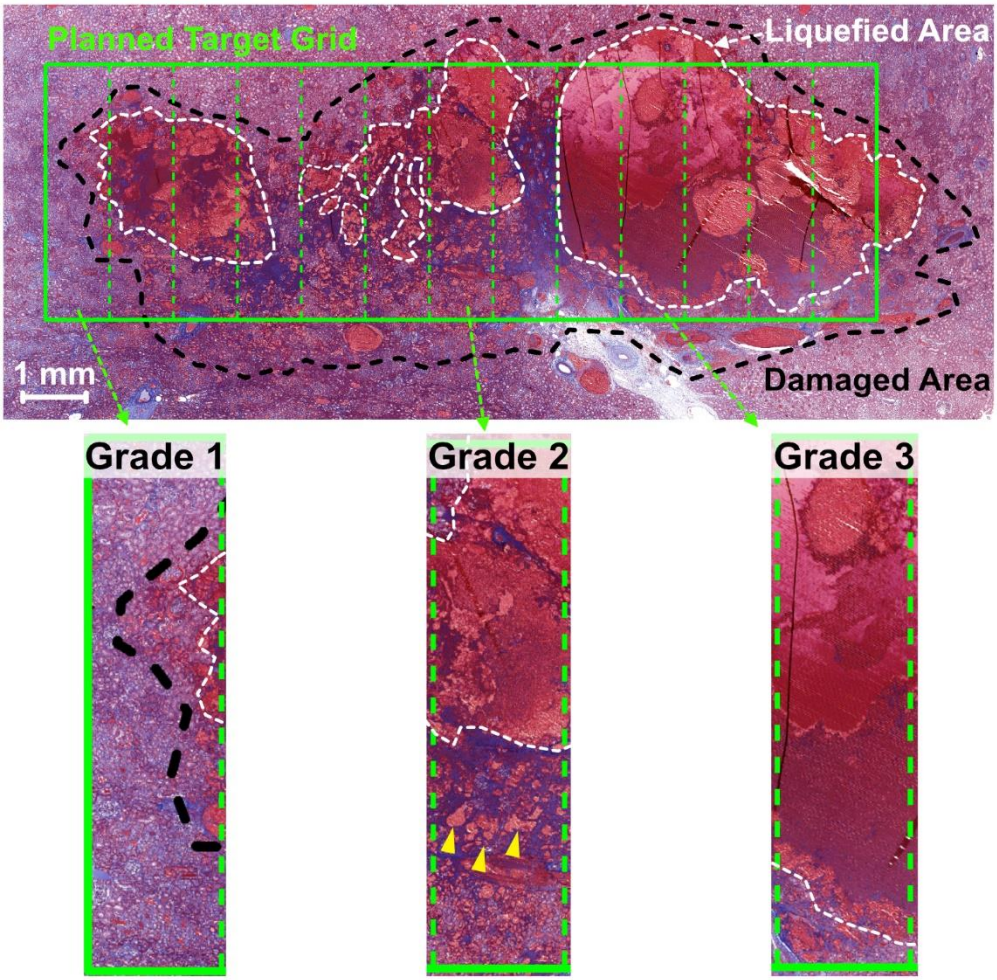

Figure 5.4. A representative example of a histological section with a zoom-in of each liquefaction grade: Grade 1 indicates a small liquefaction less than 0.5 mm in axial dimensions or only minor disruptions, Grade 2 denotes the liquefaction ranging from at least 0.5 mm of full liquefaction to less than 90%, and Grade 3 represents the complete liquefaction over 90% of area. The small liquefaction areas, distributed sparsely (yellow arrows in grade 2 section) were not considered to represent full liquefaction.

1 × 4 mm sections, corresponding to the 13-target grid in x-direction (x = -6 to 6). Fig. 5.4, for instance, shows a representative example of histological image along with planned target grid marked in green.

The extent of liquefaction within each of the 13 target grid cells was graded based on a three-level system [28], [72]. Grade 3 indicated that over 90% of the area showed full liquefaction

with tissue structures completely broken down to the subcellular level. Grade 2 encompassed liquefaction extents ranging from at least 0.5 mm of full liquefaction area in axial dimensions to less than 90%. Grade 1 denoted a liquefaction area less than 0.5 mm or only minor disruptions with gross or petechial hemorrhage. The section that included only intact tissue area was not considered for further analysis. In Fig. 5.4, the liquefied areas were outlined with a white dashed line, and the area corresponding to the three grades were indicated. The sparse liquefied volume less than 0.5 mm axially (marked with yellow triangles in grade 2 image in Fig. 5.4) was not considered as liquefied area.

5.2.7 *Comparison of Tissue Liquefaction Grade with Doppler Metrics*

The Doppler metrics associated with tissue liquefaction grades previously described were statistically analyzed, including all exposures for both liver and kidney tissue, respectively. The two-sample t-test between metrics corresponding to subsequent grades (between grade 1 and 2, and grade 2 and 3) was conducted and the statistical significance was indicated by asterisks (*: $p < 0.05$, **: $p < 0.01$, ***: $p < 0.001$, and ****: $p < 0.0001$).

5.3 RESULTS

5.3.1 *Progression of Tissue Liquefaction from Doppler Velocity Map*

Fig. 5.5(a)-(c) show the superimposed Doppler velocity maps and B-mode images captured after the 1st, 6th, and final (10th) BH pulses, respectively, for a representative liver exposure at a target point associated with grade 3 liquefaction level. The steered HIFU focal point, indicated by a green cross, was located beneath a 2 cm subcutaneous fat layer, 1.5 cm of an upper lobe of liver tissue, and 0.5 cm of a lower lobe of liver tissue. The corresponding photo taken after the treatment shown in Fig. 5.5(d) indicates the 15 mm long surface bruise on the lower liver lobe. The detected

area of bubble motion spanned approximately 5 – 8 mm laterally around the focus and 5 mm axially, ranging from the interface between the upper and lower liver lobe to the focus. It was observed that the axial position of the largest width of the detected area–marked as a green arrow and hypothesized to be the site of the strongest scattering due to the vapor cavity–initially positioned around 5 mm proximal to the focus and then gradually shifted towards the focus as treatment progressed. This trend aligns with the observations from our previous study [68], suggesting that the area of liquefaction gradually extended from proximal to distal. Additionally, the observed velocity was uniformly distributed and directed towards the transducer (*i.e.* positive velocity in red color), as expected, supporting that the tissue rebound motion predominantly affected the residual bubble motion inside the liquefied lesion. Furthermore, a few pixels of aliasing artifact–light blue pixels that have high negative velocity–were observed at the 10th BH pulse indicated by yellow arrow in Fig. 5.5(c), suggesting that the maximum Doppler velocity exceeded the measurable limit and was consequently underestimated, with the upper limit in this instance being 97.7 cm/s.

Fig. 5.5(e)-(f) show the four metrics observed from Doppler velocity maps–v_{max}, v_{target}, Δx_{max}, and Δz_{max}–tracked over the course of 10 BH pulses at the target point same as the one from Fig. 5.5(a)-(c). Two velocity metrics in Fig. 5.5(e) generally increased over the course of treatment, ranging from approximately 40 cm/s to 100 cm/s, with a fluctuation that may be attributed to the fact that the BH pulses do not always target exactly the same spot due to the pig's physiological motion, and there is tissue inhomogeneity in target volume. The increase in velocity in the last four pulses suggests progressive tissue liquefaction, providing more space for residual bubbles to move. In Fig. 5.5(f), Δx_{max}, and Δz_{max} exhibited some variability with the averages around zero and -2 mm (*i.e.* negative sign means proximal position relative to the focus),

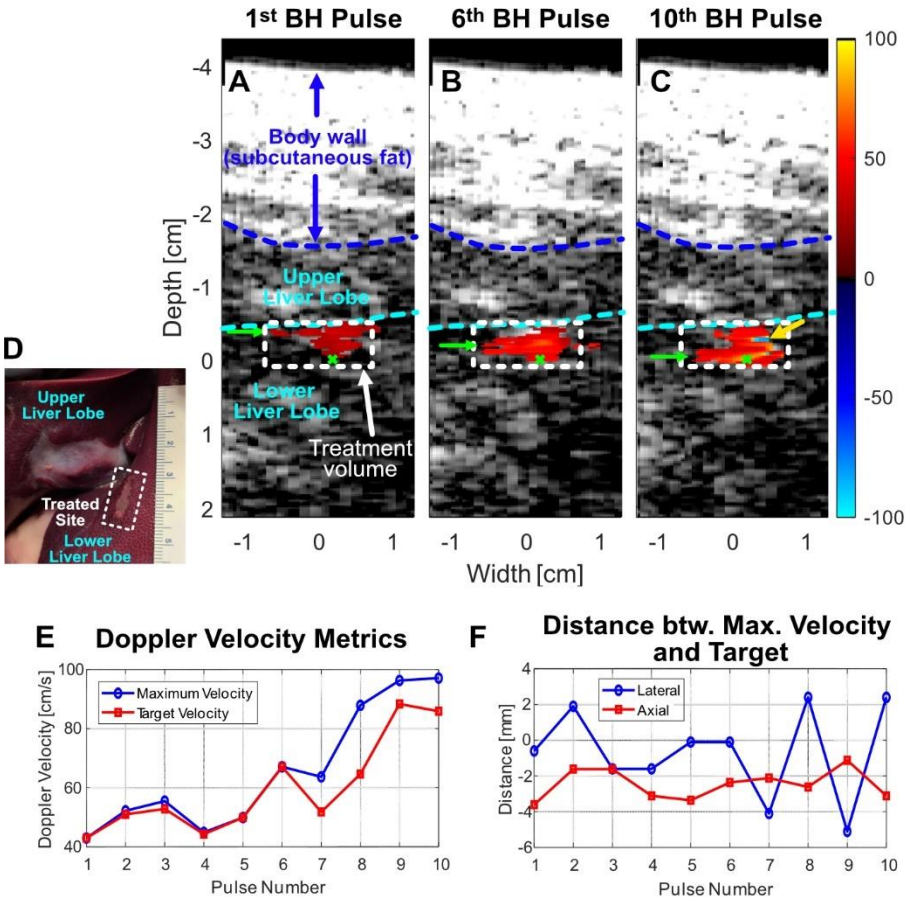

Figure 5.5. Doppler velocity maps in liver at a specific target location for (a) the first BH pulse, (b) 6th BH pulse, and (c) 10th BH pulse, showing the progression of lesion formation. (d) A corresponding photograph taken after the treatment shows the surface bruise on the lower liver lobe. The changes in Doppler metrics over the course of BH treatment: (e) maximum and target velocity and (f) distance between maximum velocity location and planned target point vs the BH pulse number.

respectively. No clear trends for both distances were similarly observed with our prior ex vivo tissue experiment [68]. Nevertheless, the observed variability was more pronounced, likely due to the BH pulse not to consistently targeting the exact same spot because of the respiration motions of the pig.

5.3.2 *Comprehensive Doppler Metric Analysis in Liver*

Fig. 5.6 presents a detailed analysis of Doppler metrics for a specific BH exposure in liver tissue, which is the same BH exposure associated with the Doppler velocity maps in Fig. 5.5, alongside the corresponding histological image and assigned liquefaction grades. This BH treatment was conducted without motion compensation, during which the pig exhibited peak cranio-caudal motion of approximately 12.6 mm and peak anterior-posterior motion of 5.5 mm. This cranio-caudal motion likely contributed to the smeared lesion appearance, characterized by 5 – 6 mm of mild disruption and partial liquefaction. In the histological image, the planned target grid is delineated with green lines, and the black and blue dashed lines outline the overall damaged area and liquefaction boundaries within the targeted sections, respectively. Adjacent to the histological image, the liquefaction grade for each section is shown. The target locations ranging from x = 0 to x = 4 were identified as the grade 3 level of liquefaction. The analysis included five metrics–the number of boiling occurrences, v_{max}, v_{target}, Δz_{max}, and Δx_{max}–measured at the BH pulse delivered to the targets on the imaging plane (blue bar charts) and elevational average with its standard deviation (yellow bar charts and error bar). Note that while the number of boiling occurrences was obtained by counting binary data across all delivered pulses per point (PPP), the other four metrics were specifically measured at the last PPP, in this case, the 10^{th} PPP.

The distribution of boiling occurrences aligned with the uneven liquefaction pattern shown on the left and right sides in the histological image. On the left side of the lesion, the BH pulses that did not induce boiling might cause widespread inertial cavitation. The maximum velocities (v_{max}) on the imaging plane for the grade 3 and 2 target location ranged from 65.4 to 97.3 cm/s and from 33.4 to 57.2 cm/s, respectively. The elevational averaged maximum velocity provided the smaller difference between the grades, but the variation within the same grade was smaller:

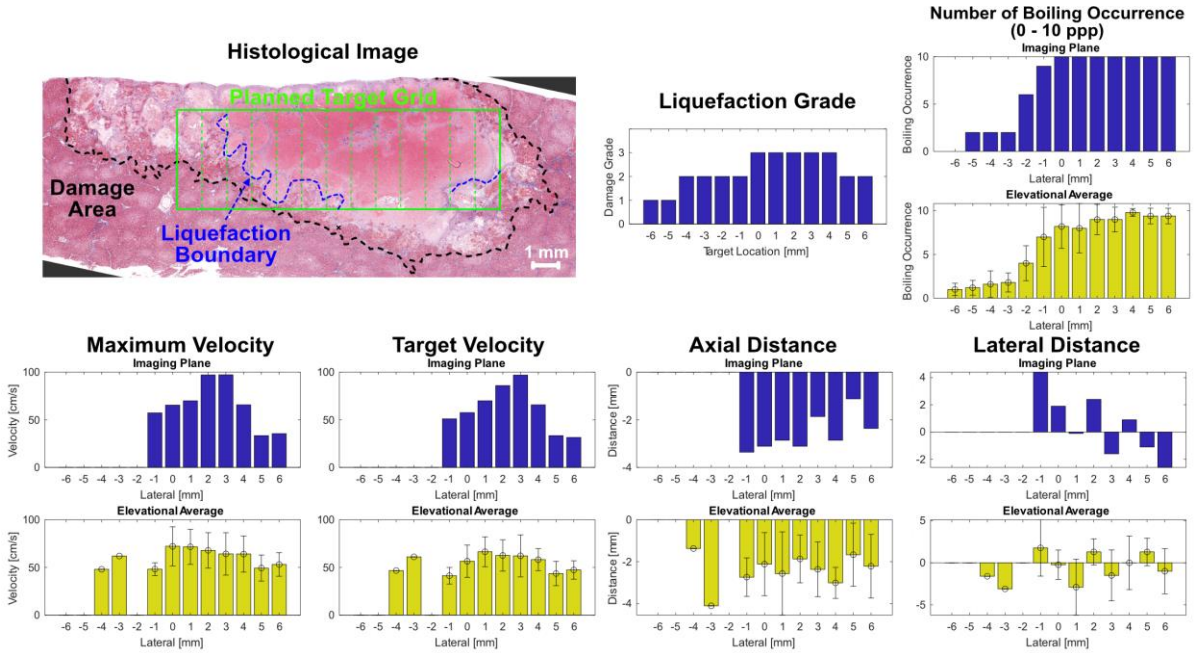

Figure 5.6. Representative example of a correlation between Doppler-based metrics with histological analysis in liver; the planned target grid is marked in green. The liquefaction grade and five metrics measured at both imaging plane (blue) and elevational average (yellow) are displayed using bar graph, showing the spatial distribution of those metrics within planned target grid. Error bars represent standard deviation.

grade 3 and 2 ranging from 64.1 to 72.2 cm/s and from 48.1 to 62.0 cm/s, respectively. The target velocity (v_{target}) showed similar results to the maximum velocity, as expected. Similar to Fig. 5.5, the axial (Δz_{max}) and lateral distance (Δx_{max}) indicated no clear distinction between the grades, but the overall values were around -2 mm axially–the maximum velocity appeared proximal to the focus–and 0 mm laterally.

5.3.3 *Comprehensive Doppler Metric Analysis in Kidney*

The histological image, liquefaction grades, and five Doppler metrics associated with a representative BH exposure in the kidney are shown in Fig. 5.7 in the same format as seen in Fig. 5.6. In this particular case, gated BH pulse protocol was implemented to mitigate the effects of the pig's respiration. The treated lesion was primarily in the medulla with a small portion extending

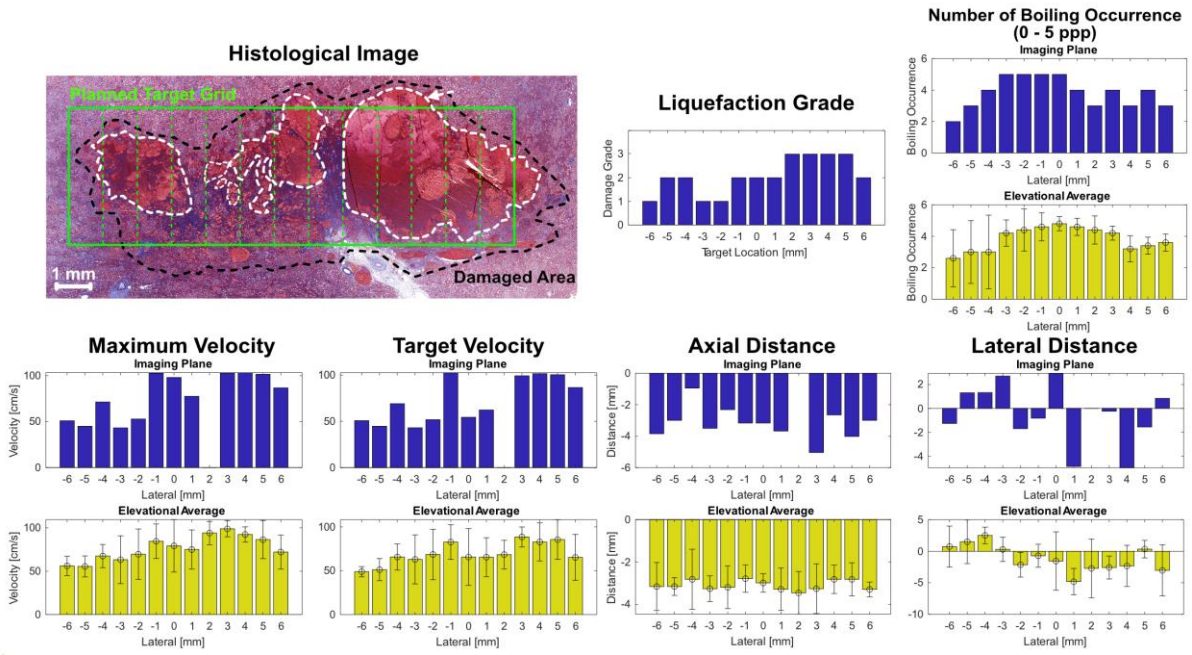

Figure 5.7. Representative example of a correlation between Doppler-based metrics with histological analysis in kidney; the planned target grid is marked in green. The liquefaction grade and five metrics measured at both imaging plane (blue) and elevational average (yellow) are displayed using bar graph, showing the spatial distribution of those metrics within planned target grid. Error bars represent standard deviation.

into the cortex on the right side of the lesion. It has been reported that the medulla has resistance to BH treatment in contrast to the cortex, which is more susceptible to breakdown. This tissue-specific response and gated pulse protocol led to a more confined lesion with several smaller areas of liquefaction within the planned target area rather than a single, extensive area.

In terms of the liquefaction quality, a 4 mm long area on the right side of the lesion reached a grade 3 level of liquefaction. On the left side of the lesion, the maximum axial length of liquefaction was approximately 2 mm, which was evaluated as a grade 1 or 2. Unlike the liver case, the number of boiling occurrences was not highly aligned with the liquefaction grade: there were some target points where 100% boiling occurred but grade 2 and grade 3 area achieved 60 – 80% boiling occurrences. This was likely due to inhomogeneity between medulla and cortex and tissue-specific response of BH treatment in kidney. Next, the maximum and target velocity showed an

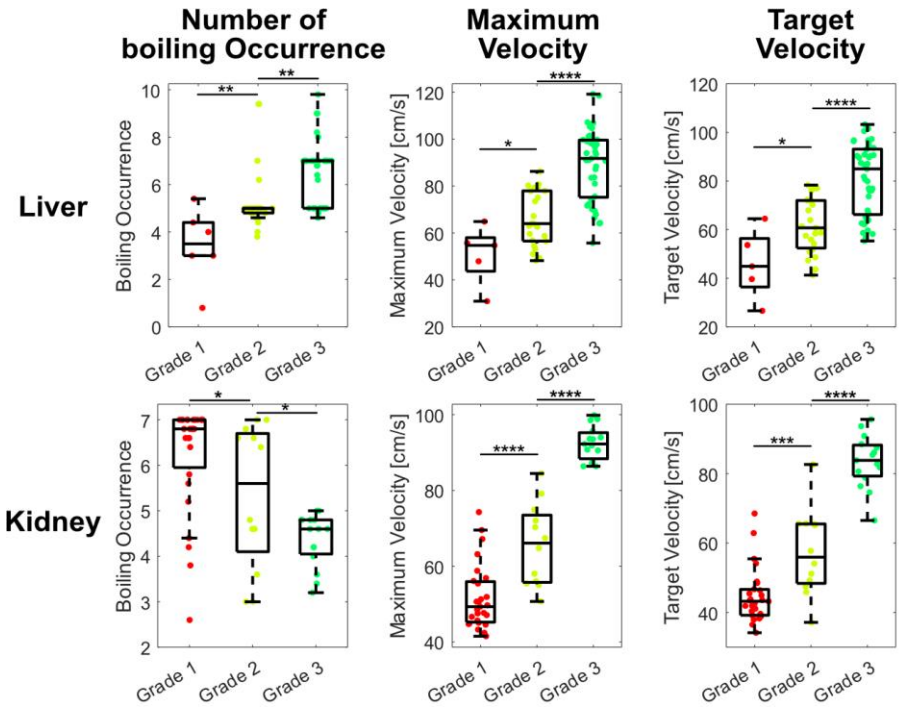

Figure 5.8. Comparison between liquefaction grades and Doppler metrics (number of boiling occurrences, maximum, and target velocity) in both liver and kidney. Each data point denoted the colored dots, and the box graphs display median value, upper and lower quantiles, and extremes. In box graphs, the whiskers of 1.5 was used. The two-sample t-test between datasets of subsequent grade levels was performed and statistical significance is indicated by asterisks (*: $p < 0.05$, **: $p < 0.01$, ***: $p < 0.001$, and ****: $p < 0.0001$).

expected dependence on the liquefaction grade particularly for the elevational averaged metrics. The elevational averaged maximum velocity for grades 3 and 2 ranged from 86.4 to 98.8 cm/s and from 55.5 to 84.5 cm/s, respectively. Lastly, the axial and lateral distance shows similar results as the liver, which did not align with the liquefaction grade.

5.3.4 *Comparison between Doppler Metrics and Tissue Liquefactions*

Fig. 5.8 presents box graph comparisons across three grades of liquefaction for both liver and kidney tissues, showing the correlations between liquefaction grades and three elevational averaged metrics–the number of boiling occurrences, v_{max}, and v_{target}–based on all of the BH exposures listed in Table 5.1. Here, each colored dot indicates the data point for the lateral

locations of the targets. For the liver, the sample sizes were n=6, 23, and 41 for grade 1, 2, and 3, respectively. For the kidney, the sample sizes were n=27, 12, and 15 for grade 1, 2, and 3, respectively. The asterisks indicate the statistical significance of differences between the grades, determined by t-test results as mentioned in method.

In the liver, the number of boiling occurrences increases with higher liquefaction grades, with grade 3 showing the most occurrences. This observation does not hold for the kidney, where grade 3 displays fewer boiling occurrences than observed in grade 1 and 2. It is worth noting that this metric may be influenced by variations in the PPP of the BH exposures across different treatments. Notably, the most extensive tissue damage characterized by uniform liquefaction throughout the kidney's target grid was achieved with a treatment of 5 PPP in the cortical area. In contrast, the most limited liquefaction occurred with a treatment of 7 PPP in the sinus and medullary area of the kidney.

Both v_{max} and v_{target} in the liver exhibit a statistically significant increase from grade 1 to grade 3 particularly with p-value between grade 2 and 3 of $2.88e^{-8}$ (for v_{max})and $7.67e^{-7}$ (for v_{target}), respectively, confirming that higher velocities are associated with more complete liquefaction. This observation also aligned with the kidney results, with p-value between grade 2 and 3 of $4.39e^{-9}$ (for v_{max})and $3.64e^{-7}$ (for v_{target}).

5.4 Discussion and Conclusion

In this study, color Doppler imaging was applied to monitor volumetric BH treatments within the liver and kidney tissues in *in vivo* pigs. The Doppler velocity maps accurately represented the treatment lesions with a good alignment with the observed dimensions. Specifically, the area of motion detected in the Doppler velocity maps (Fig. 5.5) corresponded closely with the surface

bruise visible in the photograph (Fig. 5.5) and the corresponding histological image (Fig. 5.6). This demonstrates the effectiveness of using Doppler imaging superimposed with B-mode for visually monitoring the BH-induced lesions. Further, the Doppler velocity map can be employed for the identification of BH pulses that did not induce boiling (Fig. 5.3(b)) and induced cavitation activity within blood vessels and biliary or urinary structures that were characterized by twinkling artifact (Fig. 5.3(c)). Although manual selection of the boiling cases was performed in this study, it is feasible to develop algorithms for automatic selection in future studies. For instance, using a threshold based on significantly lower Doppler power observed in non-boiling cases could automate this process. Similarly, the unique pattern of random changes in velocity sign associated with twinkling artifacts could be algorithmically detected and filtered.

Among the Doppler-based metrics analyzed, the maximum velocity (v_{max}) captured immediately following the BH pulses exhibited the best performance, showing a strong correlation with the degrees of liquefaction determined by histological assessments. This metric proved to be a reliable indicator for identifying grade 3 tissue liquefaction, which reflects the desired endpoint for BH treatment. Notably, an elevational averaged v_{max} exceeding 80 cm/s was indicative of grade 3 liquefaction with a confidence level >91% for liver and >96% for kidney, suggesting its potential as a robust and predictive metric for BH treatment. The target velocity (v_{target}) also proved to be a valuable candidate metric, providing correlation results nearly comparable to those of v_{max}, but would have an advantage in terms of reduced processing time due to a smaller ROI to be processed.

In both velocity metrics–v_{max} and v_{target}, the correlations observed in the kidney tissue slightly outperformed those in the liver. However, the number of boiling occurrences that showed reasonable correlation in liver did not correlate as strongly in kidney tissues. This discrepancy may

be attributed to the unique structural characteristics of the kidney. Specifically, the medulla and sinus areas in kidney are known for their resistance to mechanical fractionation, even when boiling occurs, which contrasts sharply with the cortex where tissue breakdown is more readily achieved. Given the tissue-specific variability in response to BH treatments, the boiling occurrence does not influence the correlation as much as it does for liver.

Overall, the finding from this *in vivo* study aligned with our previous experiments on *ex vivo* bovine myocardium tissue [68]. The maximum velocity increases in bubble motion during lesion progression observed by Doppler velocity maps were consistent across both *ex vivo* and *in vivo* settings. However, a difference was observed: v_{max} at the initial BH pulse was higher in *in vivo* tissue, around 40 cm/s, compared to 20 – 30 cm/s observed in *ex vivo* tissues. While these differences might simply reflect variations between tissue types, they may also indicate a high efficiency of liquefaction *in vivo*, supporting our anecdotal evidence that fewer BH pulses may achieve comparable liquefaction quality *in vivo* compared to more BH pulse numbers required *ex vivo*.

Several factors could have confounded the results of this study. First, the tissue samples may have undergone non-uniform and anisotropic shrinkage during the fixation process, potentially leading to an underestimation of the liquefied areas. Second, the selected BH exposures were performed with a single BH pulsing parameter set (i.e. 10 ms with 1 Hz PRF). Since the shorter but more intense BH pulses might induce different levels of ARF at the focus, the velocities of the residual bubbles may be altered, which requires future investigations. Additionally, only one sample from each tissue type was treated using multiple layers of target grid to generate an axially larger liquefied volume. Prior observations from *ex vivo* tissue suggested that the maximum velocity (v_{max}) may not be effective in larger volumes, as the maximum velocities may occur in

volumes previously treated and positioned distally, rather than in the currently treated volume. This makes it non-representative of the liquefaction level in current treatment volume. Considering treatments over larger volumes, the target velocity (v_{target}) could be a more universally applicable metric for any size of the BH treatment volume.

Chapter 6.
CONCLUSIONS

6.1 SUMMARY

This dissertation presents the Doppler-based cavitation monitoring methods for pHIFU and BH regimes. The proposed techniques provide not only imaging of the cavitation to pinpoint the treatment location and visually track the progression, but also physically meaningful quantitative metrics (i.e. bubble dissolution rate and velocity of bubble's translational motion) that correlated to the tissue damage or liquefaction levels. The summary of this work is described as follows.

In Chapter 2, dynamic mode decomposition (DMD) was introduced to separate fast-dissolving cavitation bubble images, induced by pulsed HIFU regime, from the tissue's stationary or acoustic radiation force (ARF) displaced clutter motions. With this capability, this technique can be used for Doppler clutter filter. *In silico* performance comparison was conducted with widely used Doppler filters such as infinite impulse response (IIR) high pass filter and singular value decomposition (SVD) filter. The results suggested that DMD outperforms IIR high pass and SVD in decomposition of cavitation bubbles with high accuracy (< 0.6% error). The experimental results conducted on *ex vivo* bovine tongue tissue showed effective cavitation decomposition with high contrast at HIFU focus. Furthermore, the observed decaying rate, a quantitative metric derived from DMD, indicative of the bubble dissolving rate, showed diminishing trends as the treatment progressed. This trend is physically reasonable, as the loss of tissue structures provides more space for the bubbles to persist longer.

In Chapter 3, DMD-enhanced Doppler monitoring was applied to the *in vivo* surgically exposed liver of a pig. The study introduced a fully automated bubble mode identification

technique, utilizing k-means clustering alongside an image contrast-based algorithm. This approach led to the generation of DMD-filtered bubble images and corresponding Doppler power maps following each HIFU pulse. These Doppler power maps were then analyzed in relation to the extent of tissue damage, as determined by histological analysis. The findings indicate that the DMD-enhanced Doppler power maps can effectively visualize bubble distribution with high contrast, and that the levels of Doppler power are indicative of the tissue damage level by cavitation. Moreover, the temporal characteristics of the bubble modes (*i.e.* decay rate derived from DMD) provide information of the bubble dissolution rate, which correlates with tissue damage level; for instance, slower rates are indicative of more severe tissue damage.

In Chapter 4, the translational velocity of residual bubble induced by boiling histotripsy (BH) pulses was measured using the color Doppler method. To track these swiftly moving bubbles and mitigate the aliasing artifacts, a high PRF technique was implemented. This technique involved gating the imaging pulses to effectively double the measurement velocity limits. For lesions axially smaller than HIFU focal area, the maximum velocity following the BH pulse was directed toward the HIFU transducer and increased monotonically from approximately 20 – 100 cm/s as liquefaction progressed, then saturated once tissue was fully liquefied. In cases of larger lesions formed by merging multiple smaller lesions axially, a high-speed streaming away from the HIFU transducer was observed at the point of complete liquefaction. These findings led to the proposal and evaluation of maximum directional velocity and its location along the HIFU propagation axis as potential metrics for assessing the endpoint of BH treatment.

In Chapter 5, the effectiveness of the proposed metric was tested *in vivo* using porcine abdominal tissues, specifically liver and kidney, and was correlated with the extent of tissue liquefaction evaluated histologically. The results indicated that the metrics derived from the

Doppler velocity maps, particularly maximum velocity, and target velocity, offer a strong predictive value for assessing tissue liquefaction level, as aligned with expectations based on the *ex vivo* experiment discussed in Chapter 4. Notably, an elevational averaged maximum velocity exceeding 80 cm/s was found to be indicative of complete liquefaction, with a confidence level greater than 91% for liver and over 96% for kidney. These findings suggest the potential of these metrics as a robust and predictive indicator for BH treatment.

In a nutshell, the techniques proposed in this study are both effective and innovative, offering advancement to address the existing limitations in cavitation monitoring for pHIFU and BH treatment. Here are the key contributions of this research.

1. The study developed a new method for imaging rapidly dissolving cavitation bubbles following HIFU pulses and for measuring the dissolution time using reduced-order spatiotemporal analysis, referred to as dynamic mode decomposition (DMD).
2. The study investigated the progression of lesion formation for boiling histotripsy (BH) treatment using color Doppler with high PRF measurement techniques to track swiftly moving cavitation bubbles within the liquefied lesion.
3. The study suggested quantitative metrics for both pHIFU and BH regimes, which correlated with the degree of tissue damage or liquefaction as evaluated histologically, serving as indicators for determining the completion point of treatments, thereby enhancing both the efficiency and safety of the procedures.

6.2 FUTURE WORKS

While the Doppler-based techniques proposed in this study have demonstrated potential in monitoring cavitation bubble during HIFU treatments, further research is needed to enhance their clinical applicability. To begin with, the proposed technique should be tested across the more

various types of *in vivo* tissues to explore how different tissue material properties might influence outcomes. In pHIFU regime, where the cavitation bubbles are spatially stationary but dissolve quickly, the stiffness of the tissue may affect the dissolving rate, which stiffer tissues likely leading to faster dissolution rates. Conversely, in BH regimes, where cavitation bubbles move swiftly within the liquefied tissue, it is known that stiffness could influence the size of the lesion and the number of pulses required for complete liquefaction. However, the relation between Doppler velocity and the size of the liquefaction volume is likely to show limited variability across different tissues, particularly for the larger treatment tissue volumes, as evidenced by similar results observed in both liver and kidney in this study.

Furthermore, in this study, Doppler processing was performed offline, with computation times for data related to a single HIFU pulse within a few hundred milliseconds for both pHIFU and BH regimes, demonstrating feasibility for real-time implementation. Moving forward, actual real-time implementation and demonstration of controlling tissue damage or liquefaction based on the proposed metrics are required.

Figure 6.1 illustrates the provisional real-time feedback for practical usage in both pHIFU and BH treatments. In pHIFU, the feedback screen would display a real-time Doppler power map related to the current HIFU pulse to monitor cavitation in the targeted area. Additionally, the feedback would show a damage estimation area on the B-mode image with area calculations for each grade, based on the Doppler power level. The decay rate of bubble modes would be tracked and displayed throughout the treatment, guided by the estimated maximum tissue damage level based on the findings in this research.

Similarly, in BH, the feedback screen would include a current Doppler velocity map, and the proposed metrics, including maximum velocity, would be tracked with a target value guiding

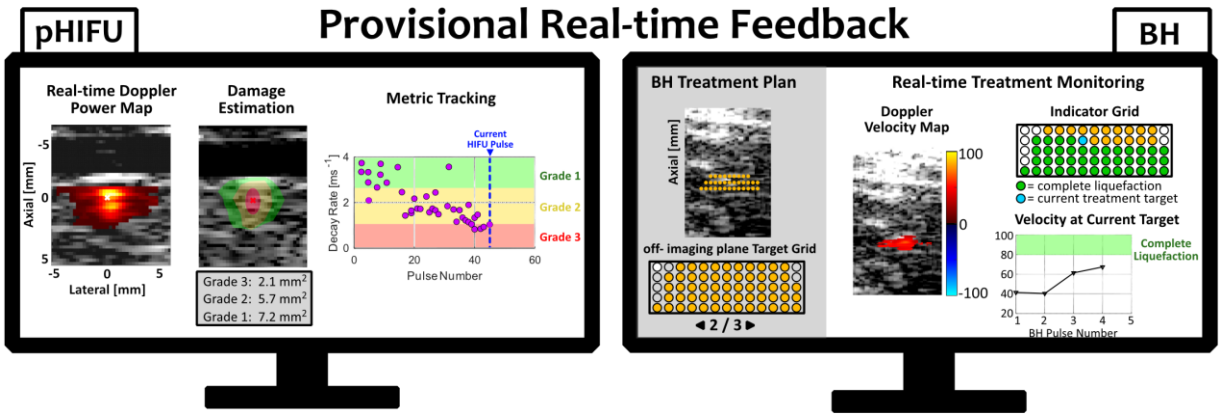

Figure 6.1. Provisional real-time feedback screen in pHIFU (left) and BH (right).

complete liquefaction. Furthermore, because BH generally uses multiple targets on a planned grid to generate large volume lesions, an auxiliary planning screen for target placement on both imaging plane and off-imaging planes can be realized. An indicator grid showing the treatment status for each target point would also be displayed.

Several intriguing topics for future research could be explored based on these studies, particularly regarding the application of DMD. One promising area involves using DMD to characterize stable cavitation activity from microbubbles. Unlike the fast-dissolving bubbles, where signal decay predominates, the backscattered signal from stable cavitation conveys the dynamics of bubble oscillations, which could be modeled by nonlinear differential equations such as the Rayleigh-Plesset equation. While my study used the basic version of DMD, which assumes that the underlying physics of the data follows linear differential equations, an advanced version of DMD, integrated with Koopman theory, can account for the nonlinearity coming from bubble dynamics. This enables the analysis of stable cavitation activity, which could enhance both imaging and therapeutic applications that utilize stable cavitation of the microbubbles. Additionally, DMD is anticipated to be beneficial in vascular imaging and flow pattern analysis within large veins and arteries, where turbulence blood flow is often observed. DMD has the potential to decompose the coherent structures within these complex blood flows and quantify

their characteristics. This capability could lead to more accurate assessments of vascular health and dynamics of blood circulation.

BIBLIOGRAPHY

[1] W. J. Fry, W. H. Mosberg, J. W. Barnard, and F. J. Fry, “Production of focal destructive lesions in the central nervous system with ultrasound,” *J. Neurosurg.*, vol. 11, no. 5, pp. 471–478, 1954.

[2] G. Ter Haar and C. Coussios, “High Intensity Focused Ultrasound: Past, present and future,” *Int. J. Hyperthermia*, vol. 23, no. 2, pp. 85–87, Jan. 2007, doi: 10.1080/02656730601185924.

[3] M. R. Bailey, V. A. Khokhlova, O. A. Sapozhnikov, S. G. Kargl, and L. A. Crum, “Physical mechanisms of the therapeutic effect of ultrasound (a review),” *Acoust. Phys.*, vol. 49, no. 4, pp. 369–388, Jul. 2003, doi: 10.1134/1.1591291.

[4] V. A. Khokhlova *et al.*, “Histotripsy methods in mechanical disintegration of tissue: Towards clinical applications,” *Int. J. Hyperthermia*, vol. 31, no. 2, pp. 145–162, Feb. 2015, doi: 10.3109/02656736.2015.1007538.

[5] J.-F. Aubry *et al.*, “The road to clinical use of high-intensity focused ultrasound for liver cancer: technical and clinical consensus,” *J. Ther. Ultrasound*, vol. 1, no. 1, p. 13, Dec. 2013, doi: 10.1186/2050-5736-1-13.

[6] S. Vaezy, M. Andrew, P. Kaczkowski, and L. Crum, “Image-Guided Acoustic Therapy,” *Annu. Rev. Biomed. Eng.*, vol. 3, no. Volume 3, 2001, pp. 375–390, Aug. 2001, doi: 10.1146/annurev.bioeng.3.1.375.

[7] R. Geoghegan, G. ter Haar, K. Nightingale, L. Marks, and S. Natarajan, “Methods of monitoring thermal ablation of soft tissue tumors – A comprehensive review,” *Med. Phys.*, vol. 49, no. 2, pp. 769–791, 2022, doi: 10.1002/mp.15439.

[8] L. A. Crum, “Measurements of the growth of air bubbles by rectified diffusion,” *J. Acoust. Soc. Am.*, vol. 68, no. 1, pp. 203–211, Jul. 1980, doi: 10.1121/1.384624.

[9] T. Li *et al.*, “Pulsed High-Intensity Focused Ultrasound Enhances Delivery of Doxorubicin in a Preclinical Model of Pancreatic Cancer,” *Cancer Res.*, vol. 75, no. 18, pp. 3738–3746, Sep. 2015, doi: 10.1158/0008-5472.CAN-15-0296.

[10] Y. Zhou *et al.*, “Enhancement of Small Molecule Delivery by Pulsed High-Intensity Focused Ultrasound: A Parameter Exploration,” *Ultrasound Med. Biol.*, vol. 42, no. 4, pp. 956–963, Apr. 2016, doi: 10.1016/j.ultrasmedbio.2015.12.009.

[11] E. S. Lee *et al.*, “Pulsed High-Intensity Focused Ultrasound Enhances Apoptosis of Pancreatic Cancer Xenograft with Gemcitabine,” *Ultrasound Med. Biol.*, vol. 39, no. 11, pp. 1991–2000, Nov. 2013, doi: 10.1016/j.ultrasmedbio.2013.06.004.

[12] T. D. Khokhlova, Y.-N. Wang, H. Son, S. Totten, S. Whang, and J. Ha Hwang, “Chronic effects of pulsed high intensity focused ultrasound aided delivery of gemcitabine in a mouse model of pancreatic cancer,” *Ultrasonics*, vol. 132, p. 106993, Jul. 2023, doi: 10.1016/j.ultras.2023.106993.

[13] J. Y. Lee *et al.*, “Combination of chemotherapy and focused ultrasound for the treatment of unresectable pancreatic cancer: a proof-of-concept study,” *Eur. Radiol.*, vol. 33, no. 4, pp. 2620–2628, Apr. 2023, doi: 10.1007/s00330-022-09271-8.

[14] S. R. Burks *et al.*, “Investigation of Cellular and Molecular Responses to Pulsed Focused Ultrasound in a Mouse Model,” *PLOS ONE*, vol. 6, no. 9, p. e24730, Sep. 2011, doi: 10.1371/journal.pone.0024730.

[15] R. M. Lorsung, R. B. Rosenblatt, G. Cohen, J. A. Frank, and S. R. Burks, “Acoustic Radiation or Cavitation Forces From Therapeutic Ultrasound Generate Prostaglandins and Increase Mesenchymal Stromal Cell Homing to Murine Muscle,” *Front. Bioeng. Biotechnol.*, vol. 8, 2020, Accessed: Nov. 07, 2023. [Online]. Available: https://www.frontiersin.org/articles/10.3389/fbioe.2020.00870

[16] A. D. Maxwell *et al.*, “Cavitation clouds created by shock scattering from bubbles during histotripsy,” *J. Acoust. Soc. Am.*, vol. 130, no. 4, pp. 1888–1898, Oct. 2011, doi: 10.1121/1.3625239.

[17] Z. Xu, T. D. Khokhlova, C. S. Cho, and V. A. Khokhlova, “Histotripsy: A Method for Mechanical Tissue Ablation with Ultrasound,” *Annu. Rev. Biomed. Eng.*, vol. 26, no. 1, p. null, 2024, doi: 10.1146/annurev-bioeng-073123-022334.

[18] E. Vlaisavljevich, A. Maxwell, L. Mancia, E. Johnsen, C. Cain, and Z. Xu, “Visualizing the histotripsy process: Bubble cloud–cancer cell interactions in a tissue-mimicking environment,” *Ultrasound Med. Biol.*, vol. 42, no. 10, pp. 2466–2477, 2016.

[19] A. D. Maxwell, C. A. Cain, T. L. Hall, J. B. Fowlkes, and Z. Xu, “Probability of cavitation for single ultrasound pulses applied to tissues and tissue-mimicking materials,” *Ultrasound Med. Biol.*, vol. 39, no. 3, pp. 449–465, 2013.

[20] M. F. Hamilton, D. T. Blackstock, and L. A. Ostrovsky, “Nonlinear acoustics,” *J. Acoust. Soc. Am.*, vol. 105, no. 2, pp. 578–578, 1999.

[21] M. S. Canney, V. A. Khokhlova, O. V. Bessonova, M. R. Bailey, and L. A. Crum, “Shock-Induced Heating and Millisecond Boiling in Gels and Tissue Due to High Intensity Focused Ultrasound,” *Ultrasound Med. Biol.*, vol. 36, no. 2, pp. 250–267, Feb. 2010, doi: 10.1016/j.ultrasmedbio.2009.09.010.

[22] J. C. Simon, O. A. Sapozhnikov, V. A. Khokhlova, Y.-N. Wang, L. A. Crum, and M. R. Bailey, “Ultrasonic atomization of tissue and its role in tissue fractionation by high intensity focused ultrasound,” *Phys. Med. Biol.*, vol. 57, no. 23, p. 8061, 2012.

[23] J. C. Simon, O. A. Sapozhnikov, Y.-N. Wang, V. A. Khokhlova, L. A. Crum, and M. R. Bailey, “Investigation into the Mechanisms of Tissue Atomization by High-Intensity Focused Ultrasound,” *Ultrasound Med. Biol.*, vol. 41, no. 5, pp. 1372–1385, May 2015, doi: 10.1016/j.ultrasmedbio.2014.12.022.

[24] K. J. Pahk, M. O. de Andrade, P. Gélat, H. Kim, and N. Saffari, “Mechanical damage induced by the appearance of rectified bubble growth in a viscoelastic medium during boiling histotripsy exposure,” *Ultrason. Sonochem.*, vol. 53, pp. 164–177, May 2019, doi: 10.1016/j.ultsonch.2019.01.001.

[25] K. J. Pahk, S. Lee, P. Gélat, M. O. de Andrade, and N. Saffari, “The interaction of shockwaves with a vapour bubble in boiling histotripsy: The shock scattering effect,” *Ultrason. Sonochem.*, vol. 70, p. 105312, Jan. 2021, doi: 10.1016/j.ultsonch.2020.105312.

[26] T. D. Khokhlova *et al.*, “Pilot in vivo studies on transcutaneous boiling histotripsy in porcine liver and kidney,” *Sci. Rep.*, vol. 9, no. 1, pp. 1–12, 2019.

[27] T. D. Khokhlova *et al.*, “Ultrasound-guided tissue fractionation by high intensity focused ultrasound in an in vivo porcine liver model,” *Proc. Natl. Acad. Sci.*, vol. 111, no. 22, pp. 8161–8166, Jun. 2014, doi: 10.1073/pnas.1318355111.

[28] E. Ponomarchuk *et al.*, “Histology-based quantification of boiling histotripsy outcomes via ResNet-18 network: Towards mechanical dose metrics,” *Ultrasonics*, vol. 138, p. 107225, Mar. 2024, doi: 10.1016/j.ultras.2023.107225.

[29] T. J. Dubinsky, T. D. Khokhlova, V. Khokhlova, and G. R. Schade, “Histotripsy: The Next Generation of High-Intensity Focused Ultrasound for Focal Prostate Cancer Therapy,” *J. Ultrasound Med.*, vol. 39, no. 6, pp. 1057–1067, Jun. 2020, doi: 10.1002/jum.15191.

[30] G. R. Schade, Y.-N. Wang, S. D'Andrea, J. H. Hwang, W. C. Liles, and T. D. Khokhlova, "Boiling Histotripsy Ablation of Renal Cell Carcinoma in the Eker Rat Promotes a Systemic Inflammatory Response," *Ultrasound Med. Biol.*, vol. 45, no. 1, pp. 137–147, Jan. 2019, doi: 10.1016/j.ultrasmedbio.2018.09.006.

[31] V. A. Khokhlova *et al.*, "Initial Assessment of Boiling Histotripsy for Mechanical Ablation of Ex Vivo Human Prostate Tissue," *Ultrasound Med. Biol.*, p. S0301562922005075, Oct. 2022, doi: 10.1016/j.ultrasmedbio.2022.07.014.

[32] P. B. Rosnitskiy *et al.*, "Pilot ex vivo study on non-thermal ablation of human prostate adenocarcinoma tissue using boiling histotripsy," *Ultrasonics*, vol. 133, p. 107029, Aug. 2023, doi: 10.1016/j.ultras.2023.107029.

[33] T. D. Khokhlova, W. L. Monsky, Y. A. Haider, A. D. Maxwell, Y.-N. Wang, and T. J. Matula, "Histotripsy Liquefaction of Large Hematomas," *Ultrasound Med. Biol.*, vol. 42, no. 7, pp. 1491–1498, Jul. 2016, doi: 10.1016/j.ultrasmedbio.2016.01.020.

[34] T. J. Matula *et al.*, "Treating Porcine Abscesses with Histotripsy: A Pilot Study," *Ultrasound Med. Biol.*, vol. 47, no. 3, pp. 603–619, Mar. 2021, doi: 10.1016/j.ultrasmedbio.2020.10.011.

[35] P. A. Ambekar *et al.*, "Comparative Study of Histotripsy Pulse Parameters Used to Inactivate Escherichia coli in Suspension," *Ultrasound Med. Biol.*, vol. 49, no. 12, pp. 2451–2458, 2023.

[36] G. Nam *et al.*, "Investigation of the Potential Immunological Effects of Boiling Histotripsy for Cancer Treatment," *Adv. Ther.*, vol. 3, no. 8, p. 1900214, Aug. 2020, doi: 10.1002/adtp.201900214.

[37] M. P. Singh, S. N. Sethuraman, C. Miller, J. Malayer, and A. Ranjan, "Boiling histotripsy and in-situ CD40 stimulation improve the checkpoint blockade therapy of poorly immunogenic tumors," *Theranostics*, vol. 11, no. 2, p. 540, 2021.

[38] > CC Coussios, C. H. Farny, G. Ter Haar, and R. A. Roy, "Role of acoustic cavitation in the delivery and monitoring of cancer treatment by high-intensity focused ultrasound (HIFU)," *Int. J. Hyperthermia*, vol. 23, no. 2, pp. 105–120, 2007.

[39] T. Leighton, *The acoustic bubble*. Academic press, 2012. Accessed: Apr. 30, 2024. [Online]. Available: https://books.google.com/books?hl=en&lr=&id=tR-

8SNimBuEC&oi=fnd&pg=PP1&dq=acoustic+bubble&ots=gZyruwZgLp&sig=MBUUSWzLF4mR060XHy-oBCCFUnk

[40] C. R. Jensen, R. O. Cleveland, and C. C. Coussios, “Real-time temperature estimation and monitoring of HIFU ablation through a combined modeling and passive acoustic mapping approach*,” *Phys. Med. Biol.*, vol. 58, no. 17, p. 5833, Aug. 2013, doi: 10.1088/0031-9155/58/17/5833.

[41] C. Coviello *et al.*, “Passive acoustic mapping utilizing optimal beamforming in ultrasound therapy monitoring,” *J. Acoust. Soc. Am.*, vol. 137, no. 5, pp. 2573–2585, May 2015, doi: 10.1121/1.4916694.

[42] V. A. Salgaonkar, S. Datta, C. K. Holland, and T. D. Mast, “Passive cavitation imaging with ultrasound arrays,” *J. Acoust. Soc. Am.*, vol. 126, no. 6, pp. 3071–3083, 2009.

[43] K. J. Haworth, K. B. Bader, K. T. Rich, C. K. Holland, and T. D. Mast, “Quantitative Frequency-Domain Passive Cavitation Imaging,” *IEEE Trans. Ultrason. Ferroelectr. Freq. Control*, vol. 64, no. 1, pp. 177–191, Jan. 2017, doi: 10.1109/TUFFC.2016.2620492.

[44] N. S. Anavekar and J. K. Oh, “Doppler echocardiography: a contemporary review,” *J. Cardiol.*, vol. 54, no. 3, pp. 347–358, 2009.

[45] C. Kasai, K. Namekawa, A. Koyano, and R. Omoto, “Real-time two-dimensional blood flow imaging using an autocorrelation technique,” *IEEE Trans. Sonics Ultrason.*, vol. 32, no. 3, pp. 458–464, 1985.

[46] T. Li, T. D. Khokhlova, O. A. Sapozhnikov, M. O’Donnell, and J. H. Hwang, “A new active cavitation mapping technique for pulsed HIFU applications-bubble doppler,” *IEEE Trans. Ultrason. Ferroelectr. Freq. Control*, vol. 61, no. 10, pp. 1698–1708, Oct. 2014, doi: 10.1109/TUFFC.2014.006502.

[47] R. M. Miller, X. Zhang, A. D. Maxwell, C. A. Cain, and Z. Xu, “Bubble-Induced Color Doppler Feedback for Histotripsy Tissue Fractionation,” *IEEE Trans. Ultrason. Ferroelectr. Freq. Control*, vol. 63, no. 3, pp. 408–419, Mar. 2016, doi: 10.1109/TUFFC.2016.2525859.

[48] T. Li *et al.*, “Passive Cavitation Detection during Pulsed HIFU Exposures of Ex Vivo Tissues and In Vivo Mouse Pancreatic Tumors,” *Ultrasound Med. Biol.*, vol. 40, no. 7, pp. 1523–1534, Jul. 2014, doi: 10.1016/j.ultrasmedbio.2014.01.007.

[49] R. P. Williams *et al.*, “Dual-Mode 1D Linear Ultrasound Array for Image-Guided Drug Delivery Enhancement Without Ultrasound Contrast Agents,” *IEEE Trans. Ultrason. Ferroelectr. Freq. Control*, pp. 1–1, 2023, doi: 10.1109/TUFFC.2023.3268603.

[50] J. R. Chevillet *et al.*, “Release of Cell-free MicroRNA Tumor Biomarkers into the Blood Circulation with Pulsed Focused Ultrasound: A Noninvasive, Anatomically Localized, Molecular Liquid Biopsy,” *Radiology*, vol. 283, no. 1, pp. 158–167, Apr. 2017, doi: 10.1148/radiol.2016160024.

[51] T. G. Landry *et al.*, “Endoscopic Coregistered Ultrasound Imaging and Precision Histotripsy: Initial In Vivo Evaluation,” *BME Front.*, vol. 2022, p. 9794321, Jul. 2022, doi: 10.34133/2022/9794321.

[52] B. Arnal, J. Baranger, C. Demene, M. Tanter, and M. Pernot, “In vivo real-time cavitation imaging in moving organs,” *Phys. Med. Biol.*, vol. 62, no. 3, p. 843, 2017.

[53] J. Baranger, B. Arnal, F. Perren, O. Baud, M. Tanter, and C. Demené, “Adaptive Spatiotemporal SVD Clutter Filtering for Ultrafast Doppler Imaging Using Similarity of Spatial Singular Vectors,” *IEEE Trans. Med. Imaging*, vol. 37, no. 7, pp. 1574–1586, Jul. 2018, doi: 10.1109/TMI.2018.2789499.

[54] A. C. H. Yu and L. Lovstakken, “Eigen-based clutter filter design for ultrasound color flow imaging: a review,” *IEEE Trans. Ultrason. Ferroelectr. Freq. Control*, vol. 57, no. 5, pp. 1096–1111, May 2010, doi: 10.1109/TUFFC.2010.1521.

[55] J. N. Kutz, S. L. Brunton, B. W. Brunton, and J. L. Proctor, *Dynamic mode decomposition: data-driven modeling of complex systems*. SIAM, 2016.

[56] P. J. Schmid, “Dynamic mode decomposition of numerical and experimental data,” *J. Fluid Mech.*, vol. 656, pp. 5–28, 2010.

[57] K. Taira *et al.*, “Modal analysis of fluid flows: An overview,” *Aiaa J.*, vol. 55, no. 12, pp. 4013–4041, 2017.

[58] E. Berger, M. Sastuba, D. Vogt, B. Jung, and H. Ben Amor, “Estimation of perturbations in robotic behavior using dynamic mode decomposition,” *Adv. Robot.*, vol. 29, no. 5, pp. 331–343, 2015.

[59] C. Bi, Y. Yuan, R. Zhang, Y. Xiang, Y. Wang, and J. Zhang, “A Dynamic Mode Decomposition Based Edge Detection Method for Art Images,” *IEEE Photonics J.*, vol. 9, no. 6, pp. 1–13, Dec. 2017, doi: 10.1109/JPHOT.2017.2766881.

[60] B. W. Brunton, L. A. Johnson, J. G. Ojemann, and J. N. Kutz, “Extracting spatial–temporal coherent patterns in large-scale neural recordings using dynamic mode decomposition,” *J. Neurosci. Methods*, vol. 258, pp. 1–15, Jan. 2016, doi: 10.1016/j.jneumeth.2015.10.010.

[61] A. A. Kaptanoglu, K. D. Morgan, C. J. Hansen, and S. L. Brunton, “Characterizing magnetized plasmas with dynamic mode decomposition,” *Phys. Plasmas*, vol. 27, no. 3, p. 032108, 2020.

[62] J. Mann and J. N. Kutz, “Dynamic mode decomposition for financial trading strategies,” *Quant. Finance*, vol. 16, no. 11, pp. 1643–1655, 2016.

[63] A. D. Maxwell *et al.*, “A Prototype Therapy System for Transcutaneous Application of Boiling Histotripsy,” *IEEE Trans. Ultrason. Ferroelectr. Freq. Control*, vol. 64, no. 10, pp. 1542–1557, Oct. 2017, doi: 10.1109/TUFFC.2017.2739649.

[64] C. R. Bawiec *et al.*, “Inertial Cavitation Behaviors Induced by Nonlinear Focused Ultrasound Pulses,” *IEEE Trans. Ultrason. Ferroelectr. Freq. Control*, vol. 68, no. 9, pp. 2884–2895, Sep. 2021, doi: 10.1109/TUFFC.2021.3073347.

[65] O. V. Bessonova, V. A. Khokhlova, M. S. Canney, M. R. Bailey, and L. A. Crum, “A derating method for therapeutic applications of high intensity focused ultrasound,” *Acoust. Phys.*, vol. 56, no. 3, pp. 354–363, May 2010, doi: 10.1134/S1063771010030140.

[66] P. A. Hasgall *et al.*, “IT’IS Database for thermal and electromagnetic parameters of biological tissues.” Feb. 22, 2022. doi: 10.13099/VIP21000-04-1.

[67] J. H. Tu, “Dynamic mode decomposition: Theory and applications,” PhD Thesis, Princeton University, 2013.

[68] M. Song *et al.*, “Quantitative Assessment of Boiling Histotripsy Progression Based on Color Doppler Measurements,” *IEEE Trans. Ultrason. Ferroelectr. Freq. Control*, vol. 69, no. 12, pp. 3255–3269, Dec. 2022, doi: 10.1109/TUFFC.2022.3212266.

[69] M. Song, O. A. Sapozhnikov, V. A. Khokhlova, and T. D. Khokhlova, “Dynamic Mode Decomposition for Transient Cavitation Bubbles Imaging in Pulsed High Intensity Focused Ultrasound Therapy,” *bioRxiv*, pp. 2024–02, 2024.

[70] A. Rose, *Vision: human and electronic*. Springer Science & Business Media, 2013. Accessed: Jan. 23, 2024. [Online]. Available: https://books.google.com/books?hl=en&lr=&id=m47kBwAAQBAJ&oi=fnd&pg=PR15&d

q=vision+human+and+electronic&ots=T2j9VBMVZ3&sig=O-F3bl8B_9ywnictpFNuzdRcZSA

[71] S. L. Brunton and J. N. Kutz, *Data-driven science and engineering: Machine learning, dynamical systems, and control*. Cambridge University Press, 2022.

[72] Y.-N. Wang *et al.*, "Focused ultrasound to displace renal calculi: threshold for tissue injury," *J. Ther. Ultrasound*, vol. 2, no. 1, p. 5, Mar. 2014, doi: 10.1186/2050-5736-2-5.

[73] T. D. Khokhlova, M. S. Canney, V. A. Khokhlova, O. A. Sapozhnikov, L. A. Crum, and M. R. Bailey, "Controlled tissue emulsification produced by high intensity focused ultrasound shock waves and millisecond boiling," *J. Acoust. Soc. Am.*, vol. 130, no. 5, pp. 3498–3510, Nov. 2011, doi: 10.1121/1.3626152.

[74] Y. Qiao, H. Yin, Z. Li, and M. Wan, "Cavitation distribution within large phantom vessel and mechanical damage formed on surrounding vessel wall," *Ultrason. Sonochem.*, vol. 20, no. 6, pp. 1376–1383, Nov. 2013, doi: 10.1016/j.ultsonch.2013.03.007.

[75] R. P. Williams, J. C. Simon, V. A. Khokhlova, O. A. Sapozhnikov, and T. D. Khokhlova, "The histotripsy spectrum: differences and similarities in techniques and instrumentation," *Int. J. Hyperthermia*, vol. 40, no. 1, p. 2233720, Dec. 2023, doi: 10.1080/02656736.2023.2233720.

[76] G. P. L. Thomas, T. D. Khokhlova, and V. A. Khokhlova, "Partial Respiratory Motion Compensation for Abdominal Extracorporeal Boiling Histotripsy Treatments With a Robotic Arm," *IEEE Trans. Ultrason. Ferroelectr. Freq. Control*, vol. 68, no. 9, pp. 2861–2870, Sep. 2021, doi: 10.1109/TUFFC.2021.3075938.

[77] Y.-N. Wang *et al.*, "Mechanical decellularization of tissue volumes using boiling histotripsy," *Phys. Med. Biol.*, vol. 63, no. 23, p. 235023, 2018.

[78] T. D. Khokhlova *et al.*, "Magnetic resonance imaging of boiling induced by high intensity focused ultrasound," *J. Acoust. Soc. Am.*, vol. 125, no. 4, pp. 2420–2431, 2009.

[79] M. Hoogenboom *et al.*, "*In vivo* MR guided boiling histotripsy in a mouse tumor model evaluated by MRI and histopathology: *In vivo* MR Guided Boiling Histotripsy," *NMR Biomed.*, vol. 29, no. 6, pp. 721–731, Jun. 2016, doi: 10.1002/nbm.3520.

[80] B. A. Rabkin, V. Zderic, and S. Vaezy, "Hyperecho in ultrasound images of HIFU therapy: Involvement of cavitation," *Ultrasound Med. Biol.*, vol. 31, no. 7, pp. 947–956, Jul. 2005, doi: 10.1016/j.ultrasmedbio.2005.03.015.

[81] M. R. Bailey *et al.*, “Use of overpressure to assess the role of bubbles in focused ultrasound lesion shape *in vitro*,” *Ultrasound Med. Biol.*, vol. 27, no. 5, pp. 695–708, May 2001, doi: 10.1016/S0301-5629(01)00342-8.

[82] A. Maxwell *et al.*, “Disintegration of tissue using high intensity focused ultrasound: Two approaches that utilize shock waves,” *Acoust. Today*, vol. 8, no. 4, pp. 24–36, 2012.

[83] T.-Y. Wang *et al.*, “Quantitative ultrasound backscatter for pulsed cavitational ultrasound therapy-histotripsy,” *IEEE Trans. Ultrason. Ferroelectr. Freq. Control*, vol. 56, no. 5, pp. 995–1005, May 2009, doi: 10.1109/TUFFC.2009.1131.

[84] T. L. Hall, J. B. Fowlkes, and C. A. Cain, “A real-time measure of cavitation induced tissue disruption by ultrasound imaging backscatter reduction,” *IEEE Trans. Ultrason. Ferroelectr. Freq. Control*, vol. 54, no. 3, pp. 569–575, Mar. 2007, doi: 10.1109/TUFFC.2007.279.

[85] T.-Y. Wang, T. L. Hall, Z. Xu, J. B. Fowlkes, and C. A. Cain, “Imaging feedback of histotripsy treatments using ultrasound shear wave elastography,” *IEEE Trans. Ultrason. Ferroelectr. Freq. Control*, vol. 59, no. 6, pp. 1167–1181, Jun. 2012, doi: 10.1109/TUFFC.2012.2307.

[86] T.-Y. Wang, T. L. Hall, Z. Xu, J. B. Fowlkes, and C. A. Cain, “Imaging feedback for histotripsy by characterizing dynamics of acoustic radiation force impulse (ARFI)-induced shear waves excited in a treated volume,” *IEEE Trans. Ultrason. Ferroelectr. Freq. Control*, vol. 61, no. 7, pp. 1137–1151, Jul. 2014, doi: 10.1109/TUFFC.2014.3013.

[87] K. B. Bader, K. J. Haworth, A. D. Maxwell, and C. K. Holland, “Post Hoc Analysis of Passive Cavitation Imaging for Classification of Histotripsy-Induced Liquefaction in Vitro,” *IEEE Trans. Med. Imaging*, vol. 37, no. 1, pp. 106–115, Jan. 2018, doi: 10.1109/TMI.2017.2735238.

[88] J. J. Macoskey, J. R. Sukovich, T. L. Hall, C. A. Cain, and Z. Xu, “Real-time acoustic-based feedback for histotripsy therapy,” *J. Acoust. Soc. Am.*, vol. 141, no. 5_Supplement, pp. 3551–3551, 2017.

[89] J. J. Macoskey *et al.*, “Bubble-Induced Color Doppler Feedback Correlates with Histotripsy-Induced Destruction of Structural Components in Liver Tissue,” *Ultrasound Med. Biol.*, vol. 44, no. 3, pp. 602–612, Mar. 2018, doi: 10.1016/j.ultrasmedbio.2017.11.012.

[90] X. Zhang *et al.*, “Real-Time Feedback of Histotripsy Thrombolysis Using Bubble-Induced Color Doppler,” *Ultrasound Med. Biol.*, vol. 41, no. 5, pp. 1386–1401, May 2015, doi: 10.1016/j.ultrasmedbio.2014.12.006.

[91] C. R. Bawiec *et al.*, “A Prototype Therapy System for Boiling Histotripsy in Abdominal Targets Based on a 256-Element Spiral Array,” *IEEE Trans. Ultrason. Ferroelectr. Freq. Control*, vol. 68, no. 5, pp. 1496–1510, May 2021, doi: 10.1109/TUFFC.2020.3036580.

[92] T. D. Khokhlova, Y. A. Haider, A. D. Maxwell, W. Kreider, M. R. Bailey, and V. A. Khokhlova, “Dependence of Boiling Histotripsy Treatment Efficiency on HIFU Frequency and Focal Pressure Levels,” *Ultrasound Med. Biol.*, vol. 43, no. 9, pp. 1975–1985, Sep. 2017, doi: 10.1016/j.ultrasmedbio.2017.04.030.

[93] P. V. Yuldashev, M. M. Karzova, W. Kreider, P. B. Rosnitskiy, O. A. Sapozhnikov, and V. A. Khokhlova, “‘HIFU beam:’ A simulator for predicting axially symmetric nonlinear acoustic fields generated by focused transducers in a layered medium,” *IEEE Trans. Ultrason. Ferroelectr. Freq. Control*, vol. 68, no. 9, pp. 2837–2852, 2021.

[94] D. H. Evans, “Doppler ultrasound: Physics, instrumentation, and clinical applications,” *No Title*, 1989, Accessed: Mar. 28, 2024. [Online]. Available: https://cir.nii.ac.jp/crid/1130000798053800064

[95] S. Bjærum, H. Torp, and K. Kristoffersen, “Clutter filter design for ultrasound color flow imaging,” *IEEE Trans. Ultrason. Ferroelectr. Freq. Control*, vol. 49, no. 2, pp. 204–216, 2002.

[96] V. Andreev, V. Dmitriev, Y. Pishchalnikov, O. Rudenko, O. Sapozhnikov, and A. Sarvazyan, “Observation of shear waves excited by focused ultrasound in a rubber-like medium,” *Acoust. Phys.*, vol. 43, pp. 123–128, Mar. 1997.

[97] Yu. A. Pishchalnikov, O. A. Sapozhnikov, and T. V. Sinilo, “Increase in the efficiency of the shear wave generation in gelatin due to the nonlinear absorption of a focused ultrasonic beam,” *Acoust. Phys.*, vol. 48, no. 2, pp. 214–219, Mar. 2002, doi: 10.1134/1.1460959.

[98] M. A. Ghanem *et al.*, “Field characterization and compensation of vibrational nonuniformity for a 256-element focused ultrasound phased array,” *IEEE Trans. Ultrason. Ferroelectr. Freq. Control*, vol. 65, no. 9, pp. 1618–1630, 2018.

[99] S. Chien, S. Usami, R. J. Dellenback, M. I. Gregersen, L. B. Nanninga, and M. M. Guest, “Blood Viscosity: Influence of Erythrocyte Aggregation,” *Science*, vol. 157, no. 3790, pp. 829–831, Aug. 1967, doi: 10.1126/science.157.3790.829.

[100] V. A. Khokhlova *et al.*, “Design of HIFU transducers to generate specific nonlinear ultrasound fields,” *Phys. Procedia*, vol. 87, pp. 132–138, 2016.

[101] G. P. L. Thomas, T. D. Khokhlova, O. A. Sapozhnikov, Y.-N. Wang, S. I. Totten, and V. A. Khokhlova, “In Vivo Aberration Correction for Transcutaneous HIFU Therapy Using a Multielement Array,” *IEEE Trans. Ultrason. Ferroelectr. Freq. Control*, vol. 69, no. 10, pp. 2955–2964, Oct. 2022, doi: 10.1109/TUFFC.2022.3200309.

[102] G. P. L. Thomas, T. D. Khokhlova, O. A. Sapozhnikov, and V. A. Khokhlova, “Enhancement of Boiling Histotripsy by Steering the Focus Axially During the Pulse Delivery,” *IEEE Trans. Ultrason. Ferroelectr. Freq. Control*, pp. 1–1, 2023, doi: 10.1109/TUFFC.2023.3286759.

[103] F. Duck, *Physical properties of tissues: a comprehensive reference book*. Academic press, 2013. Accessed: May 06, 2024. [Online]. Available: https://books.google.com/books?hl=en&lr=&id=UaXpAgAAQBAJ&oi=fnd&pg=PP1&dq=Physical+Properties+of+Tissue:+A+Comprehensive+Reference+Book&ots=I6hYZ6Gnok&sig=xMAt2wiahXnKGo45ytKw_CS1aaw

VITA

Minho Song

Minho Song received his B.S. and M.S. degrees in mechanical engineering from Yonsei University, Seoul, South Korea, in 2013 and 2015, respectively. He is currently a Ph.D. candidate in mechanical engineering at the University of Washington, Seattle, WA, USA. Before starting his Ph.D. program, he was a noise and vibration research engineer at Korea Aerospace Industries, Sacheon, South Korea from 2015 to 2019. His research interests lie in the field of biomedical acoustics including ultrasound imaging guidance for focused ultrasound therapy, cavitation monitoring, and advanced ultrasound imaging modalities.

Education

2024 Ph.D. Department of Mechanical Engineering, University of Washington, USA

2015 M.S. Department of Mechanical Engineering, Yonsei University, South Korea

2013 B.S. Department of Mechanical Engineering, Yonsei University, South Korea

Work Experience

2015 – 2019 Noise & Vibration Research Engineer, Korea Aerospace Industries, LTD

Peer-Reviewed Publications

Song, M., Thomas, G. P., Khokhlova, V. A., Sapozhnikov, O. A., Bailey, M. R., Maxwell, A. D., Yuldashev, P. V., Khokhlova, T. D. (2022). Quantitative assessment of boiling histotripsy progression based on color doppler measurements. *IEEE Transactions on Ultrasonics, Ferroelectrics, and Frequency Control*, 69(12), 3255–3269.

Ponomarchuk, E. M., Hunter, C., **Song, M.**, Khokhlova, V. A., Sapozhnikov, O. A., Yuldashev, P. V., Khokhlova, T. D. (2022). Mechanical damage thresholds for hematomas near gas-containing bodies in pulsed HIFU fields. *Physics in Medicine & Biology*, 67(21), 215007.

Ponomarchuk, E. M., Thomas, G., **Song, M.**, Krokhmal, A., Kvashennikova, A., Wang, Y.-N., Khokhlova, V. A., Khokhlova, T. D. (2024). Histology-based quantification of boiling histotripsy outcomes via ResNet-18 network: Towards mechanical dose metrics. *Ultrasonics*, 138, 107225.

Song, M., Sapozhnikov, O. A., Khokhlova, V., Khokhlova, T. D. (2024). Dynamic mode decomposition for transient cavitation bubble imaging in pulsed high-intensity focused ultrasound therapy. *IEEE Transactions on Ultrasonics, Ferroelectrics, and Frequency Control*, 71(5), 596–606.

Song, M., Sapozhnikov, O. A., Son, H., Totten, S., Wang, Y.-N., Khokhlova, T. D. (2024). Dynamic mode decomposition-based doppler monitoring for *de novo* cavitation induced by pulsed HIFU *in vivo*, *Scientific Report* (Submitted).

Song, M., Thomas, G., Khokhlova, V., Wang, Y.-N., Totten, S., Sapozhnikov, O. A., Schade, G., Khokhlova, T. D. (2024). Doppler-based assessment of boiling histotripsy-induced volumetric lesion progression *in vivo* (in preparation).

Conference Abstracts

Song, M., Thomas, G., Khokhlova, V., Sapozhnikov, O., Maxwell, A., Khokhlova, T. (2021). High pulse repetition frequency doppler ultrasound imaging method to monitor boiling histotripsy lesion formation. *20th International Symposium for Therapeutic Ultrasound* (Virtual).

Song, M., Thomas, G., Khokhlova, V., Sapozhnikov, O., Maxwell, A., Khokhlova, T. (2021). Doppler ultrasound observations and metrics of boiling histotripsy treatment progression. *181st Meeting of the Acoustical Society of America*, Seattle, WA, USA.

Song, M., Sapozhnikov, O. A., Wang, Y.-N., Hwang, J. H., Khokhlova, T. D. (2022). Passive and doppler-based assessment of cavitation activity induced by pulsed focused ultrasound. *183rd Meeting of the Acoustical Society of America*, Nashville, TN, USA.

Song, M., Thomas, G., Khokhlova, V., Wang, Y.-N., Totten, S., Sapozhnikov, O. A., Schade, G., Khokhlova, T. D. (2023). Doppler-based assessment of boiling histotripsy progression in vivo. *IEEE International Ultrasound Symposium*, Montreal, Canada.

Song, M., Sapozhnikov, O. A., Lee, G., Regnault, G., Pelivanov, I. M., Schade, G. R., Khokhlova, T. D. (2024). High intensity focused ultrasound (HIFU) based tissue elasticity mapping for planning prostate ablation. *Engineering Urology Society*, San Antonio, TX, USA

Patent Applications

T. Khokhlova, V. Khokhova, O. Sapozhnikov, and **M. Song**, "Dynamic Mode Decomposition Technique for Doppler-based Imaging of Cavitation Bubbles in Pulsed High Intensity Focused Ultrasound", (application filed)

T. Khokhlova, V. Khokhova, **M. Song**, G. Thomas, Y.-N. Wang, and R. Williams, "The use of cavitation induced by Pulsed Focused Ultrasound to alter tissue microenvironment", (record of innovation submitted)

T. Khokhlova, O. Sapozhnikov, G. Schade, and **M. Song**, "High Intensity Focused Ultrasound (HIFU) based tissue elasticity mapping for treatment planning", (record of innovation submitted)